This is to certify that the
dissertation entitled

IN SITU PROCESS MONITORING USING RAMAN SPECTROSCOPY

presented by

Javier A. Falcon

has been accepted towards fulfillment
of the requirements for the

Ph.D. degree in Chemistry and Chemical Engineering

Major Professor's Signature

3 June 2004

Date

IN SITU PROCESS MONITORING USING RAMAN SPECTROSCOPY

By

Javier A. Falcon

A DISSERTATION

Submitted to
Michigan State University
in partial fulfillment of the requirements
for the degree of

DOCTOR OF PHILOSOPHY

Department of Chemistry and
Department of Chemical Engineering & Material Science

2004

ABSTRACT

IN SITU PROCESS MONITORING USING RAMAN SPECTROSCOPY

By

Javier A. Falcon

The ability to monitor chemical processes *in situ* provides many advantages over more conventional off-line analyses. Fundamentally, *in situ* monitoring can aid in the development of more in depth process understandings and allow for greater process control. On a more practical level, *in situ* monitoring can reduce sample analysis time and allow for increased analysis automation. These advantages ultimately translate to a more robust and reproducible process. The studies presented here demonstrate the superior capability Raman spectroscopy provides for *in situ* monitoring of various processes.

Raman spectroscopy was used for *in situ* monitoring of antisolvent addition crystallization of cortisone acetate. Raman spectral features of the solvent, the antisolvent, and the solute were monitored to measure the relative concentration of the components. Different rates of antisolvent addition were monitored and the resulting solid-state form was characterized using Raman spectroscopy and differential scanning calorimetry (DSC). Raman spectroscopy was used to monitor dehydration during storage of the product crystals. This work demonstrates the advantages of using Raman spectroscopy to monitor the solution phase during crystallization and simultaneously monitoring the solid-state form.

In addition, Raman spectroscopy was used for *in situ* monitoring of anti-solvent addition crystallization of progesterone. Raman spectral features of the solute and the

anti-solvent were subjected to principal components analysis (PCA) in order to attempt to obtain information which is not readily apparent from the raw spectral data. For the system utilized, PCA was able to distinguish spectral features from the solute in solution, the solute crystals and the anti-solvent. Furthermore, PCA was capable of detecting subtle changes in the spectral data (as the addition of anti-solvent progressed) that could be used as a warning for the onset of crystallization. The current study demonstrates the advantages that can be gained by combining PCA with Raman spectroscopy for monitoring crystallizations *in situ*.

A novel dispersive Raman spectroscopic procedure for the *in situ* monitoring of fatty acid *cis* to *trans* isomerization in edible oils is also described. The rapid determination of *trans* isomer content in edible oils is of great importance in the characterization of fats and oils in the food industry. Raman spectral changes observed during the high temperature heating of oil were correlated with *cis* and *trans* isomer concentration determined by gas chromatography (GC). The short acquisition times, low laser power and ease of application of dispersive Raman spectroscopy using an NIR excitation source combined with the correlation derived from the GC data provided the capability of monitoring the isomerization *in situ*. The method developed here has potential applications for increased process control of edible oil hydrogenation, deodorization and quality control among other widely used processing steps. The *in situ* monitoring capability provided by dispersive Raman spectroscopy offers considerable advantages over the conventional off-line FT-Raman spectroscopy analysis.

ACKNOWLODGEMENTS

I would like to thank Prof. Kris A. Berglund for his guidance and support during my time at MSU. His approach to managing our research lab has given me the opportunity to grow as a scientist and as person.

I also have to thank my parents, my mom Joelle, my dad John and Kathy. You guys have believed in me and been there for me every step of the way. Thanks to the best three parents anyone could wish for.

Finally, I owe a BIG thank you (with a hug and a kiss) to Leslie. You managed to keep me sane through the tough times and helped me celebrate the good times. Thank you for everything you've done and for the sacrifices you've made for me. The best part is that hopefully now I can begin to pay you back.

TABLE OF CONTENTS

LIST OF TABLES

LIST OF FIGURES

Chapter 1

INTRODUCTION

Historically, most industrial production has involved the manufacture of the finished product, followed by laboratory testing and analysis to verify its quality, physical and chemical properties. Recently, however, there has been an increase in interest by industries and governmental regulatory agencies regarding *in situ* (on-line) process monitoring and process control methods. The Process Analytical Technologies[1] (PAT) initiative is a good example of the increased interest. PAT is a joint initiative between the pharmaceutical industry and the Food and Drug Administration (FDA) which aims to utilize emerging process engineering and manufacturing technologies to achieve high levels of quality through the use of *in situ* process monitoring and control. The main reason for the formation of initiatives such as PAT is that the adoption of these *in situ* monitoring and control methods provide companies with the opportunity to lower manufacturing cycle times, increase production efficiency and diminish end-product variability. This can in turn result in shorter time-to-market and a reduced likelihood of product failures.

Raman spectroscopy provides many advantages over other analytical techniques for monitoring processes *in situ*. This work consists of two major sections in which novel methods and applications of Raman spectroscopy are described for the *in situ* monitoring of two widely used industrial processes. The first section focuses on the *in situ* monitoring of anti-solvent addition crystallizations of active pharmaceutical ingredients (APIs) using Raman spectroscopy and principal components analysis (PCA). The second section aims at using Raman spectroscopy to monitor *in situ* the *cis-trans* isomerization

of fatty acids and the formation of oxidation products in edible oils during high temperature processing.

1-1 Theory of Raman Spectroscopy

Raman spectroscopy can be used to obtain information about electronic and vibrational transitions; this work will only deal with its use as a vibrational spectroscopy. When a molecule is irradiated by monochromatic radiation of frequency ν_o, the oscillating electric field of the light causes a short-lived distortion of the electron cloud of the bonds in the molecule. The distortion of the electron cloud induces a dipole moment oscillating with frequency ν_o, the magnitude of which is proportional to the "elasticity" of the electron cloud, i.e., the electron polarizability. The oscillating dipole gives rise to "unshifted" scattered radiation also known as Rayleigh scattering—that is scattered radiation at the same frequency as the excitation radiation.

Molecular vibrations cause the electron cloud belonging to the bonds in the molecule to expand and compress. These vibrations may change the electron cloud size and/or shape and this change translates to a change in the polarizability of the bonds involved with those clouds. The polarizability of the molecule can therefore be modulated with frequencies of vibrations ν_s. This means that some of the irradiating radiation will also be modulated during scattering, resulting in "shifted" emission lines, the Raman lines, the frequencies of which are $\nu_R = \nu_o \pm \nu_s$.

For the classic description of Raman spectroscopy discussed above[2,3], the strength of the induced dipole, μ, scales with the second-order polarizability tensor, α, and the incident electric field, E:

$$\mu = \alpha E \qquad (1\text{-}1)$$

Each of the polarizability tensor components α_{ij} depend on the normal coordinates of the molecular vibration, Q. It is possible to expand each component using a Taylor series with respect to the normal coordinates about the equilibrium position of the molecule. Ignoring terms of second or higher order in the Taylor series leaves behind an approximation that is referred to as the electrical harmonic approximation[3]

$$(\alpha_{ij})_k = (\alpha_{ij})_o + (\alpha'_{ij})_k Q_k \qquad (1\text{-}2)$$

where k identifies the k^{th} normal mode and α'_{ij} is the derivative of α_{ij} with respect to Q_k. Assuming the normal coordinates execute simple harmonic motion (mechanical harmonicity), and writing the electric field in sinusoidal form gives the induced polarization[3]

$$P = [\alpha_o + \{\alpha'_k Q_{ko} cos(\upsilon_k + \phi_k)\}] * E_o cos(\upsilon_o t) \qquad (1\text{-}3)$$

where Q_{ko} is the normal coordinate amplitude, υ_k is the frequency of the k^{th} normal mode, ϕ_k is a phase factor, υ_o is the frequency of the excitation radiation, t is time and α'_k is the derivative of the polarizability tensor. Using the trigonometric identity cos(A)*cos(B) = [cos(A+B) + cos(A-B)]/2 allows Eq. (1-3) to be expressed as[3]

$$P = \alpha_o E_o[\cos(\upsilon_o t)] + \frac{\alpha'_o E_o Q_{ko}[\cos\{(\upsilon_o - \upsilon_k)t - \phi_k\} + \cos\{(\upsilon_o + \upsilon_k)t + \phi_k\}]}{2} \qquad (1\text{-}4)$$

Eq. (1-4) provides a mathematical representation of the Rayleigh and Raman scattering process. It predicts that if light irradiates matter that is much smaller than its wavelength (in our case molecules) the incident light will be scattered at three different frequencies. The first term on the right accounts for Rayleigh scattering, which is at the same frequency as the excitation source, and has a magnitude proportional to α_o. The second

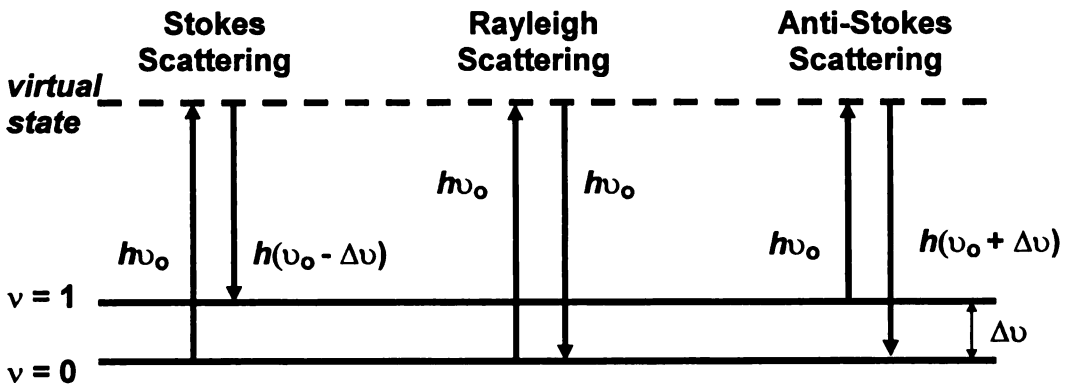

Figure 1.1. Vibration energy level diagram illustrating the energetic transitions associated with Raman spectroscopy. *h* represents Planck's constant, υ_o indicates the excitation source frequency, ν is the vibrational quantum number and $\Delta\upsilon$ is the frequency difference between the ground state and the first vibrational excited state.

and third terms account for Stoke and anti-Stokes Raman scattering respectively. Figure 1.1 shows the transitions associated with Stokes, Rayleigh and anti-Stokes scattering. Although Eq. (1-4) is incomplete (because it was derived classically), it demonstrates most of the important characteristics of Raman spectroscopy. First, polarization and scattering (Rayleigh and Raman) intensities correlate linearly with laser intensity. Second, only vibrations that change the polarizability (consequently $\alpha'_k \neq 0$) yield Raman scattering. This statement is the basis of the gross selection rule for Raman scattering. Third, Eq. (1-4) demonstrates that anti-Stokes and Stokes scattering occur at higher and lower frequencies (respectively) than the excitation frequency. Fourth, two important points that are not immediately apparent from Eq. (1-4), α'_k may vary significantly for any given molecule, this leads to wide variations in Raman scattering intensity strongly depending on the molecule being probed. And, α'_k is generally much smaller than α_o, therefore Raman scattering is much weaker than Rayleigh scattering (approximately 1,000 times weaker).

Equation (1-4) does explain the variation of Raman intensity with the fourth power of the excitation frequency for normal Raman scattering. The υ^4 factor (which can be seen in Eq. (1-5)) is derived from the classical treatment of scattering from an oscillation-induced dipole. For the same compound, the Raman spectrum will show the same frequency shift regardless of the excitation frequency, but the spectrum will be more intense as the excitation frequency is increased.

Finally, Eq. (1-4) does not explicitly incorporate one of the most important experimental parameters of Raman spectroscopy, temperature. Because Stoke and anti-Stokes Raman scattering depend on the population of the ground and the first excited

vibrational state respectively, the ratio of the scattering intensity is related to temperature by the Boltzmann distribution[2]

$$\frac{I_{R,AS}}{I_{R,S}} = \frac{(\upsilon_O + \upsilon_k)^4}{(\upsilon_O - \upsilon_k)^4} \exp\left(\frac{-h\upsilon_k}{kT}\right) \tag{1-5}$$

where $I_{R,AS}$ is anti-Stokes scattering intensity, $I_{R,S}$ is the Stokes scattering intensity, k is Boltzmann's constant, T is temperature and the other symbols have been defined above. For a given molecular vibration, the anti-Stokes scattering intensity will increase while the Stokes scattering intensity decreases. This effect becomes more pronounced as the temperature is increased. In addition, molecular vibrations with higher frequency (higher energy and lower Raman shift) will be affected more than lower frequency vibrations. This means that at a given temperature vibrations with lower Raman shifts will have a larger anti-Stokes to Stokes intensity ratio than vibrations with higher Raman shifts.

Apart from the effects of polarizability, laser wavelength, temperature conditions and other parameters discussed above on the Raman scattering intensity, it is often the case in analytical applications that the important parameter for Raman scattering intensity is the empirically determined Raman cross section, σ_j. Parameter σ_j is proportional to the probability of an incident photon being scattered as a Raman-shifted photon with a particular Raman shift[2]. Equation (1-6) relates the Raman scattering intensity (in watts) to the cross section[2], with laser intensity (I_0) in watts.

$$I_R = I_0 \, \sigma_j D dz \tag{1-6}$$

where D is the number density of scatterers (molecules per cubic centimeter) and dz is the path length of the laser in the sample and σ_j tracks with υ^4 for reasons discussed above. Equation (1-6) is now antiquated since modern Raman spectrometers almost exclusively

use photon counting detectors rather than measure watts. For this reason it is convenient to rewrite Eq. (1-6) for photon counting systems[2]

$$P_R = P_0\sigma_j'Ddz \tag{1-7}$$

P_R and P_0 now have units of photon per second and σ_j' has different frequency dependence than that of Eq. (1-6). Because of this, when P_R is measured in photons per second, the Raman intensity scales with $\upsilon_0(\upsilon_0 - \upsilon_j)^3$ rather than $(\upsilon_0 - \upsilon_j)^4$.

1-2 Background for Antisolvent Addition Crystallization Studies

Crystallization is one of the most widely used chemical engineering operations in the food, pharmaceutical and chemical industries. Of particular interest to the pharmaceutical industry is the ability to monitor and control the solid-state form that crystallizes. The solid-state form of a crystal, whether it is a polymorph, hydrate or a solvate will have significant consequences for the physical properties of the final crystal product. In order to control the physical and chemical properties of the crystal products it is necessary to monitor the crystallization process itself. Therefore, the *in situ* monitoring of crystallization is the first step to controlling the final product that crystallizes.

Historically, a variety of techniques have been used to monitor the crystallization process *in situ*. Some of these include ATR-FTIR, turbidity and nephelometry. The main disadvantage these techniques share is their inability to provide information with regard to the solid-state form crystallizing. The development of these techniques assumed that if a process involved the crystallization of one molecule, there was only one kind of solid-state form that could crystallize. The increase in polymorphs being found in

the pharmaceutical industry has created a need for an analytical technique that can simultaneously provide information about the solution and the solid state. We monitored the crystallization process *in situ* using Raman spectroscopy, and upon crystallization were immediately able to discern the solid state form that has crystallized. Furthermore, we were able to utilize Raman spectroscopy to simply and efficiently monitor the solid-state form of the product crystals during storage.

1-2.1.1 Crystallization

Crystallization begins with the generation of supersaturation. Once enough supersaturation is generated the solute molecules aggregate for form nuclei, this process is referred to as nucleation. Further integration of molecules to the nuclei is defined as crystal growth. Crystallization is a process governed by both the thermodynamics and the kinetics of the interface between the crystalline phase and the solution phase. The driving force behind the onset of crystallization is the disturbance of the thermodynamic equilibrium between a supersaturated and a saturated solution. Nucleation and crystal growth are governed more by the kinetics of mass transfer from the bulk solution phase to the solid phase.

1-2.1.1 Supersaturation

Supersaturation is a thermodynamically metastable state in which nucleation and crystal growth occur. Under supersaturated conditions, the chemical potential difference provides the driving force for the phase transition from solution to solid crystals.

Supersaturation, S, is defined as $S = a/a^*$, where a is the activity of the supersaturated solution and a^* is the activity of the saturated solution. Typically the ratio of activity coefficients is assumed to be unity; therefore, we can replace activity with concentration.

Under this assumption, supersaturation can be approximated as the ratio of the concentration of the supersaturated solution to the concentration of the saturated solution at a given temperature. While recent studies[4] have shown that this assumption is questionable, it is often used as a practical necessity.

1-2.1.2 Nucleation

Supersaturation alone is not enough cause for a system to begin to crystallize. Before crystals can develop, tiny crystallites of the smallest size capable of independent existence (termed nuclei) are formed in the supersaturated phase. This occurs when a specific supersaturation, known as the metastable supersaturation (Δc_{met}) is obtained in the system. This metastable region comes about because crystallizations don't always begin when the solubility limit is exceeded. Therefore, at every temperature there is a lower limit to supersaturation (the solubility limit) and an upper bound (the supersaturation limit). Between these boundaries nucleation is possible but not a certainty.

As shown in Figure 1.2, nucleation may be primary (which does not require preexisting crystals of the substance that crystallizes) or secondary (in which nucleation is induced by preexisting crystals of the substance). Primary nucleation may be homogeneous, whereby the nuclei of the crystallizing substance arise spontaneously in the medium in which crystallization occurs, or heterogeneous, whereby the nuclei incorporate foreign solid matter such as dust particles or the walls of the container. It is widely accepted that true homogeneous nucleation is not a common event.

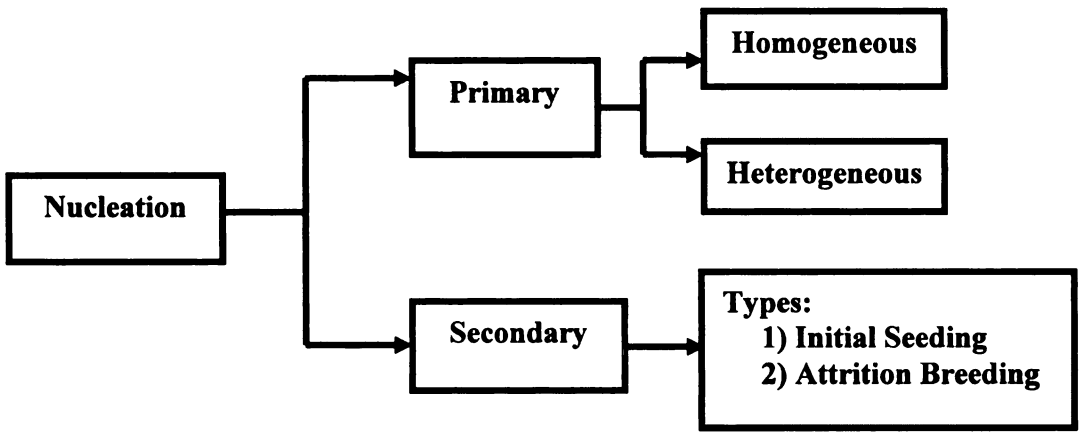

Figure 1.2. Mechanisms of nucleation[4].

There is no single nucleation theory that is accepted for predicting nucleation rate, but several correlations based on the power law model have satisfactorily explained the experimental data[4].

$$B = k_N \Delta C_{met}^n \tag{1-8}$$

Where B is the nucleation rate, k_N is the nucleation rate constant and ΔC_{met} is the metastable zone width. The exponent n is the apparent order of nucleation. The nucleation process eventually reaches equilibrium between the growth of nuclei and the dissolution of nuclei. Some of the nuclei reach a critical size (r*), which is dependent on the change of the free energy of the particle. Nuclei that are smaller than r* tend to dissolve, whereas those larger than r* are true nuclei and tend to grow to form macroscopic crystals[5,6].

1-2.1.3 Crystal Growth

The final stage of the crystallization process is crystal growth. This stage is the time when nuclei grow into macroscopic crystals. Crystal growth can be thought of as a succession of events (Figure 1.3): a) transport of species from the bulk solution to a site at the crystal surface (with initial solvent loss), b) adsorption of the growth unit to a site at the crystal surface, c) surface diffusion from the impingement site to a growth site d) incorporation into the crystal lattice[7] (with final solvent loss). The rate-limiting step may be any of the above depending on the growth conditions such as supersaturation, temperature, additives or solvent, and the hydrodynamics of the system.

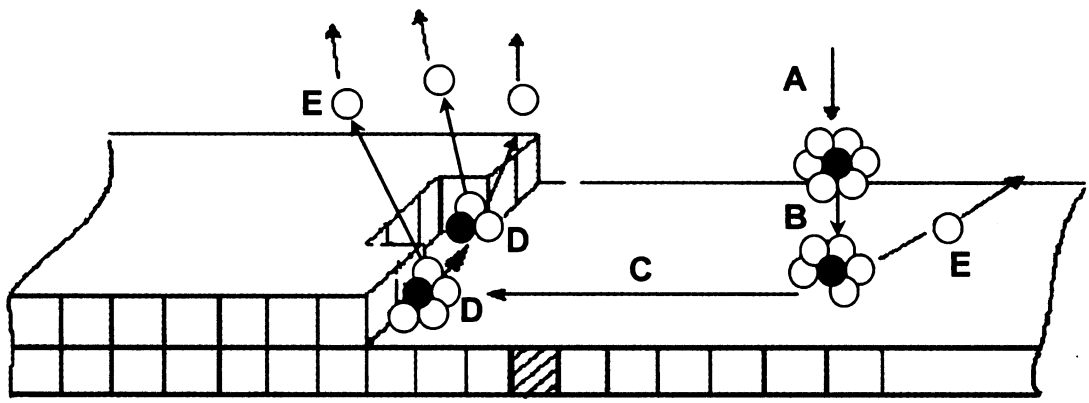

Figure 1.3. Crystal growth model[4]. Black (middle sphere) represents molecule of interest. White (surrounding spheres) represent solvent molecules. A) transport of species from the bulk solution to a site at the crystal surface, B) adsorption of the growth unit to a site at the crystal surface, C) surface diffusion from the impingement site to a growth site D) incorporation into the crystal lattice, E) initial and final solvent loss.

The basic expression used to relate crystal growth to supersaturation is[4]

$$G = k_g S^g \tag{1-9}$$

this equation uses a linear crystal growth velocity, correlating the growth rate (G) with the supersaturation (S). k_g is defined as the growth rate constant and the exponent g is the order of crystal growth.

A number of models have been proposed to represent crystal growth. Many of these models are mathematically complex, and only provide a tentative basis for the correlation of experimental data[4, 8].

1-2.2 Tailor-Made Additives

There is an enormous amount of literature[9,10] demonstrating the design principles for tailor-made additives to control and inhibit the growth of molecular crystals.

The basic idea behind tailor-made impurities is best appreciated by realizing that a crystal surface is a termination of the bulk crystal structure and that the different surfaces of a crystal will expose different parts of the crystallizing molecule to the external environment. This means that the stereochemistry and functionality of each surface will be different.

To design additive molecules that capitalize on this feature of crystals, two rules must be satisfied[9,10,11]. First, the additive must be able to enter the surface lattice site. To do this, part of the additive molecule must resemble the crystallizing host. Second, once in the crystal surface, the additive molecule must be capable of preventing crystallization by discouraging other host molecules from joining the crystal. To fulfill this role, part of the additive molecule must differ from the host either in its functionality or its

stereochemistry so that either electrostatic or steric effects can be used to prevent crystallization.

It has long been recognized that the presence of impurities substantially affects the kinetics of crystal nucleation, growth and dissolution[9]. It is possible that by affecting these processes, the impurity will promote the crystallization of a metastable solid-state form.

1-2.3 Principal Components Analysis

Mathematically, PCA is based on an eigenvector decomposition of the covariance or correlation matrix of the process variables. For a given data matrix X with *m* rows and *n* columns, with each variable being a column and each sample a row, the covariance matrix of X is defined as

$$\mathrm{cov}(X) = X^T X / m\text{-}1 \qquad (1\text{-}10)$$

with the condition that the columns of X have been "mean centered" (by subtracting off the original mean of each column to create columns that have a mean of zero). If the columns of X have been "autoscaled" (by dividing each column by its standard deviation to ensure columns with zero mean and unit variance), Eq. (1-10) gives the correlation matrix of X. The data presented in this work was only mean centered. PCA decomposes the data matrix X into a sum of the outer products of vectors t_i and p_i plus a residual matrix E:

$$X = t_1 p^T_1 + t_2 p^T_2 + \ldots + t_k p^T_k + E \qquad (1\text{-}11)$$

Here *k* must be less than or equal to the smaller dimension of X. The t_i vectors are known as scores and contain information on how the samples relate to each other. Score plots feature the scores of one principal component plotted versus the scores of another

principal component. These plots allow investigators to view the relevant variation of the data set in a smaller number of dimensions. Samples that are close to each other on a given score plot are similar with respect to the original measurements. This mathematical proximity translates to chemical similarity if meaningful measurements have been made[12].

The p_i vectors are known as loadings and contain information on how the variables relate to each other. Principal component loadings are used to determine which variables (Raman shift for Raman spectroscopy) influence a particular principal component. In addition, principal component loading plots aid in the visualization of principal components[12,13].

In the PCA decomposition, the p_i vectors are eigenvectors of the covariance matrix, therefore for each p_i

$$\text{cov}(X)\, p_i = \lambda_i\, p_i \tag{1-12}$$

where λ_i is the eigenvalue associated with the eigenvector p_i. The t_i form an orthogonal set ($t_i\, t^T_j = 0$ for $i \neq j$), while the p_i are orthonormal ($p^T_i\, p_j = 0$ for $i \neq j$, $p^T_i\, p_j = 1$ for $i = j$). It should be noted that for X and any t_i, p_i pair

$$X\, p_i = t_i \tag{1-13}$$

This is due to the fact that the score vector t_i is the linear combination of the original X data defined by p_i. The t_i, p_i pairs are arranged in descending order according to the associated λ_i. The λ_i are a measure of the amount of variance described by the t_i, p_i pair. It is possible then to think of variance as information. Because the t_i, p_i pairs are in descending order of λ_i, the first pair captures the largest amount of information of any pair in the decomposition. In fact, it can be shown that the t_1, p_1 pair captures the greatest

amount of variation in the data that is possible to capture with a linear factor. And, each subsequent pair captures the greatest possible amount of variance remaining after subtracting $t_i p^T_i$ from X.

It is generally found that using PCA allows the data to be adequately described using far fewer factors than original variables. Therefore, confusion created by data overload can be solved by observing the data using fewer scores than original variables. It should be also mentioned that many times PCA aids in finding combinations of variables that are useful in describing certain phenomena. The combinations of variables are often more reliable indicators of sample conditions than single variables because of the signal averaging aspects of PCA.

There are a number of algorithms (the power method[14], the Jacobi method[14], singular value decomposition [SVD][14], and NIPALS[15]) used to calculate the loadings and scores for PCA. SVD is the preferred algorithm because it is most stable under the widest range of applications, and it is the algorithm used in our report. A more in depth discussion of the algorithms used for PCA is outside the scope of this work. For detailed discussions of the individual algorithms and of PCA in general the reader is directed to the references provided[12,16,17,18,19].

1-3 Background for Edible Oil Studies

trans Fatty acids are present in a variety of food products; some are derived from natural sources, but most come from products that contain commercially hydrogenated fats. The nutritional properties of trans fatty acids have been debated for many years, particularly with respect to the amounts of low density and high density lipoprotein (LDL, HDL) contained in serum. Some studies have shown that *trans* fatty acids elevate

levels of serum LDL ("bad") cholesterol and lower HDL ("good") cholesterol[20,21,22]. Results like these have prompted the Food and Drug Administration (FDA) to implement new regulations[23] which make labeling of *trans* fatty acids mandatory on food products.

Current standard methods for determining the *cis* and *trans* content of fats and oils include gas chromatography and Fourier Transform infrared spectroscopy (FT-IR) for samples captured off-line. In the past, Raman spectroscopy has also been used for this purpose[24,25,26,27,28,29], although its use has been almost exclusively limited to Fourier Transform (FT) Raman spectroscopy (because of fluorescence from the oil samples). The major drawback to using FT-Raman spectroscopy is that current technology only allows for off-line analysis of samples.

Within the past few years there have been technological advances that allow dispersive Raman spectrometers to use near infrared (NIR) lasers as excitation sources. The use of an NIR laser for excitation eliminates the interfering fluorescence from oil and fat samples. The present work takes advantage of the flexibility and the *in situ* analysis capability offered by dispersive Raman spectrometers and combines it with an NIR laser excitation source. This powerful combination allowed us to use dispersive Raman spectroscopy to qualitatively and quantitatively monitor changes (*in situ*) of the fatty acid composition of sunflower oil during high temperature processing.

1-4 References

1. Food and Drug Administration (FDA), FDA Process Analytical Technologies (PAT) page. URL http://www.fda.gov/cder/OPS/PAT.htm

2. McCreery, R. L.; *Raman Spectroscopy for Chemical Analysis*. Wiley-Interscience: New York, 2000.

3. Long, D. A.; *Raman Spectroscopy*, McGraw-Hill: New York, 1977.

4. Myerson, A. S., *Handbook of Industrial Crystallization*, Butterworth-Heinemann Ltd.: Oxford, 1993.

5. *Polymorphism in Pharmaceutical Solids*. Ed. Brittain, H.G., Marcel Dekker: New York, 1999.

6. Boistelle, R., *Advances in Nephrology*, **1986**, 15, 173.

7. Bennema, P., *J. Crystal Growth*, **1967**, 1, 128.

8. Mullin, J. W., *Crystallization*, 3rd Edition, Butterworth-Heinemann Ltd.: Oxford, 1993.

9. Mersmann, S. *Crystallization Technology Handbook*. Marcel Dekker: New York, 1995.

10. Weissbuch, I. et al, in The Lock and Key Principle, J. P. Behr (ed), Chap. 6. Chichester: Wiley, 1994.

11. Blagden, N.; Davey, R.; *Chemistry in Britain*. **1999**, 44.

12. Beebe, K. R.; Pell, R. J.; Seasholtz, M. B. *Chemometrics: A Practical Guide*; John Wiley & Sons: New York, 1998.

13. ThermoGalactic website. URL http://www.galactic.com/algorithms/pca.htm

14. *HoloReact Software Operations Manual*. Kaiser Optical Systems, Inc.

15. Press, W. H.; Flanner, B. P.; Teukoslky, S.; Vetterling, W. T. *Numerical Recipes: The Art of Scientific Computing*, Cambridge University Press: Cambridge, 1986.

16. Malinowski, E. R. *Factor Analysis in Chemistry*, 2nd Ed.; John Wiley & Sons: New York 1991.

17. Beebe, K. R. Kowalski, B. R. *Analytical Chemistry*, **1987**, 59, 1007A-1017A.

18. Jackson, B. B. *Multivariate Data Analysis: An Introduction*, Richard D. Irwin, Inc.: Homewood, Illinois 1983.

19. Jackson, J.E. A User's Guide to Principal Components; John Wiley & Sons: New York 1991.

20. Mensink, R.P.; Katan, M.B. *N. Engl. J. Med.*, **1990**, 323,439.

21. Judd, J.T.; Clevidence, B.A.; Muesing, R.A.; Wittes, J.; Sunkin, M.E.; Podczasy, J.J. *Am. J. Clin. Nutr.*, **1994**, 59, 861.

22. Almendingen, K.; Jordal, O.; Kierulf, P.; Sandstad, B.; Pedersen, J.I. *J. Lipid Res.*, **1995**, 36, 1370.

23. FDA/DHHS, 68 Federal Register, 41,434 (July 11, 2003). *Food Labeling: Trans Fatty Acids in Nutrition Labeling, Nutrient Content Claims, and Health Claims* (Final Ruling). URL http:// www.cfsan.fda.gov/~lrd/fr03711a.html

24. Bailey, G.F; Horvat, R.J. *J. Am. Oil Chem. Soc.* **1972**, 49 (8), 494-498.

25. Sadeghi-Jorabchi, H.; Hendra, P.J.; Wilson, R.H.; Belton, P.S. *J. Am. Oil Chem. Soc.* **1990**, 67 (8), 483-486.

26. Sadeghi-Jorabchi, H.; Wilson, R.H.; Belton, P.S.; Edwards-Webb, J.D.; Coxon, D.T. *Spectrochimica Acta.* **1991**, 47A (9/10), 1449-1458.

27. Baeten, V.; Hourant, P.; Morales, M.T.; Aparacio, R. *J. Agric. Food Chem.* **1998**, 46, 2638-2646.

28. Johnson, G.L.; Machado, R.M.; Freidl, K.G.; Achenbach, M.L.; Clark, P.J.; Reidy, S.K. *Organic Process Research & Development.* **2002**, 6 (5), 637-644.

29. Weng, Y.M.; Weng, R.H.; Tzeng, C.Y.; Chen, W. *Applied Spectroscopy.* **2003**, 57 (4), 413-418.

Chapter 2

MONITORING OF ANTI-SOLVENT ADDITION CRYSTALLIZATIONS WITH RAMAN SPECTROSCOPY *

*_Crystal Growth and Design_, **2003**, 3(6), 947-952.

2-1 Abstract

Fiber optic Raman spectroscopy was used for in situ monitoring of antisolvent addition crystallization of cortisone acetate. Raman spectral features of the solvent, the antisolvent, and the solute were monitored to measure the relative concentration of the components. Different rates of antisolvent addition were monitored and the resulting solid-state form was characterized using Raman spectroscopy and differential scanning calorimetry (DSC). Raman spectroscopy was used to monitor dehydration during storage of the product crystals. The current study demonstrates the advantages of using Raman spectroscopy to monitor the solution phase during crystallization and simultaneously monitoring the solid-state form.

2-2 Introduction

The solid-state form of a compound (polymorphs, hydrates, or solvates) must be controlled to satisfy regulatory authorities as to the bioavailability of formulations of new chemical entities[1]. One of the major contributory factors to bioavailability is the solubility of a compound. Solubility can be largely dependent on the solid-state form, as different solid-state forms have different energies and therefore different solubilities.[2,3] To control the solid-state form that will crystallize, it is necessary to be able to monitor the solid-state form in situ during crystallization, and to be able to monitor the different stages of the crystallization process itself. In the present work, Raman spectroscopy is

used to monitor the crystallization process in situ. In addition, in situ analysis of the spectra obtained during the crystallization gives insight into the solid-state form that crystallizes as it crystallizes. Finally, we present the use of Raman spectroscopy to monitor the dehydration of crystal hydrates over time.

2-3 Experimental Section

2-3.1 Materials and Instrumentation

Solutions used in the crystallization experiments were prepared with deionized water and analytical grade acetone (J. T. Baker). Cortisone acetate (CA) and bisnoraldehyde (BA) were provided by Pharmacia Corporation (Kalamazoo, MI) and were used without further purification. Recrystallizations were conducted in a 60-mL glass water-jacketed reactor. The temperature of the water jacket was maintained at 22.4 ± 0.6 °C using a Brinkmann water circulator. Water addition rates and total water added volumes were controlled with a 665 Dosimat (Metrohm Ltd.) water pump. A schematic diagram of the experimental setup is shown in Figure 2.1. All crystallizations were performed using the same size stir bar with the same stir rate. Raman spectra were collected using a HoloLab Series 5000 Kaiser Optical Systems instrument. Details of the HoloLab 5000 have been described previously.[4,5] Briefly, a 100 mW external cavity stabilized diode laser at 785 nm is used for sample illumination. A CCD camera, a spectrograph, and a fiber optic probe comprise the rest of the HoloLab 5000 system. Remote sampling was accomplished by employing a fiber optic probe attached to an immersion optic to focus the incident beam into the solutions. The positioning of the immersion optic within the crystallizer was maintained as constant as possible through out all the experiments. This

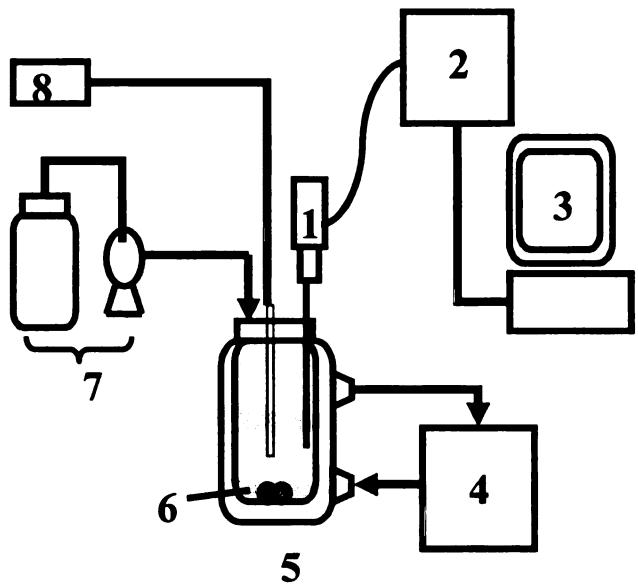

2.1. Schematic of the experimental setup. (1) Raman probe, (2) HoloLab 5000, (3) PC, (4) water circulator, (5) jacketed reactor, (6) magnetic stir bar, (7) water reservoir and pump, (8) digital thermometer.

ensured that any effects the immersion optic may have had on the crystallization process impacted all the experiments in the same way. All spectra were a sum of five accumulations collected over 5 seconds each, for a total spectra acquisition time of 25 seconds.

2-3.2 Calibration of Raman Spectra

The Raman spectra of standards were used to construct a partial least-squares (PLS) regression model using QuantIR, a PLS regression analysis software package by ASI-Mettler Toledo. The model consists of 30 standard solutions ranging in concentration from 0.04 to 2.56 wt % of CA, from 40.00 to 99.00 wt % acetone and from 60.00 to 0.00 wt % water.

2-3.3 Anti-Solvent Addition Crystallizations

Binary solutions of acetone and CA were prepared (1 wt % CA in acetone) for the starting point of the first set of crystallizations. For the starting point for the second set of crystallizations, ternary solutions of acetone, water, and CA were prepared (87.00, 10.50, and 2.50 wt %, respectively). The solutions were stirred in the glass-jacketed reactor for 2 hours to ensure dissolution of CA. Once this was achieved, water was added continuously to the solutions. For both sets of crystallization experiments, three different water addition rates were used, 0.25, 0.50, and 1.00 mL/min. During the continuous addition of water, the crystallization was monitored by acquiring Raman spectra of the solution in 1-min intervals.

2-3.4 Solid-State Analysis of Crystals

The resulting crystals were stored in scintillation vials in a dark cabinet at room temperature (23 °C) and humidity. Solid-state Raman spectra were recorded in the

scintillation vials immediately after crystallization and each day thereafter. Images of the crystals were obtained using an Olympus IMT-2 light microscope equipped with a 40X magnification objective. The thermal properties of the different solid-state forms were characterized with a differential scanning calorimeter, TA instrument DSC Q 100. The temperature program used was heating at 10 °C/min to 180 C, heating from 180 to 230 °C at 5 °C/min, and heating from 230 to 250 °C at 2.5 °C/min.

2-3.5 Effect of Impurities

Another set of three crystallizations was performed. These crystallizations were all conducted using a 0.50 mL/min water addition rate. BA was chosen as the impurity for study due to its structural similarity to CA. BA was added during the solution preparation step, prior to the beginning of the crystallization experiment. These solutions were initially prepared with the same concentrations of acetone, CA, and water as the second set of crystallizations. The amounts of BA added to each crystallization were as follows: 0.04, 0.15, 0.22 wt %.

2-3.6 Principal Components Analysis (PCA)

The Raman spectra obtained during the second set of crystallizations were subjected to PCA using Matlab based HoloReact software provided by Kaiser Optical Systems. In HoloReact, the PCA mode uses singular value decomposition (SVD) for the calculations. The regions selected for analysis were 750-850 and 1600-1630 cm^{-1}, and PCA was applied to both regions simultaneously. Examination of the third factor obtained from PCA was used to monitor the saturation point of the solutions.

2-4 Results and Discussion

2-4.1 Calibration of Raman Spectra

Raman spectra of standard solutions were collected and subjected to a partial least squares (PLS) calibration analysis. The peak region selected to correlate spectra and solution concentrations was 1610-1680 cm^{-1}. This is the only region in the spectra of the CA, acetone, water solution that contains accessible CA vibrational bands. The standard error determined by a leave-one-out cross validation was 0.04 CA weight percent. The two vibrational bands found in the 1610-1680 cm^{-1} region are explained by conjugation theory.[6] Figure 2.2 shows the molecular structure of CA. The conjugation between the C=O at position 3 and the C=C at position 4 results in the delocalization of the π electrons and reduces the double-bond character of both sets of double bonds. This causes the Raman scattering to occur at lower wavenumbers than those of unconjugated systems. Using this interpretation, the peak found between 1600 and 1625 cm^{-1} in the spectra is assigned to C=C vibrations. The peak found between 1660 and 1680 cm-1 in the spectra is assigned to C=O vibrations.

2-4.2 Solubility Curve

CA solubility in acetone/water solutions of varying compositions at 22.4 ± 0.6 °C was determined using the PLS model described above. Figure 2.3 shows the solubility curve of CA determined via this procedure. Each point on the curve is the average of at least three measurements. The error bars represent the standard deviation of three measurements. Solid CA in excess of solubility was added to solutions initially containing 40/60, 50/50, 60/40, 70/30, 80/20, 90/ 10 wt % acetone/water. Each solution

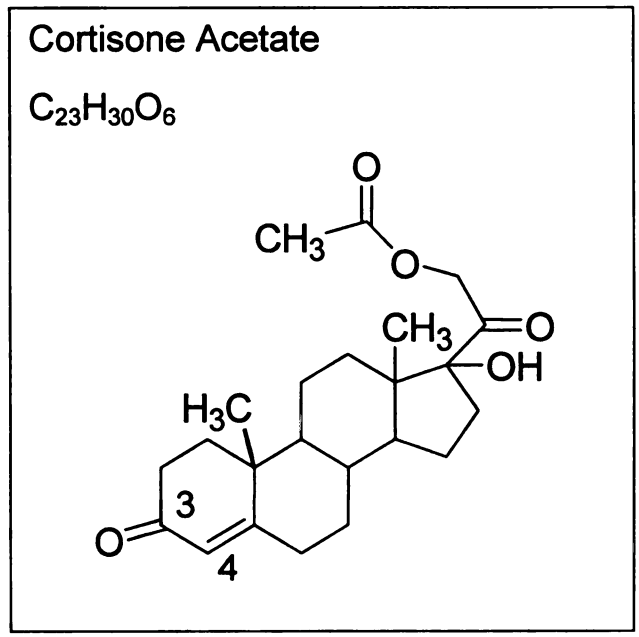

Figure 2.2. Molecular structure of cortisone acetate (CA).

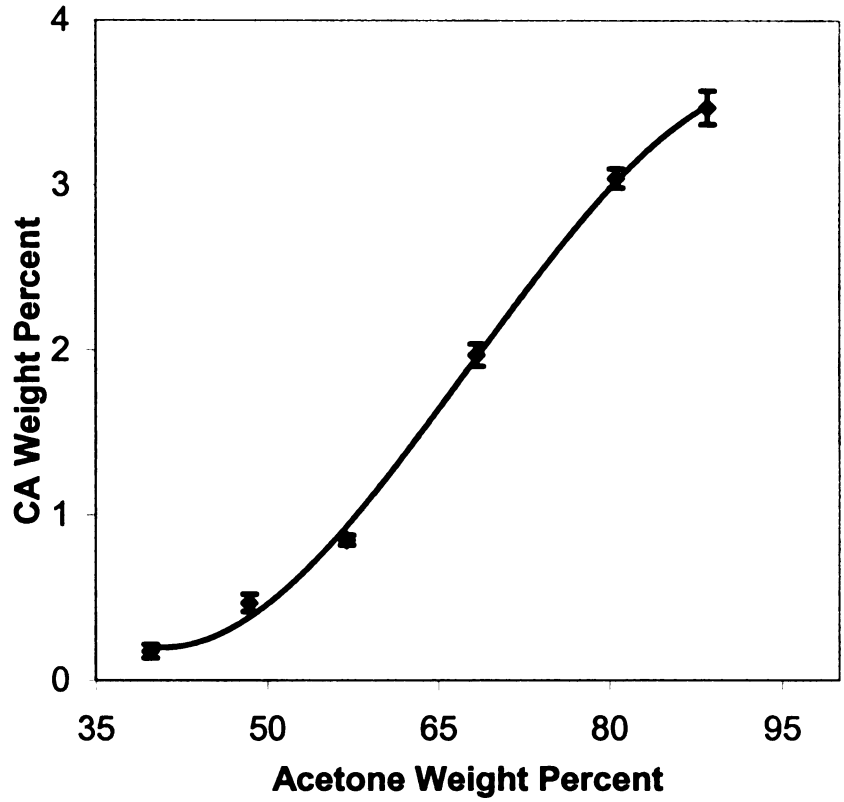

Figure 2.3. Solubility of cortisone acetate in binary mixtures of acetone/water at 22.4 °C.

was stirred for 24 h to ensure equilibrium was achieved. Raman spectra from the liquid phase were collected, and the CA concentration was determined using the calibration. The solubility of CA was found to be higher (2-3 times higher) in acetone/water solutions of composition from 90/10 to 60/40 acetone/water compared to the solubility of CA in acetone. The increase in solubility was an unexpected result since the literature value reported for the solubility of CA in water is 2.20 x 10^{-3} wt %[7] The reported solubility of CA in acetone is 1.71 wt %;[7] therefore, the expectation was that the addition of water to acetone would decrease the solubility of CA. Although unexpected, an enhanced solubility or maximum solubility effect[8] has been observed for a variety of solid systems dissolved in a binary mixed solvent.

2-4.3 Crystallizations

The CA and acetone concentrations decrease as water is added into the solution. As more water is added into the solution, the solubility of CA is also decreased. Eventually, the decrease in solubility due to water addition drives the CA concentration beyond solubility. At this point, the solution can no longer sustain the level of supersaturation and CA nucleates, resulting in a rapid decrease of CA concentration in solution. The last period reflects the final slow growth of the crystals in a solution with a near-depleted supersaturation. Figure 2.4 shows the solution phase peak area plotted versus time for the first set of crystallizations, which depicts the decrease in concentration and the crystallization events described. The low concentration of CA precluded the use of the peak area of the solute to monitor the crystallization. It was necessary to use a solvent band to follow the crystallization. The 787 cm^{-1} acetone band assigned to the C-C(=O)-C

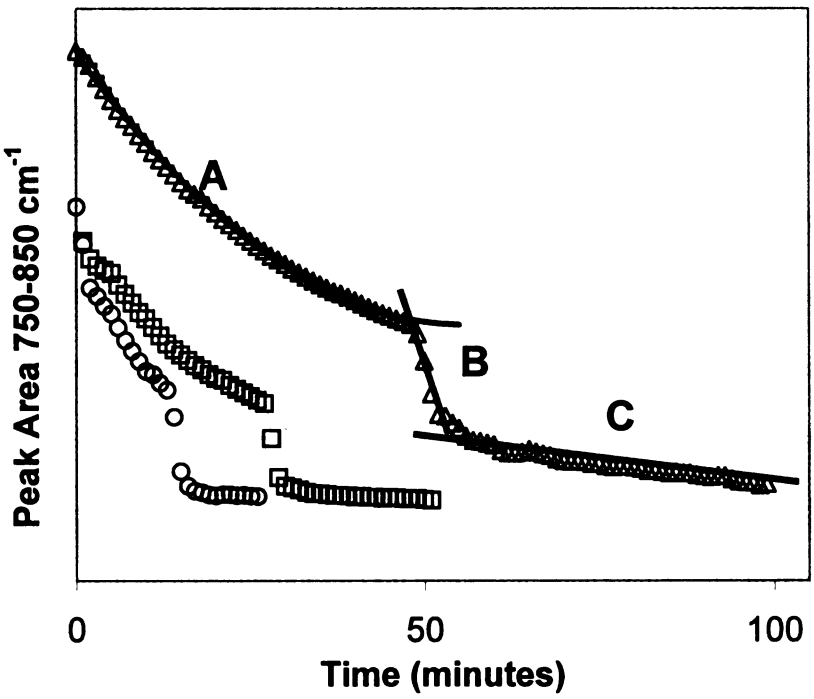

Figure 2.4. Real time change in the baseline peak area of the Raman spectrum between 750-850 cm^{-1} for the first set of crystallizations as described in the text. The symbols represent different water addition rates: (Δ) 0.25, (□) 0.50, (O) 1.0 mL/min. Line A shows the change in concentration as water is added to the solution, line B follows the sharp decrease in peak area caused by turbidity in the solution which is caused by nucleation. Line C follows the solution after the nucleation event.

symmetric stretch[9] was used to monitor the crystallization event. It is important to note that the rapid decrease in signal intensity (evident in Figure 2.4) that occurs immediately after crystallization begins is not solely due to a decrease in concentration of the species being monitored. The growing crystals will reflect and refract the excitation and Raman scatter; this consequently decreases the amount of Raman scatter that reaches the collection optics and therefore the detector. In effect, the Raman spectrometer is acting as a turbidity meter. This is particularly useful when (as above) monitoring the crystallization of a compound present at low concentrations. It is possible to monitor a solvent band with the knowledge that the crystal growth will be evident even though the compound being crystallized is not being directly monitored. As expected, the slope of the line marked A (when normalized to 1) in Figure 4 matches the slope of the line of the calculated concentration change for acetone for all three curves. To monitor the peak intensity of CA accurately, a second set of crystallizations was performed at a higher starting CA concentration. This second set of experiments was made possible because of the a priori knowledge from the solubility curve that CA displays increased solubility in a range of binary mixtures of acetone/water.

Figure 2.5 shows the peak area of the 787 cm^{-1} acetone band plotted versus time for the second set of crystallization experiments. Again as expected, the slope of the line marked A (when normalized to 1) in Figure 2.5 matches the slope of the line of the calculated concentration change for acetone for all three curves.

Due to the increased concentration of CA in the second set of experiments, it was possible to use a solute band to monitor the crystallization event. The CA 1600-1625 cm^{-1} band assigned to C=C vibrations was used. Figure 2.6 shows the peak area of the band

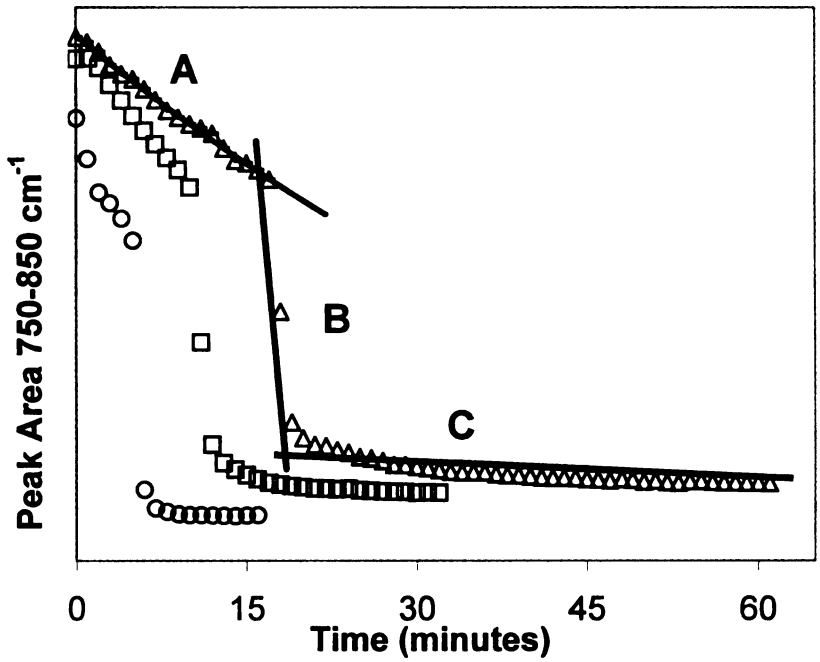

Figure 2.5. Real time change in the baseline peak area of the Raman spectrum of cortisone acetate between 750-850 cm^{-1} for the second set of crystallization experiments as described in the text. The symbols represent different water addition rates: (Δ) 0.25, (□) 0.50, (O) 1.0 mL/min. Line A shows the change in concentration as water is added to the solution, line B follows the sharp decrease in peak area caused by turbidity in the solution which is caused by nucleation. Line C follows the solution after the nucleation event.

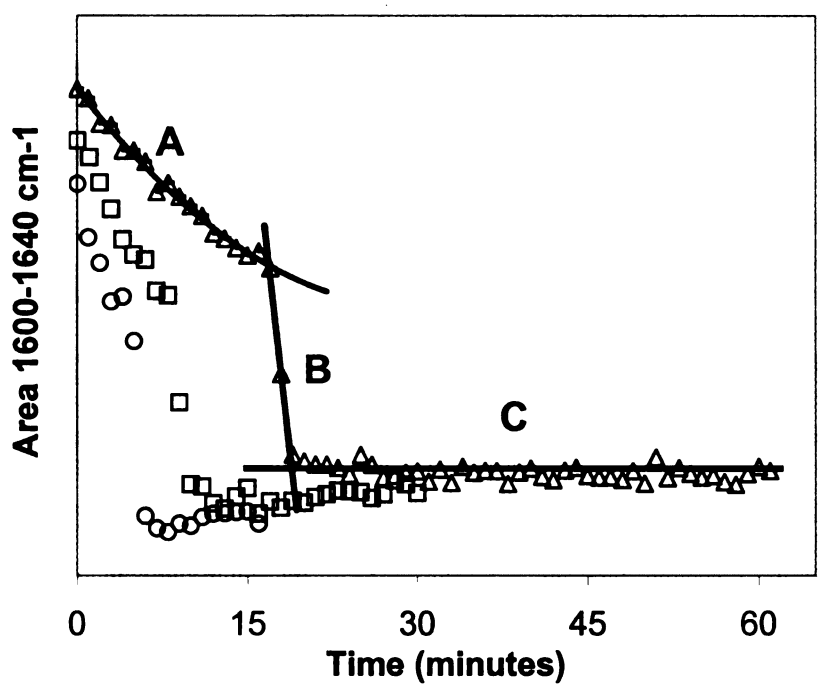

Figure 2.6. Real time change in the baseline peak area for the Raman spectrum of cortisone acetate between 1600-1640 cm^{-1} for the second set of crystallization experiments. The different symbols represent different water addition rates: (Δ) 0.25, (□) 0.50, (O) 1.0 mL/min. Line A shows the change in concentration as water is added to the solution, line B follows the sharp decrease in peak area caused by turbidity in the solution which is caused by nucleation. Line C follows the solution after the nucleation event.

versus time for the second set of experiments. The data for the CA concentration are in qualitative agreement with those obtained for acetone.

It is important to note that no calibration model has been applied to the data presented in Figures 2.4-2.6. The peak area profiles come directly from the raw data. With a reliable instrument that exhibits negligible signal drift from day to day (or more likely by avoiding signal drift through peak area ratio methods or daily calibrations), the idea of using the raw peak area data vastly simplifies the process of monitoring the concentration changes in situ. The simplification comes from the fact that it is possible to monitor the relative concentrations of components during the crystallization without having to perform the crystallization and then subsequently subject the data to the calibration model. Certain methods[10] have claimed to monitor crystallizations in situ, even though the data must first be collected and then run through a calibration model. In that scenario, there is no possibility for changing experimental conditions in response to a perturbation to the crystallization.

Monitoring the crystallization process has been previously demonstrated using ATR-FTIR[11] and dynamic light scattering[12] among other techniques. The drawback to these techniques is that it is not possible to obtain information regarding the structure of the crystals during the crystallization. With Raman spectroscopy, the spectra of the solution and then of the slurry can be monitored for changes in the solid-state form that crystallizes.

Figure 2.7, trace 1, shows the Raman spectrum of the as received CA crystals used to prepare the solutions. Trace 2 shows the spectrum of CA in solution, trace 3 shows the

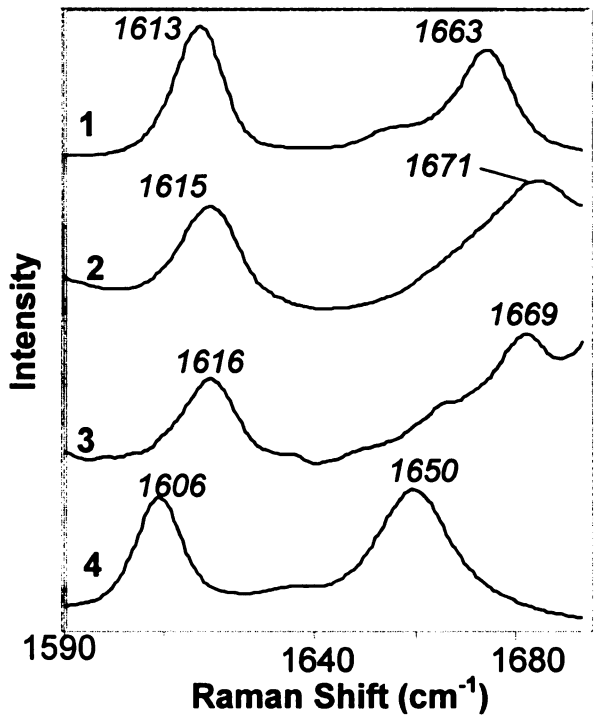

Figure 2.7. Comparison of cortisone acetate Raman spectra for different environments in the region between 1600-1680 cm^{-1}. Spectrum (1): as received crystals. Spectrum (2): solution of CA, acetone and water. Spectrum (3): CA crystals in slurry. Spectrum (4): crystals after drying.

spectrum of the CA in slurry after crystallization, and trace 4 shows the dried product crystals after crystallization. The 1600-1680 cm^{-1} region is useful to track the changes the crystals underwent from the solution state through to the product crystals. From Figure 2.7, it can be seen that the original crystals are not the same as the product crystals. Perhaps more importantly, the spectrum of the crystals in the slurry shows that the solid-state form that has crystallized is not the same as the original crystals. Even before the crystals are vacuum filtered and dried, it is possible to know which solid-state form has crystallized. The product crystals turn are a hydrate of CA (see solid state analysis below for explanation). Both sets of crystallizations, with different concentrations of CA, yielded the same CA hydrate crystals.

2-4.4 Solid-State Analysis

Generally, as the rate of supersaturation increases (increasing rate of water addition), the induction time decreases. Accordingly, higher rates of supersaturation exhibit larger numbers of small crystals or the formation of precipitate. Figure 2.8 shows photomicrographs of the product crystals resulting from the three different water addition rates of the second set of crystallizations (the results were the same for the first set). It is evident from the different sizes of the crystals that, as expected, the highest rate of water addition yielded the smallest crystals. The Raman spectra change with the passage of time indicating a transformation occurs. Again, the region of focus is between 1600 and 1680 cm^{-1}. Immediately after crystallization and for some time after, there are two large peaks that appear at 1606 and 1650 cm^{-1} in the spectrum of the product crystals. As time passes, the 1606 peak develops a shoulder. The peak at 1606 cm^{-1} then becomes a doublet at 1605 and 1613 cm^{-1}. The 1650 cm^{-1} peak also develops a shoulder and in

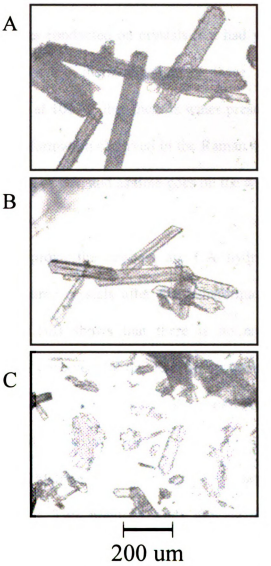

Figure 2.8. Cortisone acetate crystals resulting from the three different rates of water addition used. These photographs are at the same magnification and encompass identical viewing areas. The pictures represent the different water addition rates. (A) 0.25, (B) 0.50, (C) 1.00 mL/min.

addition shifts toward higher wavenumbers. The 1650 cm^{-1} peak then becomes a peak at 1651 cm^{-1} with a small shoulder at 1669 cm^{-1}. Figure 2.9 shows the Raman spectra that illustrate the transformation described above. To further investigate this phenomenon, a DSC experiment was conducted on crystals that had yet to undergo the transformation. Figure 2.10A shows the thermodiagram of these crystals. It is evident from the endotherm centered at 100 °C that there is water present in the crystals. The endotherm along with the transformation observed in the Raman spectrum indicates that the product crystals are a hydrate of CA, and as time goes on the water is lost from the crystals due to phase transformation.

To conclusively prove the crystals are CA hydrates, DSC experiment was also conducted on the same crystals after the transformation was observed in the Raman spectrum. Figure 2.10B shows that there is no endotherm near 100 °C after the transformation was observed in the Raman spectrum. This proves that the product crystals are hydrates, and as time passes the water is slowly lost from the crystals. The formation of CA hydrates seen here agrees with past studies,[13] where it has been reported that CA will form a hydrate when crystallized from acetone if the solvent contains more than 10 wt % water. This previous study did not analyze the crystals over time to investigate the dehydration of the crystals. The Raman approach of the present study uniquely allows tracking of the crystal phase during the various steps of the crystallization process.

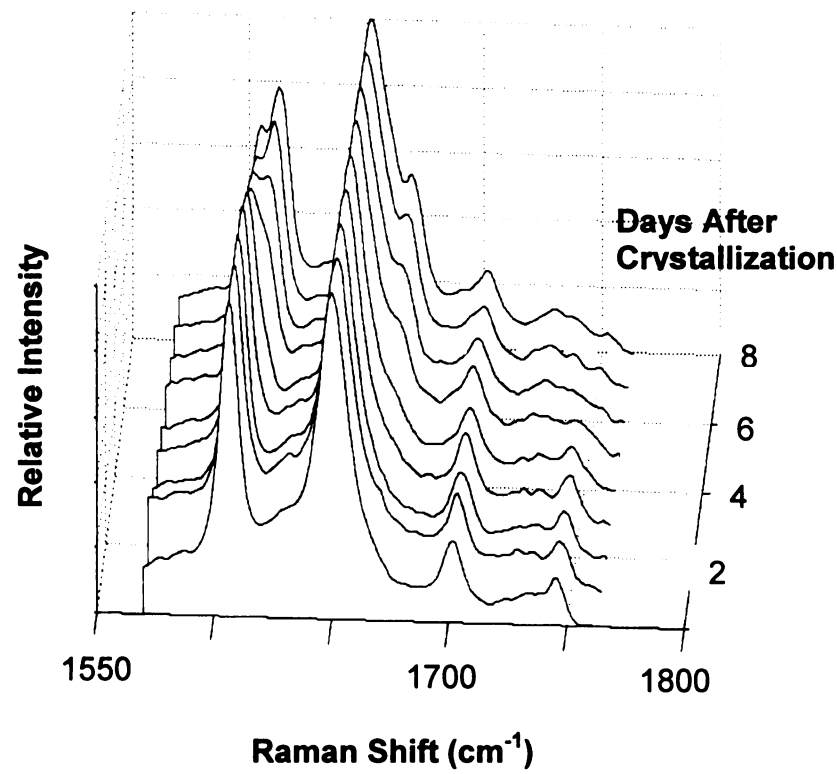

Figure 2.9. Time resolved Raman spectra of cortisone acetate acquired daily to monitor post crystallization phase transformation. The first spectrum in was acquired the day of crystallization (day 0 after crystallization). The final spectrum was acquired 8 days after crystallization.

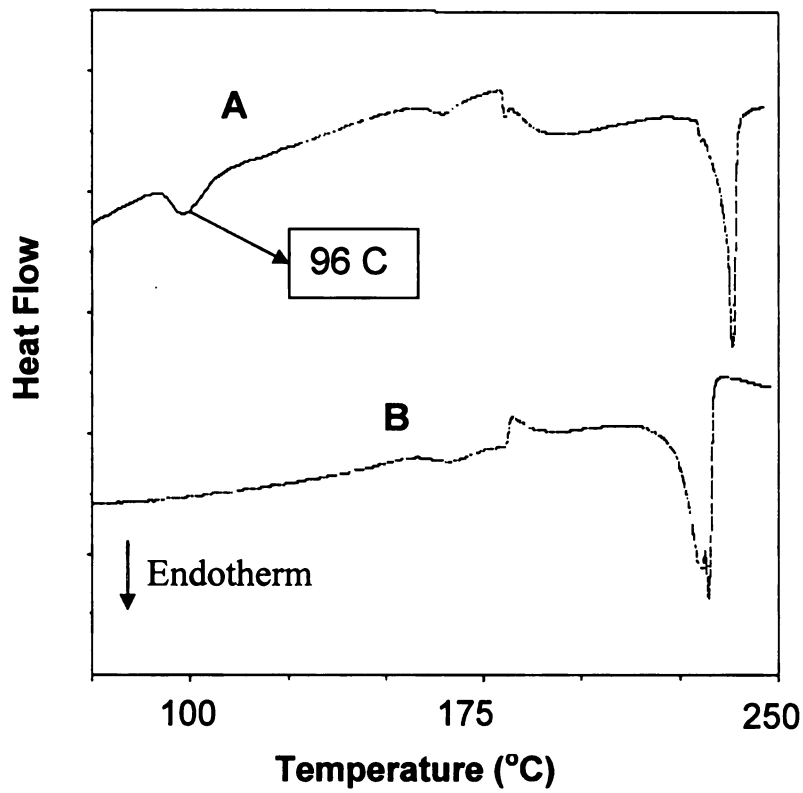

Figure 2.10. The DSC thermograms of (A) CA hydrate and (B) same crystals after loss of water. Apparent endotherms or exotherms at around 180 C are due to change in the temperature program heating rate.

2-4.5 Effect of Impurity

Impurities can serve as tailor-made additives that alter the solid-state form produced from particular crystallization conditions.[11] The impurity chosen for the current study was BA. Figure 2.11 shows the molecular structure of BA. This molecule meets the criteria, which have been discussed extensively[14-16] for tailor-made additives. That is, BA is structurally similar enough to CA to be incorporated into the CA crystal lattice, but BA also has differences in its structure that should disrupt the growth of the CA crystal lattice.

The Raman spectra obtained for the crystallizations where BA was present were identical to the CA hydrate spectra that were obtained for all the other crystallizations without BA. The addition of BA appeared to have no effect on the solid-state form that crystallized (under the conditions used). Even though BA failed to provide a different solid-state form, the dried crystals were monitored daily. During the monitoring of the crystals, it became evident that the crystals with BA added to them took considerably longer to dehydrate. Figure 2.12 shows the peak width in the region between 1600 and 1640 cm^{-1} versus the number of days after crystallization for three crystallizations performed at 0.50 mL/min without BA.

The crystallization was performed in triplicate to ensure that the dehydration time used for comparison was statistically meaningful. From Figure 2.12, it can be seen that all three crystallizations required 3 days for the dehydration to begin. To complete the dehydration, the crystallizations required 5.33 (1.53 days. Figure 2.13 shows the peak width versus the number of days after crystallization for the solutions with BA. The three crystallizations were conducted at a water addition rate of 0.50 mL/min with increasing

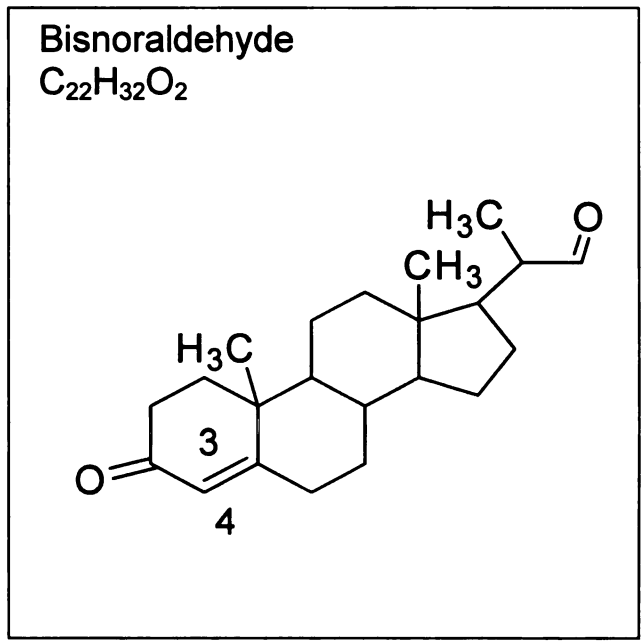

Figure 2.11. Molecular structure of bisnoraldehyde

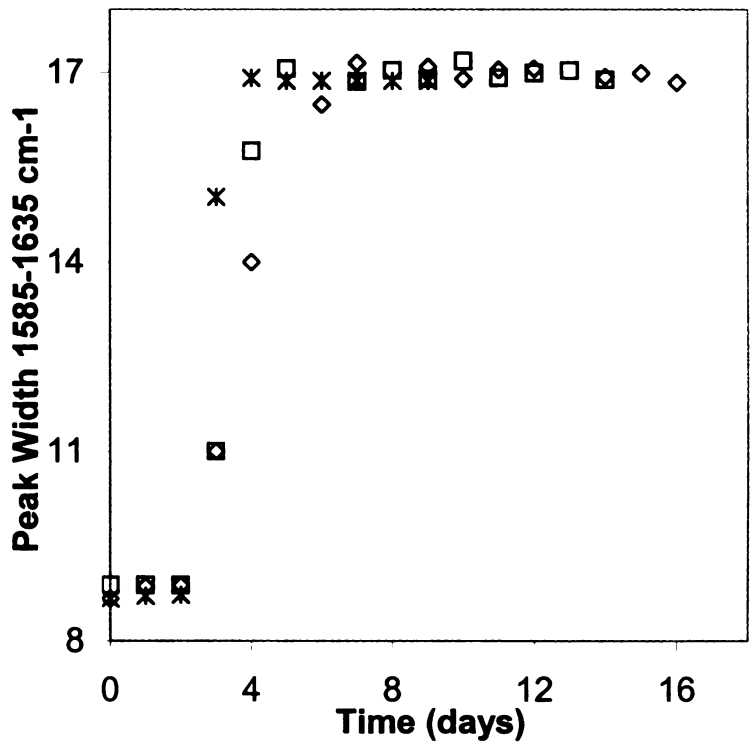

Figure 2.12. Peak width of the Raman spectrum of cortisone acetate between 1585-1635 cm^{-1} for three crystallizations conducted with a water addition rate of 0.50 mL/min. All three crystallizations required three days for dehydration to begin which is reflected by the increase of peak width. Dehydration required 5.33 ± 1.53 days for completion. .

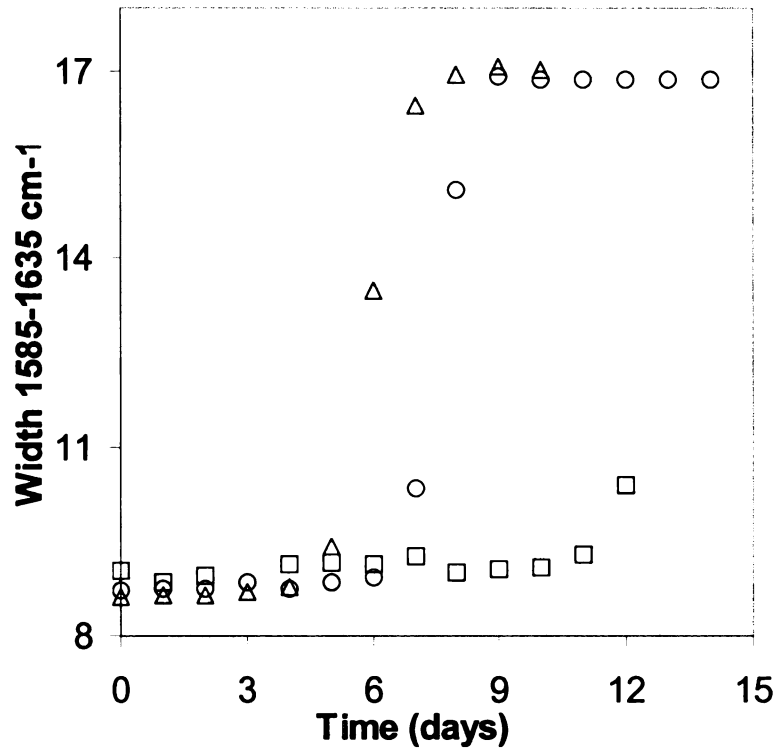

Figure 2.13. Peak width of the Raman spectrum of cortisone acetate between 1585-1635 cm^{-1} for three crystallizations in the presence of bisnoraldehyde. The crystallization at 0.04 weight percent BA in solution(Δ) shows no statistically meaningful difference from the reference crystallizations. The crystallization with 0.15 weight percent BA in solution (O) required seven days for dehydration to begin and 12 days for dehydration to be completed. Finally, the crystallization with 0.22 weight percent BA in solution (□) had not begun dehydration after 12 days.

amounts of BA added. The crystallization with the smallest amount of BA shows no statistically meaningful difference from the crystallization with no BA added. The two other samples with higher concentrations of BA demonstrated a significant increase in the number of days required for dehydration. The sample from second highest BA containing solution required 6 days for dehydration to begin and 9 days for the dehydration to be completed. The sample from the solution with the most BA began to dehydrate 12 days after crystallization occurred, which is approximately a five to six times increase in the number of days required for dehydration when compared to the "reference" experiments. The morphology of the crystals did not change and the Raman spectrum looks identical to the Raman spectrum of a sample without BA.

2-4.6 Principal Components Analysis (PCA)

The goal of this analysis was to investigate the possibility of identifying and isolating subtle features that are part of the Raman spectra that are susceptible to changes in solution structure, for utilization in measurement of precrystallization phenomena. The arrangement or rearrangement of solute molecules in solution (caused by supersaturation or nucleation) should be manifested in Raman spectral features such as shifts in peak positions and changes in peak areas and or peak widths. These variations in spectral features may not be readily apparent in the raw spectra. Techniques such as spectral deconvolution[17,18] and derivative spectroscopy[17] have been used in the past to investigate the occurrence of these difficult to track changes in the spectra of crystallization experiments. PCA is a powerful mathematical technique that has not been used in the past to investigate crystallization experiments. PCA of the spectral data for the second set of experiments using the HoloReact software yielded 25 different factors. Using a percent

variance plot, it was determined that only the first three factors would have to be examined closely since they described 99.95% of the variance in the data. The first and second factor provided information that was readily apparent from the raw spectra. The third factor, however, yielded an interesting result. Figure 2.14 shows the third factor plotted versus time for the second set of crystallization experiments. The plots show an increase up to an apex and then a steady decrease. Using the mass balance from the crystallization experiments and the solubility curve presented above, it was possible to determine that the apex in all three plots corresponds with the point at which the solution becomes saturated. Therefore, using this technique, it is possible to determine the onset of supersaturation in the crystallization experiment. A full explanation of this phenomenon would involve a thorough discussion of PCA itself. That is beyond the scope of this work, so the interested reader is referred to a number of texts available.[19,20] A simplistic molecular level explanation of the trend in the data displayed from the third factor is that this factor is correlated to the interactions between solvent and solute during the water addition. As the solution becomes saturated and subsequently supersaturated, the changes in this interaction that take place are correlated to the variance displayed in the raw spectra. The purpose of this work is not to conclude that this effect is general to antisolvent crystallization or even to corticosteroid antisolvent crystallization. It is only intended to show that PCA is a powerful technique that may provide useful information about the crystallization phenomena beyond that which is obvious from the overall spectra.

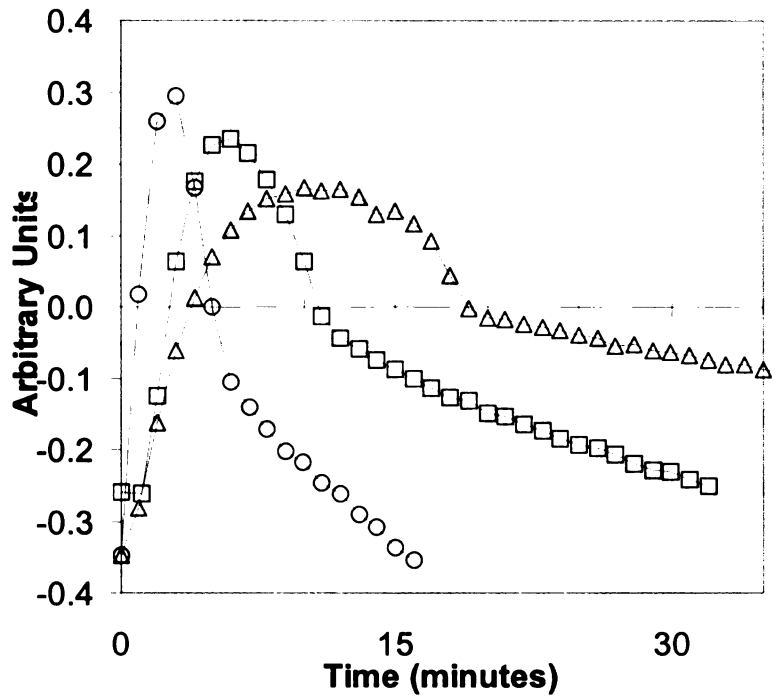

Figure 2.14. The third factor obtained from PCA of the Raman spectra of cortisone acetate in aqueous acetone solutions for the regions of 750-850 cm^{-1} and 1600-1630 cm^{-1} for the second set of crystallizations described in the text. The different symbols represent different water addition rates: (O) 0.25, (□) 0.50, (Δ) 1.0 mL/min. The solution becomes saturated at the first inflection point in time

2-5 Conclusions

The use of Raman spectroscopy was demonstrated for simultaneous monitoring of the crystallization process and of the solid-state form crystallizing during antisolvent addition crystallization. Raman spectroscopy is able to provide accurate information regarding not only the crystallization process such as ATR-FTIR and other methods, but it is also capable of providing information on the solid-state form during crystallization and subsequent unit operations such as drying. Finally, Raman spectroscopy was also used to monitor the dehydration of crystals during an extended storage time including the effect of an impurity on the transformation rate. These results provide further evidence that Raman spectroscopy can be very useful in rapid screening of different solid-state forms during processing or storage.

2-6 Acknowledgments

Kaiser Optical Systems, Inc. provided the Raman spectrometer and HoloReact software and Pharmacia Corporation provided the steroids used in this study. Their contributions are appreciated. Partial support of J.A.F. was received from a GAANN fellowship.

2-7 References

1. Threlfall, T. *Analyst* **1995**, *120*, 2435-2460.

2. *Polymorphism in Pharmaceutical Solids*; Brittain, H. G., Ed.; Marcel Dekker: New York, 1999.

3. Byrn, D. E.; Pfieffer, R. R.; Stowell, J. G. *Solid-State Chemistry of Drugs*, 2nd ed.; SCCI, Inc.: West Lafayette, 1999.

4. Battey, D. E.; Slater, J. B.; Wludyka, R. S.; Owen, H.; Pallister, D. M.; Morris, M. D. *Appl. Spectrosc.* **1993**, *47*, 1913.

5. Owen, H.; Battey, D. E.; Pelletier, M. J.; Slarter, J. B. *Proc. SPIE* **1995**, *24*, 260.

6. Silverstein, R. M.; Bassler, C. G.; Morril, T. C. *Spectrometric Identification of Organic Compounds*, 5th ed.; John Wiley & Sons: New York, 1991.

7. *The Merck Index*, 8th ed.; Stecher, P. G., Windholz, M., Leahy, D. S., Bolton, D. M., Eaton, L. G., Eds.; Merck & Co., Inc: New Jersey, 1968.

8. Prausnitz, J. M.; Lichtenthaler, R. N.; Azevedo, R. G. *Molecular Thermodynamics of Fluid-Phase Equilibria*, 3rd ed.; Prentice Hall PTR: New Jersey, 1999.

9. Dollish, F. R.; Fateley, W. G.; Bentley, F. F. *Characteristic Raman Frequencies of Organic Compounds*; Wiley-Interscience: New York, 1974.

10. Schwartz, A. M.; Berglund, K. A. *J. Cryst. Growth* **1999**, *203*, 599.

11. Feng, L.; Berglund, K. A.; *Cryst. Growth Des.* **2002**, *2*, 449.

12. Ansari, R. R.; Suh, K. I.; Arabshahi, A.; Wilson, W. W.; Bray, T. L.; DeLucas, L. J. *J. Cryst. Growth* **1996**, *168*, 216-226.

13. Kuhnert-Brandstatter, M.; Gasser, P. *Microchem. J.* **1971**, *16*, 590.

14. Weissbuch, I.; Leiserowitz, L.; Lahav, M. In *Advances in Crystal Growth Research*; Sato, K., Nakajima, Y., Furukawa, Eds.; Elsevier Science B.V.: Amsterdam, 2001; Chapter 23.

15. Kuzmanko, I.; Rapaport, H.; Kjaer, K.; Als-Nielsen, J.; Weissbuch, I.; Lahav, M.; Leiserowitz, L. *Chem. Rev.* **2001**, *114*, 1659-1696.

16. Weissbuch, I.; Lahav, M.; Leiserowitz, L. *Adv. Cryst. Growth Res.* **2001**, 381-400.

17. Dunuwila, D. D.; Berglund, K. A. *Trans. I. ChemE* 1995.

18. Cerreta, M. K.; Berglund, K. A. *J. Cryst. Growth* **1987**, *84*, 577-588.

19. Malinowski, E. M. *Factor Analysis in Chemistry*; John Wiley & Sons: New York, 1991.

20. Beebe, K. R.; Pell, R. J.; Seasholtz, M. B. *Chemometrics: APractical Guide*; John Wiley & Sons: New York, 1998.

Chapter 3

IN SITU MONITORING OF ANTI-SOLVENT ADDITION CRYSTALLIZATIONS WITH PRINCIPAL COMPONENTS ANALYSIS OF RAMAN SPECTRA *

*Crystal Growth and Design, **2004**, 4(3), 457-463.

3-1 Abstract

Fiber optic Raman spectroscopy was used for *in situ* monitoring of anti-solvent addition crystallization of progesterone. Raman spectral features of the solute and the anti-solvent were subjected to principal components analysis (PCA) in order to attempt to obtain information which is not readily apparent from the raw spectral data. For the system utilized, PCA was able to distinguish spectral features from the solute in solution, the solute crystals and the anti-solvent. Furthermore, PCA was capable of detecting subtle changes in the spectral data (as the addition of anti-solvent progressed) that could be used as a warning for the onset of crystallization. The current study demonstrates the advantages that can be gained by combining PCA with Raman spectroscopy for monitoring crystallizations *in situ*.

3-2 Introduction

Monitoring and control of the crystallization of active pharmaceutical ingredients (API) are important to the pharmaceutical industry. This importance is due in large part to the pharmaceutical industry's need to satisfy regulatory authorities as to the morphology, polymorphism, crystal size and other properties of new chemical entities[1]. Pharmaceutical companies have also recognized that on-line or *in situ* monitoring of crystallizations will greatly aid in the reproducibility of results and in detecting problems

that may arise during crystallization. Consequently, *in situ* monitoring of crystallizations will reduce money and time spent in reworking "failed" crystallizations.

The use of Raman spectroscopy to monitor crystallization processes *in situ* offers many advantages over using turbidity or nephelometry measurements[2]. Even with the advantages afforded, Raman spectroscopy has yet to meet the expectations placed on it regarding crystallization monitoring[3]. The formation of solution structures (caused by supersaturation or nucleation) should be noticeable in the Raman spectrum. Peaks arising from the solution structures should provide information regarding the intermolecular interactions (e.g. hydrogen bonding) that are present in the solid-state phase[3] and could help to predict the solid-state form that ultimately crystallizes. The appearance of bands related to these kinds of interactions could also be used as a signal of the imminence of crystallization.

The foregoing discussion is based on a solid theoretical foundation; however, to the authors' knowledge there have been few results reported in this area. Some studies have reported the detection of solution structures[4,5] in supersaturated solutions, but the solution structures were found to be unrelated to the crystal structure. A possible explanation for the lack of results in this area could be the difficulty in interpreting the spectral data obtained. The kinds of solution structure interactions described above are expected to have varying effects on the Raman spectrum of a sample. For example, the interactions could cause: new peaks to appear, changes in the intensity of existing peaks, peak shifts, changes in peak width, variations in the baseline of the spectrum and probably a combination of the listed changes. It is also likely that any bands related to the solution structure interactions would overlap with existing solvent or solution bands, thus masking

their appearance. Another factor that makes data interpretation difficult is the concentration of the crystallizing species in solution. Many APIs are not readily soluble in organic solvents and are often present in relatively low concentrations compared to the solvent. The low concentration of the API in solution combined with the strong Raman scattering properties of many organic solvents often leads to small, broad bands from the crystallizing species. A final consideration for the lack of results is that crystallizations are dynamic experiments with at least one condition varying at all times. Two of the most common crystallization techniques are cooling and anti-solvent addition. Temperature changes used in cooling crystallizations and the introduction of another compound to a solution (anti-solvent addition crystallization) are both known to impact the Raman spectrum (strongly dependent on the sample). With these variations factored in, it becomes even more difficult to single out any changes in the Raman spectrum that are due solely to any solution structure phenomena.

For these reasons, multivariate analysis, and in particular principal components analysis (PCA) seems well suited for processing spectral data for anti-solvent addition crystallization experiments. PCA is purely a mathematical technique whose goal it is to reduce the dimensionality of a data matrix.

3-3 Experimental Section

3-3.1 Materials and Instrumentation

Solutions used in the crystallization experiments were prepared with de-ionized water and analytical grade acetone (J.T.Baker, Phillipsburg, NJ). Progesterone (PG) was provided by Pharmacia Corporation (Kalamazoo, MI) and was used without further purification. Crystallizations were conducted in a 60 mL glass water-jacketed reactor.

The temperature of the water jacket was maintained at 22.4 ± 2.0^{0}C using an RTE-140 bath/circulator with microprocessor controller (NESLAB, Postmouth, NH). Water addition rates and total water added volumes were controlled with a 665 Dosimat (Metrohm Ltd., Switzerland) water pump. A schematic diagram of the experimental setup is shown in Figure 3.1. All crystallizations were performed using the same size stir bar with the same stir rate.

Raman spectra were collected using a HoloLab Series 5000 instrument provided by Kaiser Optical Systems, Inc. Details of the HoloLab 5000 have been described previously[6,7]. Briefly, a 100 mW external cavity stabilized diode laser at 785 nm is used for sample illumination. A CCD camera, a spectrograph, and a fiber optic probe complete the HoloLab 5000 system. Remote sampling was accomplished by employing a fiber optic probe attached to an immersion optic to focus the incident beam into the solutions. The positioning of the immersion optic within the crystallizer was maintained constant through out all the experiments. This positioning ensured that any effects the immersion optic may have had on the crystallization impacted all the experiments equally.

3-3.2 Calibration of Raman Spectra

The Raman spectra of standards were used to construct a multiple linear regression (MLR) model using the MATLAB (The MathWorks, Inc.) based HoloReact™ software provided by Kaiser Optical Systems, Inc. The model consists of eleven standard solutions ranging in concentration from 1.01 to 8.22 weight percent of PG, from 56.96 to 88.45 weight percent acetone and from 10.03 to 39.99 weight percent water.

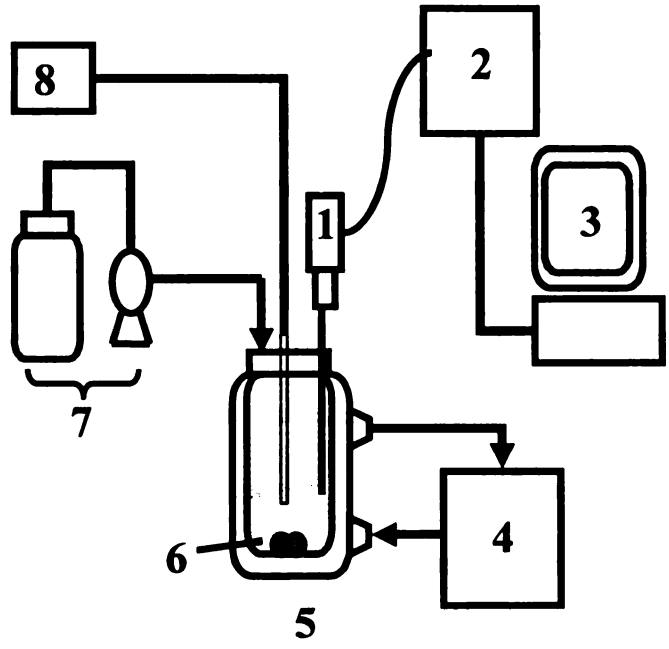

Figure 3.1. Schematic of the experimental setup. (1) Raman probe, (2) HoloLab 5000, (3) PC, (4) water circulator, (5) jacketed reactor, (6) magnetic stir bar, (7) water reservoir and pump, (8) digital thermometer.

3-3.3 Anti-Solvent Addition Crystallizations

For all crystallization experiments, binary solutions of acetone and PG were prepared as the starting point. The solutions were stirred in the glass-jacketed reactor for 2 hours to ensure dissolution of PG. Once this was achieved, water was added continuously to the solutions. For all sets of experiments three different water addition rates were used, 0.25, 0.50 and 1.00 mL/min (except for the set of crystallizations used for reproducibility [see (a) below], where the water addition rate was 0.5 mL/min). For all experiments, 10.3 mL of acetone comprised the initial solution and 12 mL was the total volume of water added. During the continuous addition of water the crystallization was monitored by continuously acquiring Raman spectra of the solution. The spectra were acquired using 10 second acquisition time and 10 second intervals between spectra.

3-3.4 Reproducibility Crystallizations (a)

A replicate set of three crystallizations initially contained 7.0wt% PG. These crystallizations were performed in order to demonstrate the reproducibility of the experimental results.

3-3.5 Blank Experiments (b)

For this set of three experiments water was added to neat acetone. The results were used as "blanks" for comparison purposes.

3-3.6 Varying Initial PG Concentration Crystallizations (c)

Three sets of three crystallizations were performed. The first set of three contained an initial PG concentration of 3.5wt %, the second set contained 7.0wt % PG, and the third set contained 14.0wt % PG.

3-3.7 Principal Components Analysis (PCA)

The Raman spectra obtained were subjected to PCA using two different software packages, HoloReact™ and PLS_toolbox (Eigenvector Research, Inc.). Holoreact™ and PLS_toolbox are MATLAB based software and both use singular value decomposition (SVD) for the PCA calculations. In order to perform the SVD calculations the software packages use the *svd* command found in MATLAB. MATLAB's *svd* command[8] uses a version of the LINPACK[9] routine ZSVDC for the SVD calculations. HoloReact™ was used to collect the spectral data and analyze it *in situ;* PLS_toolbox was used for all post experiment data analysis.

All the spectral data were mean centered before being subjected to PCA, this was the only data pre-processing performed. The region selected for analysis was 1594-1688 cm^{-1}. Examination of the scores and loadings for the most important principal components (PCs), as determined from percent variance plots, were used to investigate changes in the spectral features of the Raman data.

3-4 Results and Discussion

3-4.1 Calibration of Raman Spectra

Raman spectra of standard solutions were collected and subjected to the MLR calibration analysis. The peak regions selected to correlate spectra and solution concentrations were 750-850 cm^{-1} and 1600-1630 cm^{-1}. The standard error of prediction (SEP) determined by a leave-one-out cross validation was 0.11 PG weight percent and the standard error of calibration (SEC) determined by a leave-one-out cross validation was 0.06 PG weight percent.

The 750-850 cm^{-1} region was chosen because it contains the 787 cm^{-1} acetone band assigned to the C-C(=O)-C symmetric stretch[10]. This band provides the model with the spectral changes caused by the various concentrations of acetone and water present in the standards. The vibrational band found in the 1600-1630 cm^{-1} region provides the model with the spectral changes caused by the different concentrations of PG used in the standards. The presence of this band in the spectrum can be explained by conjugation theory[11]. Figure 3.2 shows the molecular structure of PG. The conjugation between the C=O at position 3 and the C=C at position 4 results in the delocalization of the π electrons and reduces the double-bond character of both sets of double bonds. This causes the Raman scattering to occur at lower wavenumbers than those of un-conjugated systems. Using this interpretation, the peak found between 1600-1630 cm^{-1} in the spectra is assigned to C=C vibrations.

3-4.2 Solubility Curve

PG solubility in acetone/water solutions of varying compositions at 22.4 ± 0.5 ^0C was determined using the MLR model described above. Figure 3.3 shows the solubility curve of PG determined via this procedure. Each point on the curve is the average of at least three measurements. The error bars represent the standard deviation of the three measurements.

Solid PG in excess of solubility was added to solutions initially containing 49.85/50.15, 58.75/41.25, 73.46/26.54, 87.81/13.19, 89.99/10.00 weight percent acetone/water. Each solution was stirred for twenty-four hours to ensure equilibrium was achieved. Raman spectra from the liquid phase were collected and the PG concentration was determined

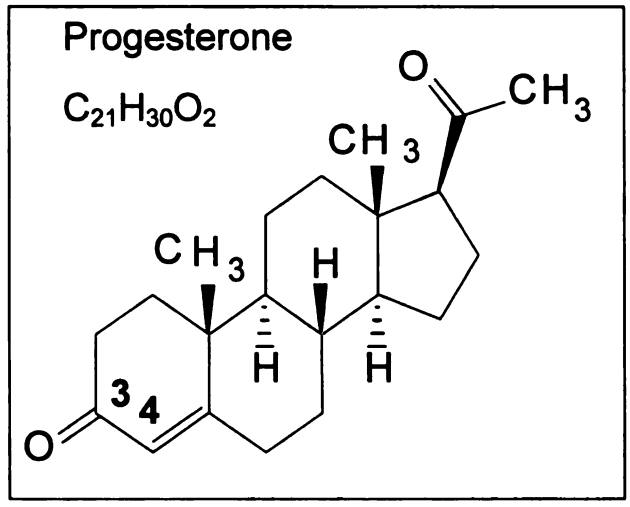

Figure 3.2. Molecular structure of progesterone (PG).

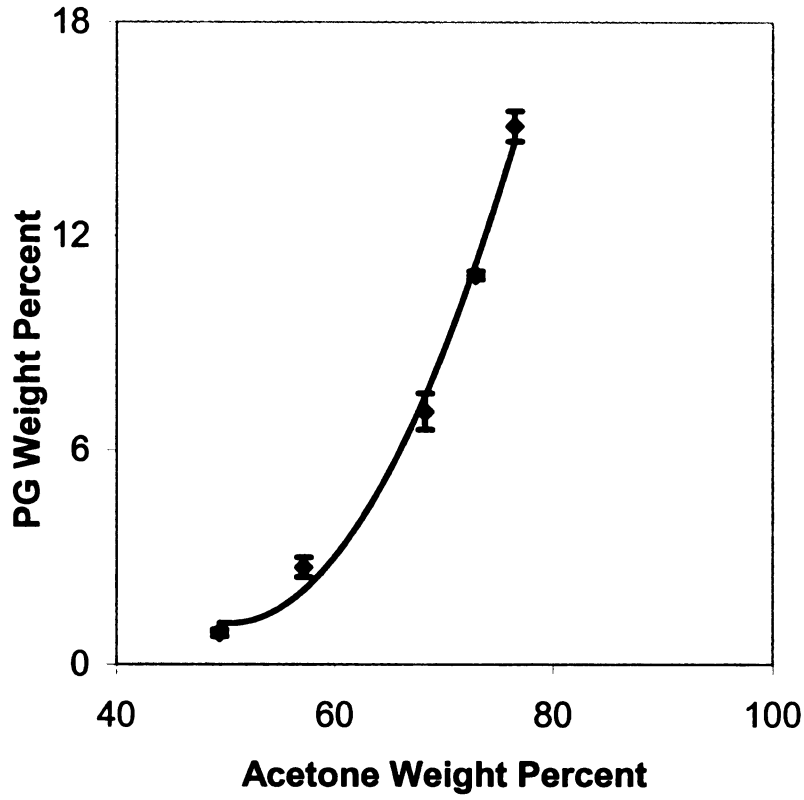

Figure 3.3. Solubility of progesterone in binary mixtures of acetone/water at 22.4 °C.

using the MLR calibration. The solubility of PG was found to be within the expected limits found in the literature[12,13] for PG dissolved in neat water and neat acetone. The solubility of PG was used to determine the concentrations that could be used in the anti-solvent crystallization experiments. Also, the solubility data were used to monitor the progress of the crystallizations.

3-4.3 Anti-Solvent Addition Crystallizations

The PG and acetone concentrations decrease as water is added to the solution. As more water is added into the solutions the solubility of PG decreases. Eventually, the water addition drives the PG concentration beyond solubility. Continued water addition beyond this point ensures that eventually the solution will no longer be able sustain the level of supersaturation and PG nucleates. The last phase is the growth of the crystals in a solution with near-depleted supersaturation. As described previously[2], it is possible to monitor this process *in situ* using Raman spectroscopy. Monitoring the crystallization process in this way provides invaluable information. However, the raw Raman spectral data without being subjected to a quantitative calibration does not provide a key piece of information: How close is the solution to the nucleation and/or crystallization point? Advanced warning regarding the impending point of nucleation and crystal growth would be useful in a variety of fields. A simple example of the usefulness of this would be in monitoring the reproducibility of the crystallizations and reproducibility of the crystal physical properties. Another example would be the possibility of altering the crystal size distribution by stopping the addition of anti-solvent at a certain time before crystallization occurs.

3-4.4 Principal Components Analysis (PCA)

The goal of this analysis was to investigate the possibility of identifying and isolating subtle features of the Raman spectrum that are susceptible to changes in solution structure for utilization in measurement of pre-crystallization phenomena. The arrangement or rearrangement of solute and solvent molecules (caused by supersaturation or nucleation) should be manifested in Raman spectral features such as shifts in peak positions and changes in peak areas and/or peak widths. These variations may not be readily apparent in the raw spectra. The system chosen for this work represents a good example, not only for subtle changes in the spectrum, but also for the difficulty in interpreting changes that occur to the spectra during crystallization. Figure 3.4 shows the Raman spectral data for a typical experiment. It can be seen from Figure 3.4 that there are at least three different changes occurring as water is added. The signal intensity, the peak position and the baseline of the spectra are changing as water is added to the solution. In the past, techniques such as spectral deconvolution[4] and derivative spectroscopy[5] have been used to investigate the occurrence of these difficult to track changes in the spectra.

PCA is a powerful mathematical technique that has not been used in the past to investigate crystallization experiments. Two matrices are obtained from the analysis. The loadings matrix shows the relationship of the variables to each other and to the principal components. The scores show the similarities and differences between the samples based on the principal components.

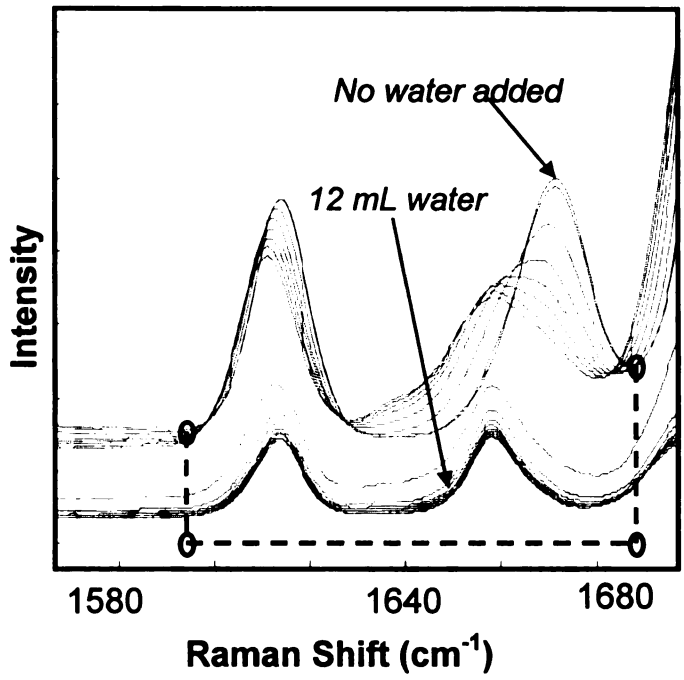

Figure 3.4. Raman spectra obtained for a PG crystallization experiment with an initial PG concentration of 7.0wt %. The region enclosed by the dashed lines is the region being investigated with PCA.

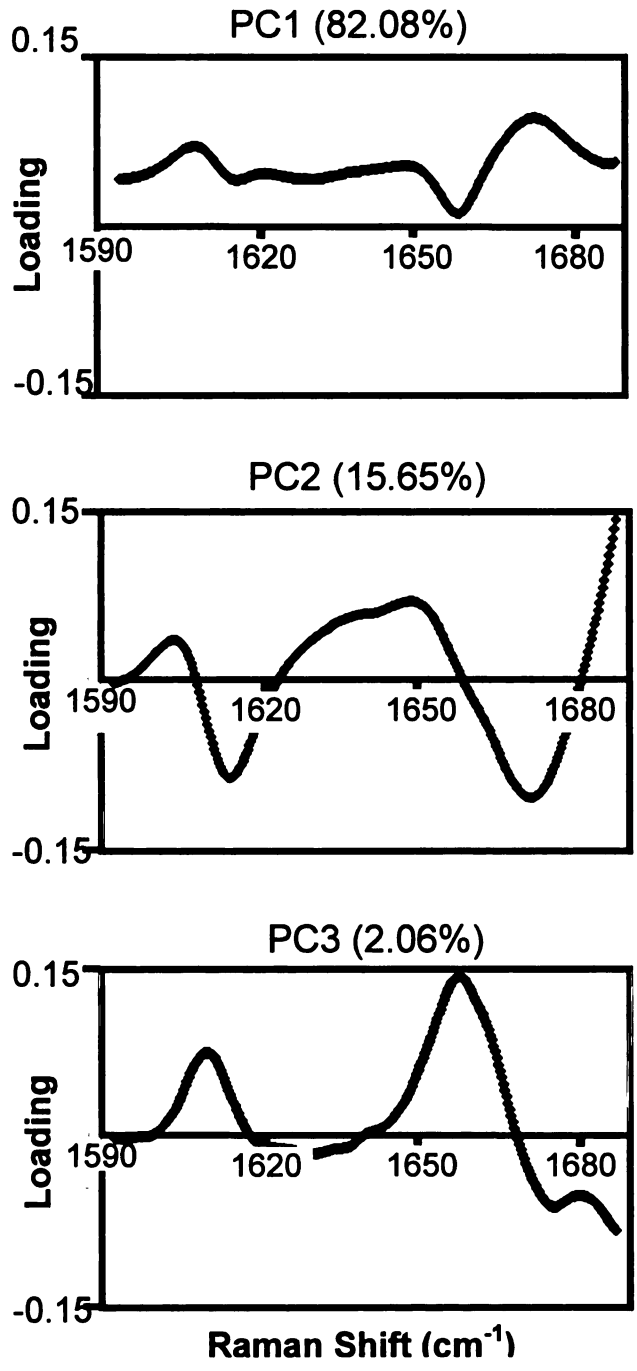

Figure 3.5. Principal component loadings of Raman spectra obtained from an initial PG concentration of 7.0wt %. (PC 1) is the first principal component, (PC 2) is the second principal component, (PC 3) is the third principal component.

3-4.5 PCA of Reproducibility Crystallizations

Three crystallizations were performed in order to demonstrate the reproducibility of the results. The data shown in this section are presented for comparative purposes only and are not discussed in depth with relation to the interpretation of changes relating to the crystallization experiments. Figure 3.5 shows three major principal component (PC) Figure 3.5 is presented in order to illustrate how the changes in the Raman spectra translate into loading plots of the PCA.

The three data sets obtained for the reproducibility analysis were used to construct one PCA model. Figure 3.6 displays the graph of PC1 scores versus PC2 scores for this model. Without performing the standard deviation calculations it is evident that the scores of the values are similar for the three data sets. This similarity between the scores values for the three data sets indicates that experimental results are reproducible when comparing crystallizations with the same initial concentrations and the same rate of water addition. It is important to note here that the present work does not use the values of the scores in order to monitor the progress of the crystallizations. Only the "trend" that the scores plots display (as seen in Figure 3.6) is used to monitor the crystallization process.

3-4.6 PCA of Blank Experiments

"Blank" experiments were performed in order to simplify data analysis. Inspection of the data from the blank experiments was used in order to investigate the effects of continuous water addition on the PCA calculations and results. These experiments also ensured that acetone-water interactions would not be mistaken for crystallization phenomena. Figure 3.7 shows the Raman spectra collected for one blank experiment with a water addition rate of 0.5 mL/min. Similar to Figure 3.4, Figure 3.7 displays the

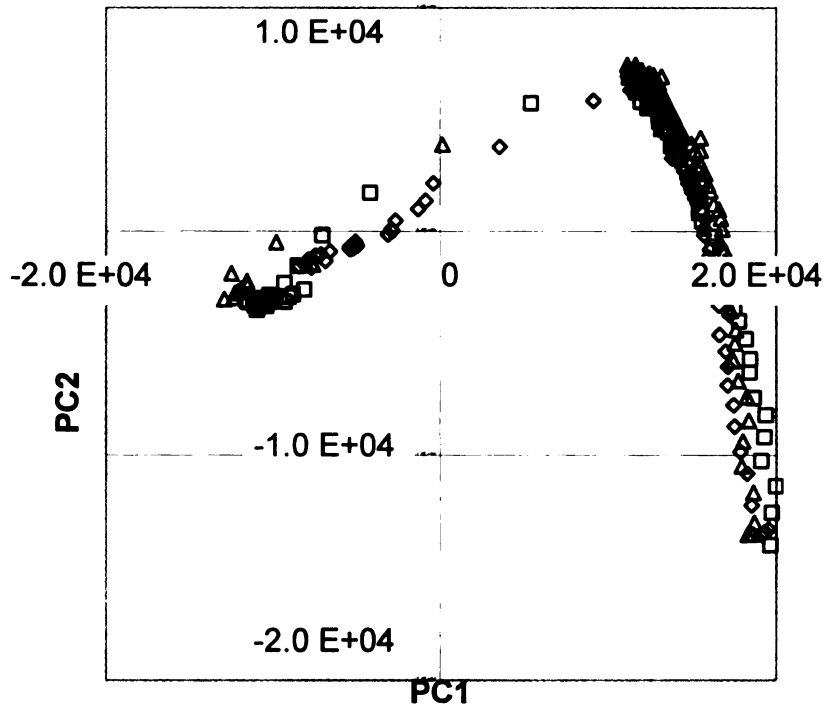

Figure 3.6. Scores plots for the three reproducibility crystallization data sets. The scores were calculated by constructing one PCA model using the three data sets. The similarity between the scores values indicates the reproducibility of the experiment. Arrow indicates direction of increasing water concentration.

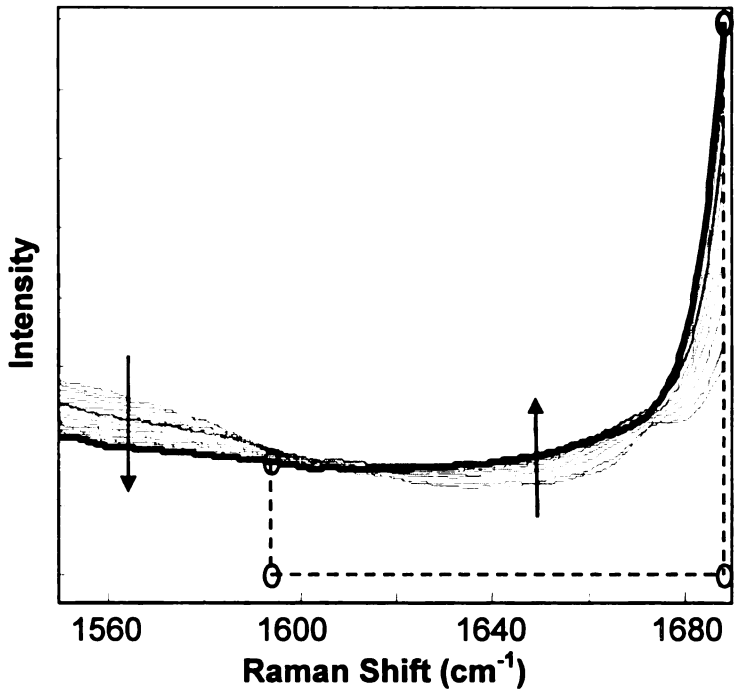

Figure 3.7. Raman spectra obtained for a "blank" experiment (no PG present). The region enclosed by the dashed lines is the region being investigated with PCA. Arrows highlight how the spectra change as water is added.

changes that occur to the region of interest in the Raman spectra as water is added to the initial solution. Figure 3.8 shows the first two PC loadings for the data shown in Figure 3.7, the two loadings account for 99.78% of the variance in the data. The loading plot for PC 1 in Figure 3.8 appears to have two major features. The first feature is the broad band that begins at 1594 cm^{-1} and ends at approximately 1665 cm^{-1}. In the region between 1594 and 1665 cm^{-1} Figure 3.7 shows that there is an increase in signal intensity as water is added. The increase in intensity can be explained by considering that even though water is known to be a weak Raman scatterer, it still has a Raman spectrum. One of the features of the water Raman spectrum is a broad band near 1645 cm^{-1} that arises from the H-O-H bending modes of the molecules[14]. As water is added, almost every region in the spectrum should display decreases in signal intensity (since most of the visible bands are due to acetone). However, the regions of the spectrum that coincide with the Raman water bands should increase in signal intensity.

The second major feature seen in the Figure 3.8 PC 1 loading plot is the large increase along the PC 1 axis in the region between 1670 and 1688 cm^{-1}. Figure 3.7 shows a peak shifting into this region. The peak that is shifting is due to C=O stretching of acetone molecules[10]. With no water added the peak is centered on 1706 cm^{-1}, after 12 ml of water are added the peak is centered on 1695 cm^{-1}. As the peak shifts the signal intensity changes for the Raman bands in the area of interest, this is detected by PCA and displayed in PC 1 on Figure 3.8. Using the preceding discussion, it can be concluded that PC 1 is affected mostly by the changes in signal intensity caused by water addition.

The PC 2 loading plot in Figure 3.8 displays similar features to those seen in the PC 1 loading plot. The PC 2 loading plot demonstrates that PC 2 is influenced by the change

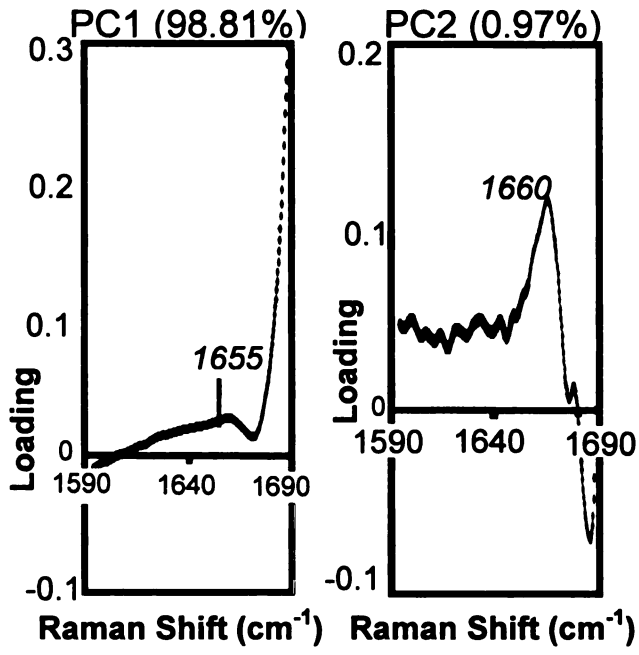

Figure 3.8. Principal component loadings of Raman spectra obtained from a "blank" experiment (no PG present). (PC 1) is the first principal component, (PC 2) is the second principal component. Numbers in *italics* indicate peak position in cm^{-1}.

in signal intensity at Raman shifts below 1640 cm^{-1}. There is a significant feature beginning at 1640 cm^{-1} and also a rapid decrease in values along the PC 2 axis from 1670 to 1688 cm^{-1}. This indicates that PC 2 is being influenced by the appearance of the water band and the peak shift that also affect PC 1. PC 2 is describing subtle additional information that is not described by PC 1. PC 1 describes 98.84 % of the variance while PC 2 describes only 0.81 % of the variance. For the blank experiments PC 1 alone is capable of describing most of the variance in the data. Figure 3.9 is a plot of cumulative water volume versus the scores for PC 1. This plot demonstrates how PC 1 is capable of describing the behavior of the samples in the data set (this figure is identical to a graph of signal intensity versus cumulative water volume for the raw spectral data [data not shown]). As water is added to the solution at a constant rate, the signal intensity of water should increase and the signal intensity of acetone should decrease. The increase or decrease of signal intensity is not expected to be linear (as might be expected with a constant water addition rate) since Raman spectroscopy is affected by concentration and not volume.

3-4.7 PCA of Varying Initial PG Concentration Crystallizations

As described in the experimental section above, three sets of three crystallizations were performed. Each set of three crystallizations was conducted with a different initial PG concentration. Figure 3.10 shows the loading plots of the first three PCs for crystallization experiments with initial PG concentrations of 3.5, 7.0 and 14.0 wt%. Separate PCA was performed for each set of three replicates at the different initial concentrations.

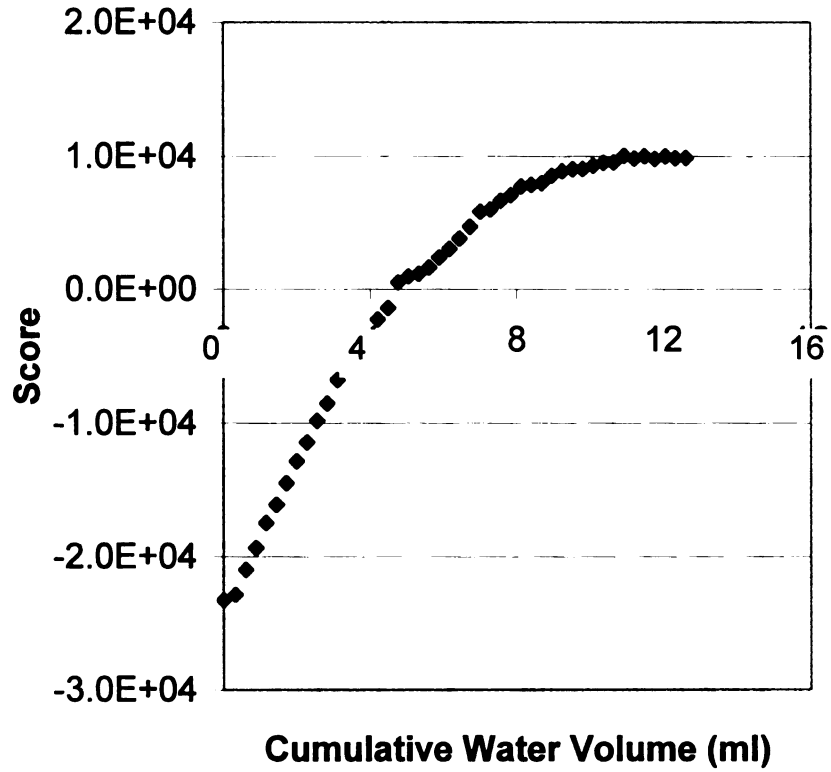

Figure 3.9. PC 1 scores versus cumulative water volume (ml) plot from a "blank" experiment (no PG present).

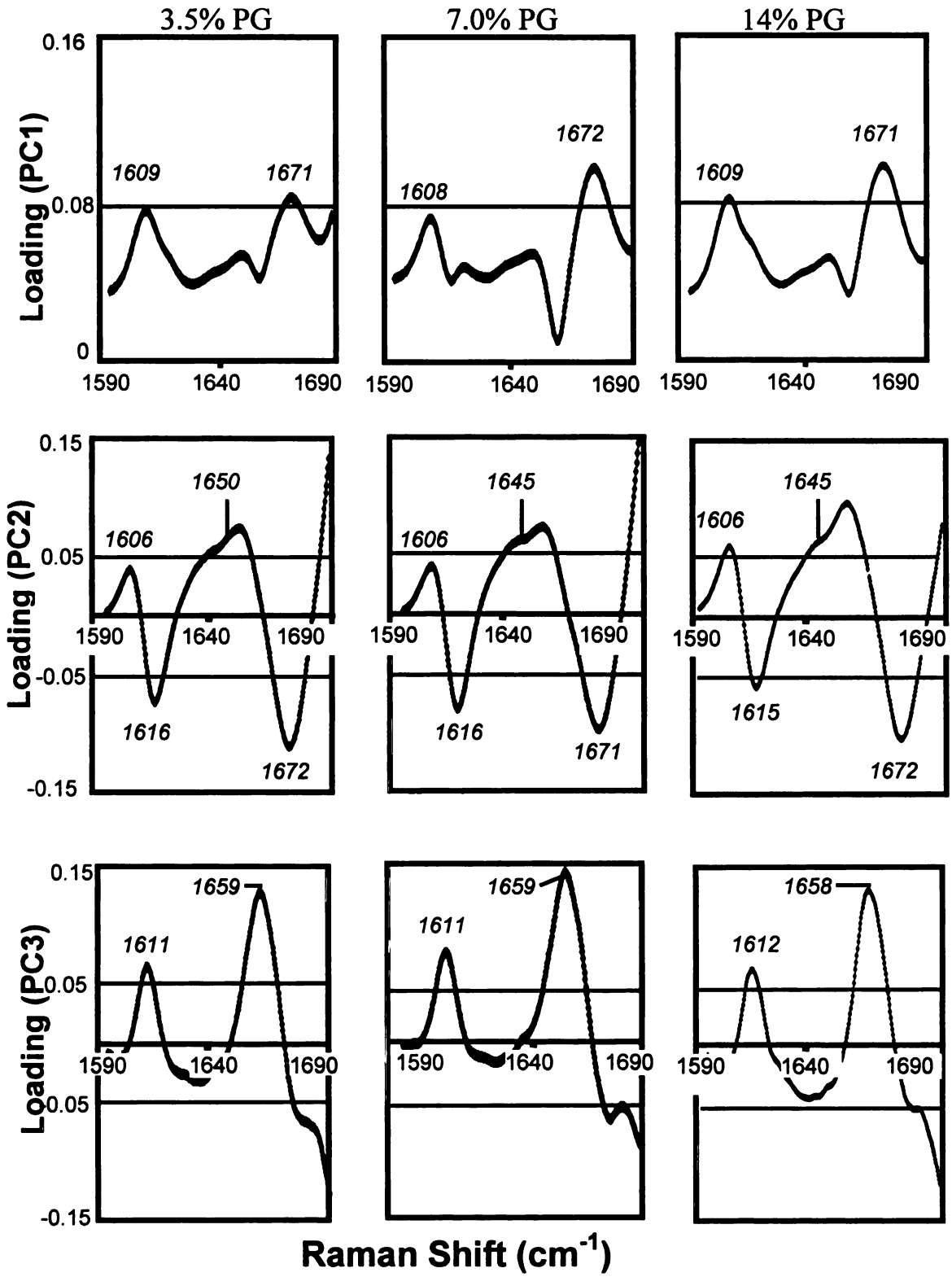

Figure 3.10. Principal component loadings of Raman spectra obtained for varying initial PG concentrations. (A) 3.5wt%. (B) 7.0wt%, (C) 14.0wt%. (PC1) first principal component, (PC2) second principal component, (PC3) third principal component. Numbers in *italics* indicate peak position in cm^{-1}.

In Figure 3.10 the loading plots of PC 1 for the three crystallization experiments demonstrate that 1609 and 1672 cm^{-1} are the Raman bands that have the most influence over PC 1. These features can be matched to the PG solution peaks for the C=C vibrations at 1610 cm^{-1} and the C=O vibrations at 1670 cm^{-1}. From that it can be concluded that PC 1 is most affected by decrease in intensity of the PG solution peaks observed as water is added.

In Figure 3.10 the PC 2 loading plots for all three crystallizations show that there are four main Raman bands that influence PC 2. The first two Raman bands can be addressed together, with features at 1606 and 1616 cm^{-1}. These two features in the PC 2 loading plots demonstrate the shift that the first solution PG peak (originally at 1610 cm^{-1}) undergoes as water is added. This peak shift can be seen in Figure 3.4, where the first PG solution peak begins at 1617 cm^{-1} and then shifts towards lower Raman wavenumbers as water is added to the solution (this is prior to crystallization, once crystallization occurs the peak shifts back to higher wavenumbers). The third feature of the PC 2 loading plots covers a broad range of wavenumbers (from 1620 to 1660 cm^{-1}). This feature is approximately centered on 1640 cm^{-1} and has already been interpreted as arising from water molecules in a previous section of this work. The fourth and final feature seen in the PC 2 loadings plots of Figure 10 is centered on 1670 cm^{-1}. This feature is due to the shifting (to lower wavenumbers) of the second PG solution peak as water is added. In addition, this feature also tails towards higher PC 2 values at 1688 cm^{-1}. This strong tailing is due to the peak shift (to lower Raman shifts) of the C=O band of acetone. Both of the peak shifts described above can be seen in Figure 3.4. Using the

above discussion it is possible to conclude that PC 2 is mostly influenced by changes in the Raman band positions caused by the addition of water.

Finally, it is possible to analyze the PC 3 loading plots for the three crystallizations shown on Figure 3.10. The PC 3 loading plots exhibit two main features. The first feature is centered on 1612 cm^{-1} and the second is centered on 1658 cm^{-1}. These features are a good match with the expected peak positions of crystalline PG. From the assignments above it can be concluded that PC 3 is mostly influenced by the formation of crystals in solution. This conclusion is corroborated by the fact that PC 3 loading plots display only random noise before crystallization occurs (data not shown). It is only after crystallization occurs that the PC 3 loading plots begin to be influenced by the crystalline PG Raman bands.

Examining the three PC 2 and PC 3 loading plots shown in Figure 3.10, it becomes evident that many of the variables have negative PC 2 and PC 3 loadings. It should be noted that only the absolute magnitude of the loading is discussed here. In some applications, the sign of the loadings have been utilized to make physical interpretations[15]; in this work the use is mainly in establishing the relative contributions of the variables to the PCs.

For that reason careful examination of the data must be undertaken when spectroscopic bands are correlated to PC loading plots. In the present work the correlations for all three PCs are simplified by the well-defined loading plots and the high resolution of the spectral data. In addition, the positioning of the loadings for each PC matches well with the raw Raman data.

In the discussion above regarding the influences of Raman shifts on the PC loading plots, all of the raw data from the crystallization experiment were used as input. When monitoring crystallizations *in situ*, this would not be the case. The data would be input sequentially as it was collected. The PCA results would not reflect the appearance of the solid until crystallization occurred. For this reason, PC 3 could not be used to monitor the crystallization *in situ*. Because PC 1 and PC 2 are influenced by the signal intensity from the PG, acetone and water in solution they are largely unaffected by the removal of the post crystallization data. This allows for *in situ* monitoring of the crystallization process using PC 1 and PC 2.

Figure 3.11 displays selected score plots for a crystallization conducted with a 7wt% initial PG concentration and a 0.5 ml/min water addition rate ([a] having the lowest and [d] having the highest water concentrations). The score plots were calculated *in situ*, as water was added to the initial solution spectra were acquired and immediately placed into the PCA data set (arrows indicate the direction of increasing water concentration). Beginning with score plot [a] it can be seen that PC 1 is capable of differentiating between the spectra according to water concentration. Score plots [b] and [c] demonstrate that as water is added PC 2 can also aid in differentiating the spectra with a noticeable change in slope for the data. Finally, score plot [d] shows how PC 1 and PC 2 can differentiate between PG in solution and crystalline PG suspended in a liquid.

The scores plots do not provide any information regarding the passing of the solubility limit for the solutions (the solubility limits do not correspond to any particular feature in the score plots), but they do seem to provide a fair amount of warning as to the impending crystallization. The change in slope along the PC 2 axis can be used as a

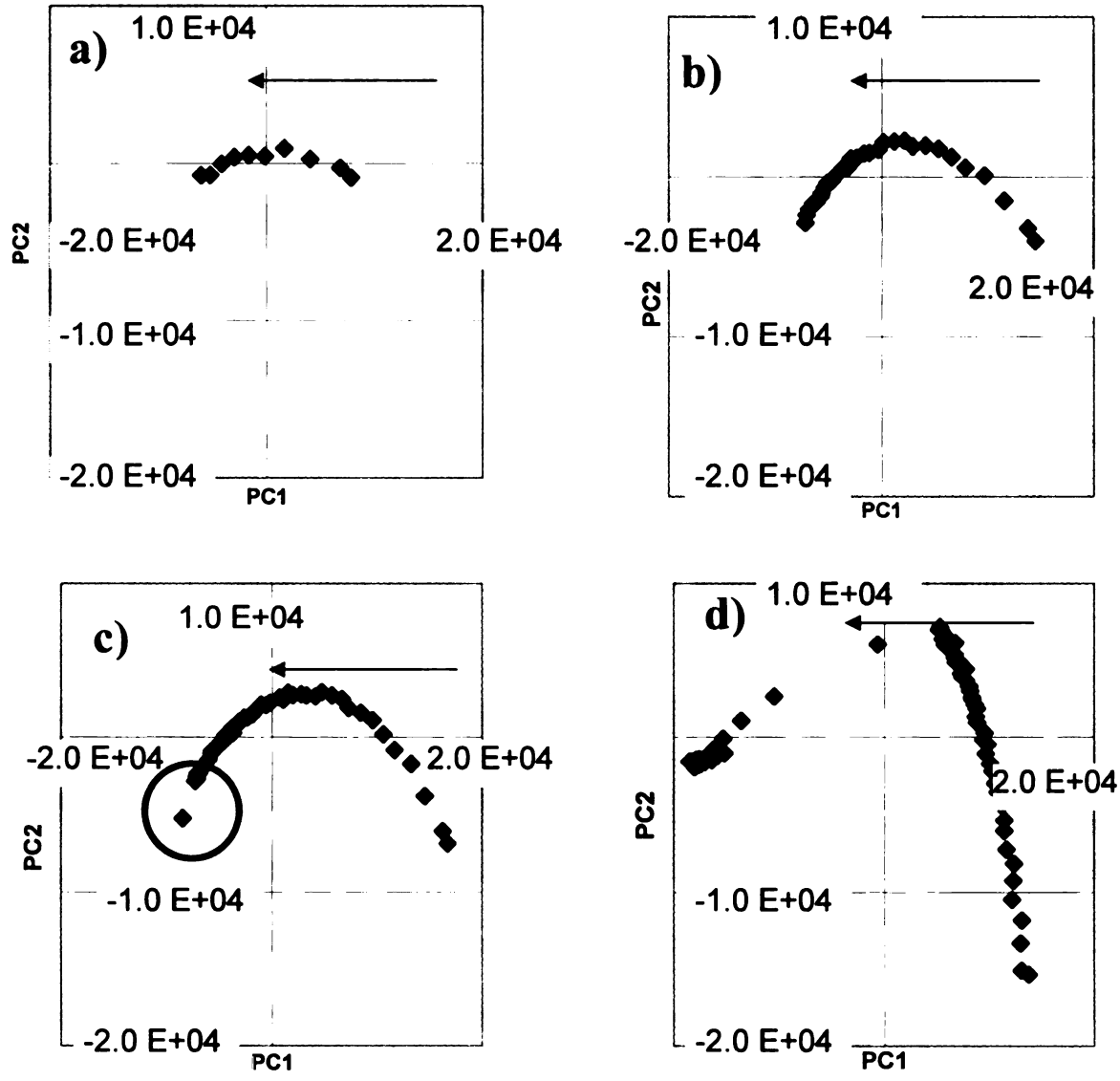

Figure 3.11. Principal components scores plot of Raman spectra obtained for crystallization with 7.0wt% initial PG concentration. The score plots were calculated after a specific volume of water was added to the original solution. a) 1.52 ml, b) 4.81 ml, c) 8.14 ml and d) 12 ml. Beginning of crystallization is circled in score pot c). Arrows indicate direction of increasing water concentration. The circled point on plot (c) indicates the beginning of crystallization.

warning of the onset of crystallization, and was reproducible in all the other crystallization experiments performed (data not shown). These results are promising for crystallization monitoring. PCA is able detect subtle changes in signal intensity that are not visible from the raw Raman spectral data. The detection of these slight changes provides a signal for the imminence of the approaching crystallization. In addition, PCA differentiates the spectral features of the three major "components" present in the region analyzed. That is, the spectral features of PG in solution mostly influence PC 1, water spectral features mostly influence PC 2 and the PG slurry spectral features mostly influence PC 3. This helps reveal the presence of a water band that is not readily apparent from the raw Raman data.

3-5 Conclusions

The use of PCA was demonstrated for aiding in the monitoring of anti-solvent addition crystallizations. For the region analyzed, PCA was able to distinguish spectral features from the solute in solution, the solute crystals and the anti-solvent. Furthermore, PCA was capable of detecting subtle changes in the spectral data (as the addition of anti-solvent progressed) that could be used as a warning for the onset of crystallization. It must be emphasized that the methodology introduced in this work must be considered system specific. It is expected that using a different system will yield vastly different results. For that reason, this work is only intended to show that PCA is a powerful technique that has not been used previously to study crystallizations. In this case PCA was able to provide useful information on crystallization phenomena beyond that, which was obvious from the raw spectral data.

3-6 Acknowledgments

Dr. David Burgard provided invaluable assistance in applying and understanding the results obtained from the PCA of the spectral data. Kaiser Optical Systems, Inc. provided the Raman spectrometer and HoloReact software and Pharmacia Corporation provided the steroids used in this study. Their contributions are appreciated. Partial support of J. A. F. was received from GAANN and Alfred P. Sloan Foundation fellowships.

3-7 References

1. Threlfall, T. *Analyst*, **1995**, 120, 2435-2460.

2. Falcon, J. A.; Berglund, K. A. *Journal of Crystal Growth and Design*, **2003**, 3(6), 947-952.

3. *Polymorphism in Pharmaceutical Solids*; Brittain, H.G., Editor; Marcel Dekker: New York, 1999.

4. Dunuwila, D. D.; Berglund, K. A. *Trans. I. ChemE.*, **1995**.

5. Cerreta, M. K.; Berglund, K.A. *Journal of Crystal Growt,*. 1987, 84, 577-588.

6. Battey, D.E.; Slater, J.B.; Wludyka, R.S.; Owen, H.; Pallister, D.M.; Morris, M.D. *Applied Spertroscopy*, **1993**, 47, 1913.
7. Owen, H.; Battey, D.E.; Pelletier, M.J.; Slarter, J.B. *Proc. SPIE*, **1995**, 24(6), 260.

8. MATLAB Function Reference, version 5. The Math Works Inc.

9. Dongarra, J. J.; Bunch, J. R.; Moler, C. B.; Stewart, G. W. LINPACK Users' Guide, Chapter 11; Society for Industrial and Applied Mathematics: Philadelphia, 1979.

10. Dollish, F.R.; Fateley, W.G., Bentley, F.F. *Characteristic Raman Frequencies of Organic Compounds*; Wiley-Interscience: New York, 1974.

11. Silverstein, R. M.; Bassler, C. G.; Morril, T. C. Spectrometric Identification of Organic Compounds, 5th Edition; John Wiley & Sons: New York, 1991.

12. Brotherton, J. *Sex Hormone Pharmacology*; Academic Press: New York, 1976.

13. Walker, J. Private Communications.

14. Eisenberg, D.; Kauzmann, W. *The Structure and Properties of Water*; Oxford University Press: Oxford, 1969.

15. Martans, H; Naes, T. *Multivariate Calibration*; John Wiley & Sons: New York, 1989.

Chapter 4

IN SITU MONITORING OF CHANGES IN SUNFLOWER OIL FATTY ACID COMPOSITION DURING HIGH TEMPERATURE PROCESSING USING A DISPERSIVE RAMAN SPECTROMETER*

*Submitted to *Organic Process Research & Development*, April, 2004.

4-1 Abstract

The rapid determination of *trans* isomer content in edible oils is of great importance in the characterization of fats and oils in the food industry. A novel dispersive Raman spectroscopic procedure for the *in situ* monitoring of fatty acid *cis* to *trans* isomerization in edible oils is described. Raman spectral changes observed during the high temperature heating of oil were correlated with *cis* and *trans* isomer concentration determined by gas chromatography (GC). The short acquisition times, low laser power and ease of application of dispersive Raman spectroscopy using an NIR excitation source combined with the correlation derived from the GC data provided the capability of monitoring the isomerization *in situ*. The method developed here has potential applications for increased process control of edible oil hydrogenation, deodorization and quality control among other widely used processing steps. The *in situ* monitoring capability provided by dispersive Raman spectroscopy offers considerable advantages over the conventional off-line FT-Raman spectroscopy analysis.

4-2 Introduction

The accurate determination of the concentration of various types of unsaturation (especially *cis* and *trans* isomers) of fats and oils has become a subject of great importance to the food industry. This is due in part to new regulations[1] set forth by the Food and Drug Administration (FDA) regarding food and nutritional labeling. The FDA

has been urged to set forth these new regulations by consumer groups with increasing health consciousness and the mounting evidence for cardiovascular health risks from the consumption of high levels of saturated and *trans* fatty acids.

Current standard methods for determining the *cis* and *trans* content of fats and oils include gas chromatography and Fourier transform infrared spectroscopy (FT-IR) of samples captured off-line. In the past Raman spectroscopy has also been used for this purpose[2,3,4,5,6,7], although its use has been almost entirely limited to Fourier Transform (FT) Raman spectroscopy. The one exception is the seminal work in this area, in which Bailey and Horvat[2] described the use of a dispersive Raman spectrometer, but used it to analyze only pure lipid samples. Although it has been proven that FT-Raman spectroscopy is capable of providing good quality fluorescence-free spectra (due to the use of 1064 nm excitation wavelength) the current technology only allows for off-line analysis of samples.

Past publications[3,4,5,6,7] have correctly argued that dispersive Raman spectroscopy using visible light excitation sources could not be used to analyze commercial oils and fats. This was due to fluorescence (fluorescence in oils and fats is most often caused by natural antioxidants, carotenes, nutritional supplements and/or coloring ingredients) from the samples which severely degraded the quality of the spectrum. However, within the past few years there have been technological advances that now allow dispersive Raman spectrometers to use near infrared (NIR) lasers as excitation sources. The use of an NIR laser for excitation eliminates the interfering fluorescence from oil and fat samples. The present work takes advantage of the flexibility and the *in situ* analysis capability offered by dispersive Raman spectrometers and combines it with an NIR laser excitation source

in order to demonstrate the feasibility of using dispersive Raman spectroscopy to qualitatively and quantitatively monitor changes (*in situ*) of the fatty acid composition of sunflower oil during high temperature processing.

4-3 Experimental Section

Three 32 Fl oz. 100% Sunflower oil bottles (Meijer, Grand Rapids, MI) were purchased from a local retail supplier. "Fresh" 250 mL batches of oil were heated to one of the three following temperatures: 200, 250 or 300 °C and held at the particular temperature for 40 minutes. Experiments were performed in triplicate, always using fresh oil at the start. Oil was heated in a 1.19 L stainless steel beaker (Polar Ware, Sheboygan, WI) using a stirrer/hotplate model PC-420 (Corning Incorporated Life Sciences, Acton, MA). Hotplate temperature was maintained within 5 °C of the desired temperature using a CN7600 temperature controller (Omega Engineering, Inc., Stamford, CT). The oil was continuously stirred during heating using a stainless steel four-blade propeller attached to a StedFast model SL 1200 mechanical stirrer (Fisher Scientific International, Inc., Hampton, NH). All experiments began by obtaining the Raman spectrum of the oil at room temperature (20 °C), the oil was then heated at approximately 10 °C/minute until reaching the desired temperature. A schematic diagram of the experimental setup is shown on Figure 4.1. Once the 40 minute heating time period ended, the oil was immediately placed into a water-ice bath. This ensured that the oil was maintained at a constant temperature for exactly 40 minutes. Once cooled, aliquots of the oil were placed in a freezer (0 °C) for storage until they were analyzed by GC or further analyzed by Raman spectroscopy.

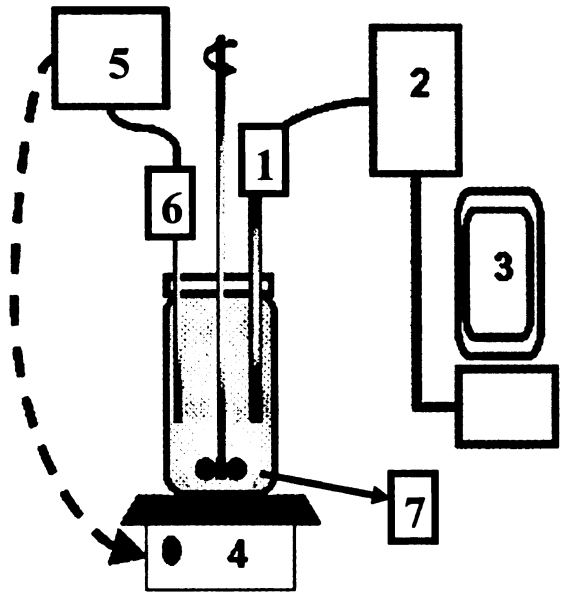

Figure 4.1. Schematic of the experimental setup. (1) Raman probe, (2) HoloLab 5000, (3) PC, (4) hot-plate, (5) temperature controller, (6) thermocouple, (7) stainless steel propeller stirrer.

4-3.1 Analytical Methods

The gas chromatography (GC) operational settings used in this work are similar to AOCS official method Ce 1c-89[8]. This method specifies GC analysis for methyl ester derivatives of fatty acids. Methyl ester derivatives were obtained by reacting sunflower oil with methanol/BF_3 as specified by AOCS official method Ce 2-66[8]. Analysis of the fatty acids composition of the oil was carried out using a Shimadzu GC-17A (Shimadzu Corp., Kyoto, Japan) GC fitted with a Supelcowax-10 (Supelco, Inc., Bellefonte, PA) capillary column (60 m × 0.32 mm i.d., 0.5 μm film thickness). The carrier gas used was helium at a flow rate of approximately 1mL/min. The sample injected was 1 μL and injection was by a split injection system (100:1 split ratio). The injector temperature was 210 °C, while the flame ionization detector was maintained at 230 °C. The column oven was temperature programmed from 150 to 200 °C at 1.3 °C/min and held at that temperature for 30 minutes. Identification of peaks was by comparison of relative retention times with those of authentic standards.

Fluorescence spectra were acquired using a Spex Fluorolog-2 Spectrofluorometer (Spex Industries, Inc., Edison, NJ). Sunflower oil was tested using 632.8 and 785 nm excitation wavelengths. The collection ranges were 635 to 800 nm for 632.8 nm excitation and 790 to 900 nm for 785 nm excitation wavelength. Acquisition time was 1 seconds per collection wavelength.

Raman spectra were collected using a HoloLab Series 5000 instrument (Kaiser Optical Systems, Inc., Ann Arbor, MI). During heating Raman spectra were acquired in one minute intervals. Once the desired temperature was reached, Raman spectra were acquired using two minute intervals. All spectra were obtained using two acquisitions

with two second exposure leading to a four second total acquisition time per spectrum. Details of the HoloLab 5000 have been described previously[9,10]. Briefly, a 100 mW external cavity stabilized diode laser at 785 nm is used for sample illumination. A CCD camera, a spectrograph, and a fiber optic probe complete the HoloLab 5000 system. Remote sampling was accomplished by employing a fiber optic probe attached to an immersion optic to focus the incident beam into the solutions. The positioning of the immersion optic was maintained constant through out all the experiments. This ensured that any effects the immersion optic may have had on the experiments remained constant throughout.

4-4 Results and Discussion

As discussed in the introduction section, many previous FT-Raman studies of edible oils have argued that only FT-Raman and not dispersive Raman spectroscopy can be used to analyze edible oils. The reason given was that dispersive Raman spectrometers were limited to using excitation lasers in the visible wavelength range. Using visible wavelength range excitation sources caused fluorescence from impurities or additives in the oil. The fluorescence would overwhelm the Raman scattering signal and therefore obtaining a spectrum with acceptable signal-to-noise ratio was impossible. This argument was correct, until approximately five years ago when a dispersive Raman spectrometer using NIR excitation laser became available. However, some FT-Raman studies[5,7] analyzing edible oils continue to use the outdated argument. It can be demonstrated that in order to avoid the fluorescence interference when analyzing edible oils it is not necessary to use an excitation source as far into the IR region as FT-Raman does using

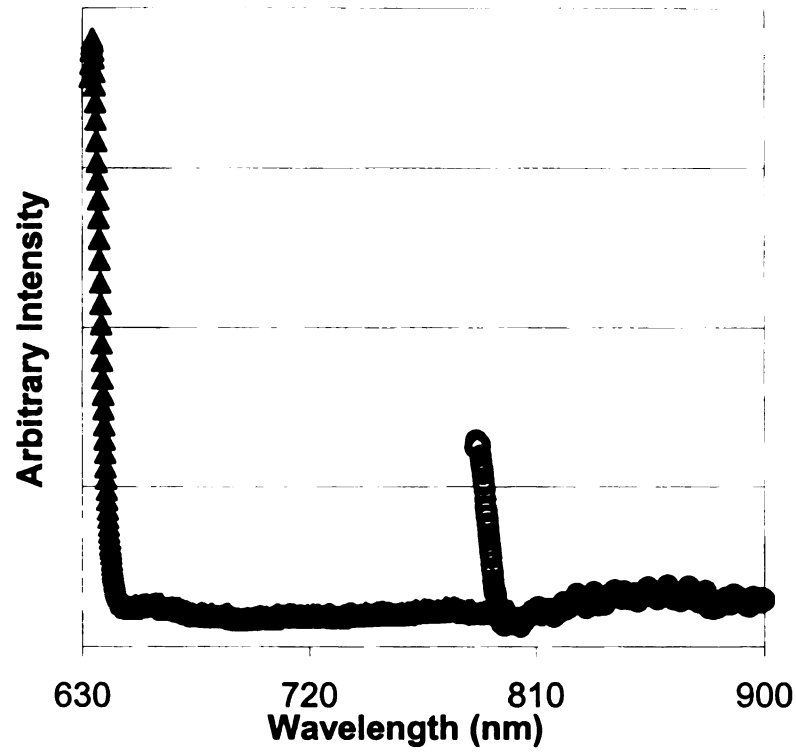

Figure 4.2. Fluorescence emission spectra of sunflower oil obtained for oil at room temperature. (Δ) 632.8 nm excitation, (O) 785 nm excitation.

the 1064 nm wavelength. Figure 4.2 shows the fluorescence emission spectra of sunflower oil using excitation at 632.8 and 785 nm. It is evident from these spectra that using 785 nm excitation sources reduce the fluorescence intensity by approximately half. These results indicate that it may be possible to use a dispersive Raman spectrometer to analyze edible oils. Using a lower wavelength excitation source provides one main advantage, improved sensitivity. Because the efficiency of Raman scattering is inversely proportional to wavelength to the fourth power, a lower wavelength excitation source allows the use of lower laser power and shorter acquisition times. The shorter acquisition times allow for *in situ* monitoring of processes.

Figure 4.3 displays the Raman spectrum of sunflower oil at room temperature. This figure demonstrates that by using an NIR laser as an excitation source it is possible to obtain high signal to noise ratio, fluorescence free Raman spectra of edible oils using dispersive Raman spectrometers. Table 4.1 displays the assignments of the major Raman bands of the sunflower oil spectrum. There are numerous references in the literature that have utilized various ratios of the peaks presented in Table 4.1 in order to quantitatively analyze the fatty acid composition of edible oils. As mentioned in the introduction section all of these references have been limited to analyzing samples off-line. This is due to all but one reference using FT-Raman spectroscopy for the analyses. By using a dispersive Raman instrument it was possible to implement similar peak area ratio methodologies used by the previous studies in order to monitor (*in situ*) changes in the fatty acid composition of edible oils during high temperature processing. As described in the experimental section batches of fresh sunflower oil were heated to 200, 250 or 300 ^{o}C

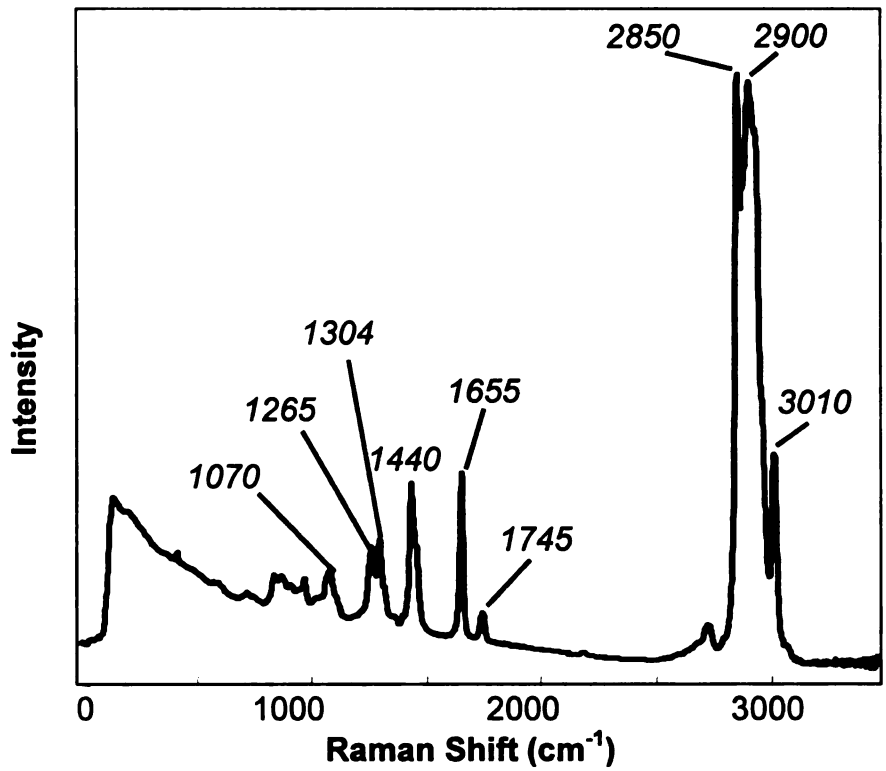

Figure 4.3. Raman spectrum of sunflower oil acquired at room temperature using a dispersive Raman spectrometer.

Raman Shift (cm^{-1})	Molecule	Group	Vibration
3010	RCH=RCH	=C-H	Asymmetric stretching
2900	-CH3	C-H	Symmetric stretching
2850	-CH2	C-H	Symmetric stretching
1745	RC=OOR	C=O	Stretching
1665	***trans* only** RCH=CHR	C=C	Stretching
1655	***cis* only** RCH=CHR	C=C	Stretching
1440	-CH2	C-H	Deformation
1300	-CH2	C-H	Deformation
1265	***cis* only** RCH=CHR	=C-H	Deformation
1070	-(CH2)n-	C-C	Stretching

Table 4.1. Assignment of the major Raman scattered bands of sunflower oil.

and held at the corresponding temperature for 40 minutes. GC analyses of unheated samples of sunflower oil revealed the following fatty acid profile: 6.01 ± 0.02 % palmitic acid, 4.15 ± 0.33 % stearic acid, 24.53 ± 3.04 % *cis* oleic acid, 0.59 ± 0.03 % *trans* oleic acid, 64.41 ± 2.24 % *cis,cis* linoleic acid, 0.26 ± 0.03 % *cis,trans* linoleic acid. These values are in good agreement with previously reported[11] sunflower oil fatty acid concentrations. It should be noted that because it was necessary to purchase three bottles of oil in order to perform the experiments, the standard deviation values calculated for all the data presented in this work are influenced by the differences in the fatty acid composition of natural oils. Table 4.2 lists the results obtained from GC analysis for the total %*cis* and total %*trans* of the samples heated at the three temperatures plus a control sample which was not heated. The calculation of %*cis* and %*trans* is not straight forward, since sunflower oil contains high amounts of linoleic acid. Linoleic acid with its two double bonds can be present in the samples as one of four isomers: *cis,cis* / *cis,trans* / *trans,cis* / *trans,trans*. The recent FDA regulation[1] that requires *trans* fat concentration to be listed in the nutritional label of foods provides the solution. If the double bonds are not conjugated, *cis,trans* and *trans,cis* isomers should be considered *trans*.

An examination of Table 4.2 reveals that there are significant changes in the total %*cis* and the total %*trans* concentration (determined by GC) of fatty acids as a function of temperature. The total %*cis* concentration decreases by 8.5% while the total %*trans* concentration increases by 7.5%. A more in-depth analysis of the GC data reveals that there is no change in the concentrations of *cis* or *trans* oleic acid and only linoleic acid is undergoing isomerization. These results are in good agreement with previous findings[12]

Temperature (°C)	Total *cis* (%)	Total *trans* (%)
25	88.69 ± 3.78	0.94 ± 0.11
200	87.18 ± 5.66	1.68 ± 0.64
250	87.67 ± 4.47	1.22 ± 0.17
300	80.12 ± 3.18	8.48 ± 1.27

Table 4.2. Fatty acid composition of sunflower oil as a function of temperature determined

which indicate that polyunsaturated fatty acids are susceptible to heat induced isomerization.

Table 4.1 was utilized to find peak areas and peak area ratio that could be correlated to the isomerization taking place. Previous studies[2,3,7] have focused on the 1655 cm^{-1} peak as an indicator of *cis* isomer concentration. Our attempts to correlate this peak area with the total %*cis* concentration determined by GC resulted in a poor linear model. The poor linearity can be explained by the fact that during isomerization the peak area of the 1665 cm^{-1} peak increases. This peak has been assigned to the *trans* C=C stretching, as the isomerization progresses and the 1665 cm^{-1} peak area increases it overlaps with the 1655 cm^{-1} peak and thus interferes with the calculation of the 1655 cm^{-1} peak area. Because of this interference it was necessary to find another peak that could be used in order to monitor the concentration of *cis* isomer. The 1265 cm^{-1} peak, which has been assigned to in-plane =C-H deformation in an unconjugated *cis* double bond[3], was the other available peak. Although the 1265 cm^{-1} peak also suffers from some overlap with another peak (the 1300 cm^{-1} peak assigned to in-plane CH_2 twisting) the overlap is not as severe, and the correlation between this peak area and the total %*cis* concentration provides a reasonable linear correlation. In order to improve the reliability of the correlation between the spectroscopic data and the GC data a peak area ratio was used instead of the absolute peak area of the 1265 cm^{-1} peak.

The 1745 cm^{-1} peak was chosen to ratio with the 1265 cm^{-1} peak, this peak ratio has successfully been used previously[4] to monitor the *cis* and *trans* isomer concentration in off-line oil samples. The 1745 cm^{-1} peak has been assigned to the carbonyl stretching of fatty acids. The carbonyl moiety should be unaffected by the isomerization of the C=C

bond, which indicates that the 1745 cm^{-1} peak should also be unaffected. Although the discussion above regarding the use of the 1745 cm^{-1} peak is valid, it fails to take into account the many degradation products that are known to form during the hearting of oil at high temperatures[13]. More specifically, previous work[14] has demonstrated that sunflower oil heated at 300 °C for 40 minutes degrades the oil into a variety of oxidation products such as ketones and aldehydes (lower temperatures produced insignificant changes). In that work, an increase in concentration of those carbonyl containing compounds due to the heating of sunflower oil was demonstrated to increase the peak area and the peak width of the 1745 cm^{-1} peak during off-line studies using FT-IR for analysis. However, even using FT-IR, which is known to be far more sensitive to carbonyl vibrations than Raman spectroscopy, the changes to the spectrum of sunflower oil due to the formation of the oxidation degradation products was quite small. Figure 4.4 shows the average (of three experiments) peak area of the 1745 cm^{-1} peak plotted versus time for sunflower oil being heated at 300 °C for 40 minutes. It can be seen that there is no meaningful change in the peak area. Without more in-depth data analysis (such as derivative calculations or multivariate analysis) the use of baseline integration calculations of unprocessed Raman spectra is incapable of detecting the changes to the 1745 cm^{-1} peak that should accompany the increase in carbonyl containing compounds. Because the 1745 cm^{-1} peak area remains constant through the heating process at a particular temperature, it was a good candidate to "normalize" the 1265 cm^{-1} peak area. The plot of the 1265/1745 peak area ratio versus the total *%cis* determined by GC for sunflower oil unheated and after heating to the three test temperatures is shown in Figure 4.5. This plot gives rise to a linear fit of with a reasonable correlation coefficient of 0.95.

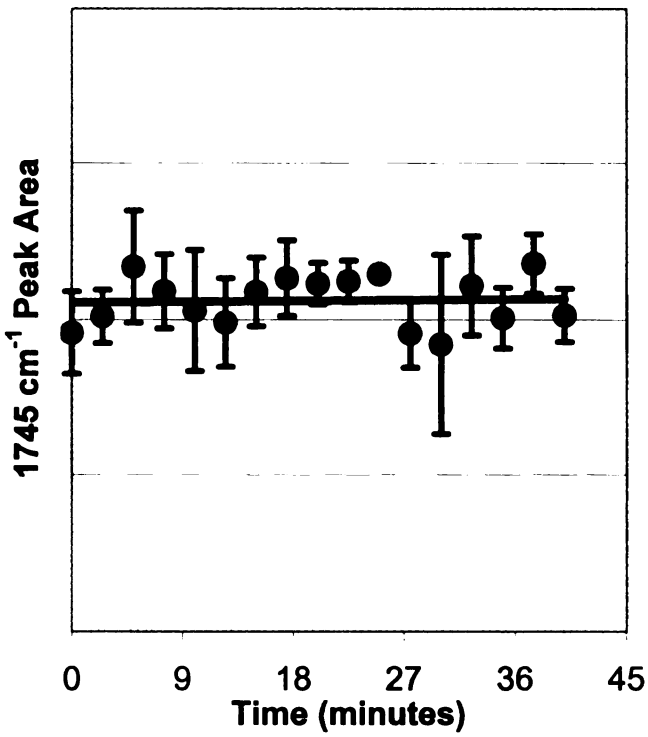

Figure 4.4. Average peak area and standard deviation for 1745 cm^{-1} peak plotted against time for oil heated at 300 °C for 40 minutes.

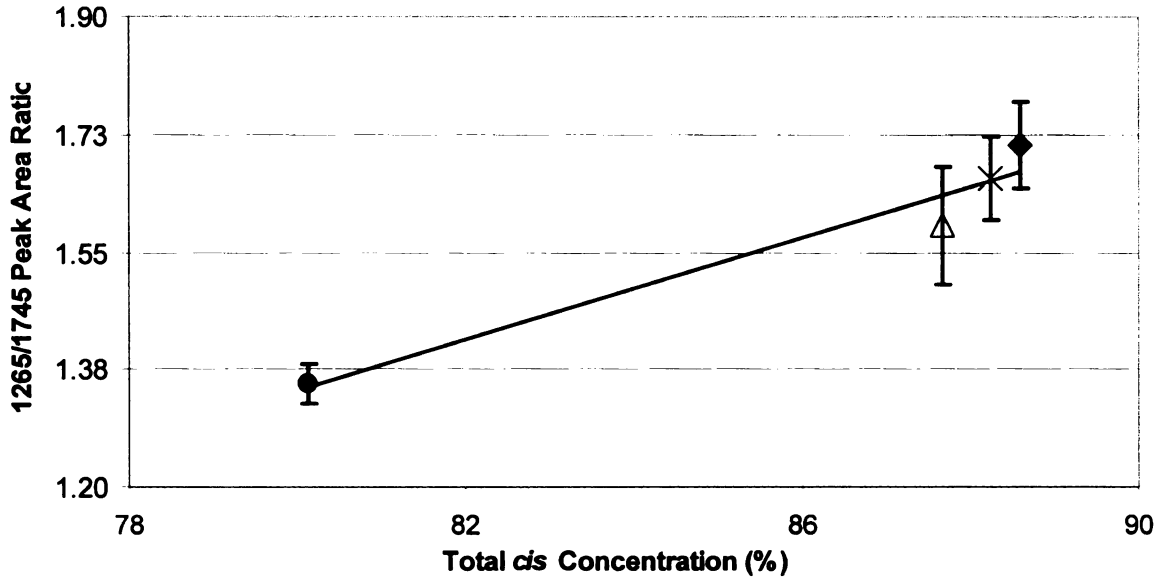

Figure 4.5. Peak area ratio 1265/1745 plotted against the total %*cis* concentration as determined by GC. Linear fit displays reasonable correlation coefficient of 0.95. (◆) unheated sample, (×) 200 °C, (Δ)250 °C, (●) 300 °C.

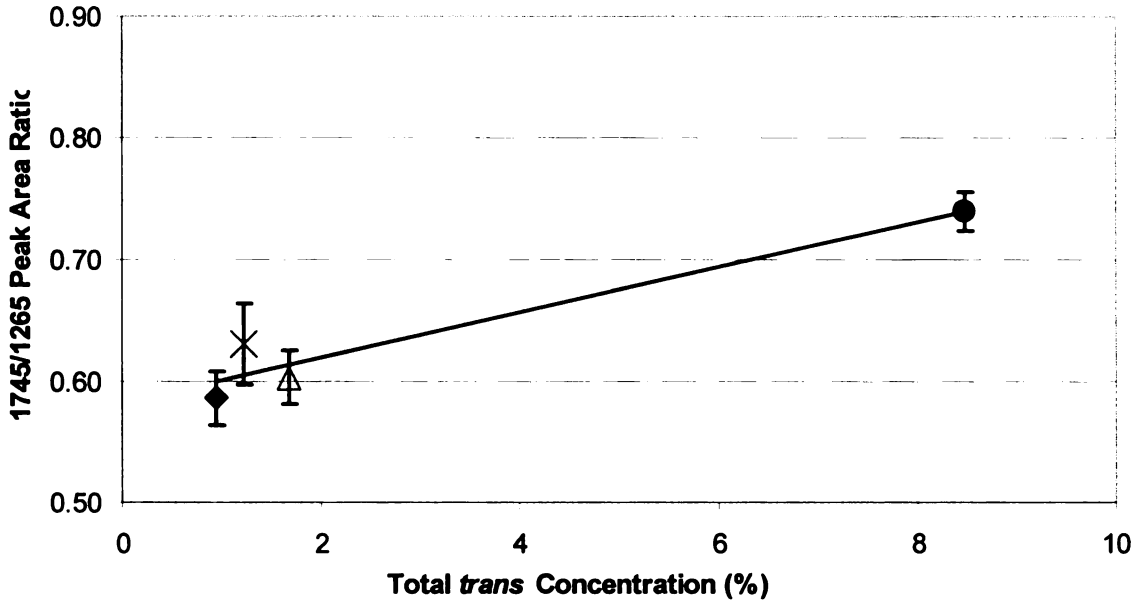

Figure 4.6. Peak area ratio 1745/1265 plotted against the total %*trans* concentration as determined by GC. Linear fit displays reasonable correlation coefficient of 0.93. (◆) unheated sample, (×) 200 °C, (Δ)250 °C, (●) 300 °C.

If the peak area ratio of 1265/1745 can be correlated to the concentration of *cis* isomers, it should be possible to correlate the inverse of the peak area ratio to the *trans* isomer concentration. The plot of 1745/1265 peak area ratio versus total *%trans* is presented as Figure 4.6. The plot on Figure 4.6 provides a linear fit with a reasonable correlation coefficient of 0.93. For clarity, it should be stated that the spectral data used for Figures 4.5 and 4.6 were obtained at room temperature. That is, the samples were heated and cooled as described in the experimental section and then Raman spectra were acquired. Figures 4.5 and 4.6 demonstrate that at a constant temperature, a linear correlation can be made between these peak area ratios and the GC data which can be used to monitor changes in the total *%cis* and total *%trans* concentrations of edible oils. Figure 4.7 displays the 1745/1265 peak area ratio versus time for sunflower oil during heating at the three test temperatures. From Figure 4.7 it can be seen that during the 40 minutes for which oil was held at 200 °C the 1745/1265 peak area ratio did not change from its initial value. The ratio can be seen to increase slightly for the oil held at 250 °C. Finally, for the oil held at 300 °C the ratio undergoes a relatively large increase from its initial value. Utilizing the linear correlation developed in Figure 4.6 it is possible to state that the changes in the peak area ratio seen in Figure 4.7 are directly related to the change in concentration of the *trans* isomer in the oil samples. Figure 4.7 demonstrates that the rate of thermally induced *cis* to *trans* isomerization increases with increasing temperature under the circumstances examined in this work. The increased rate therefore leads to a higher total *%trans* concentration in oils heated at 300 °C as compared to oils heated at 200 or 250 °C for the same period of time. The results from Figure 4.7 are in good agreement with the GC data presented in Table 4.2. Only at 300 °C is there a marked

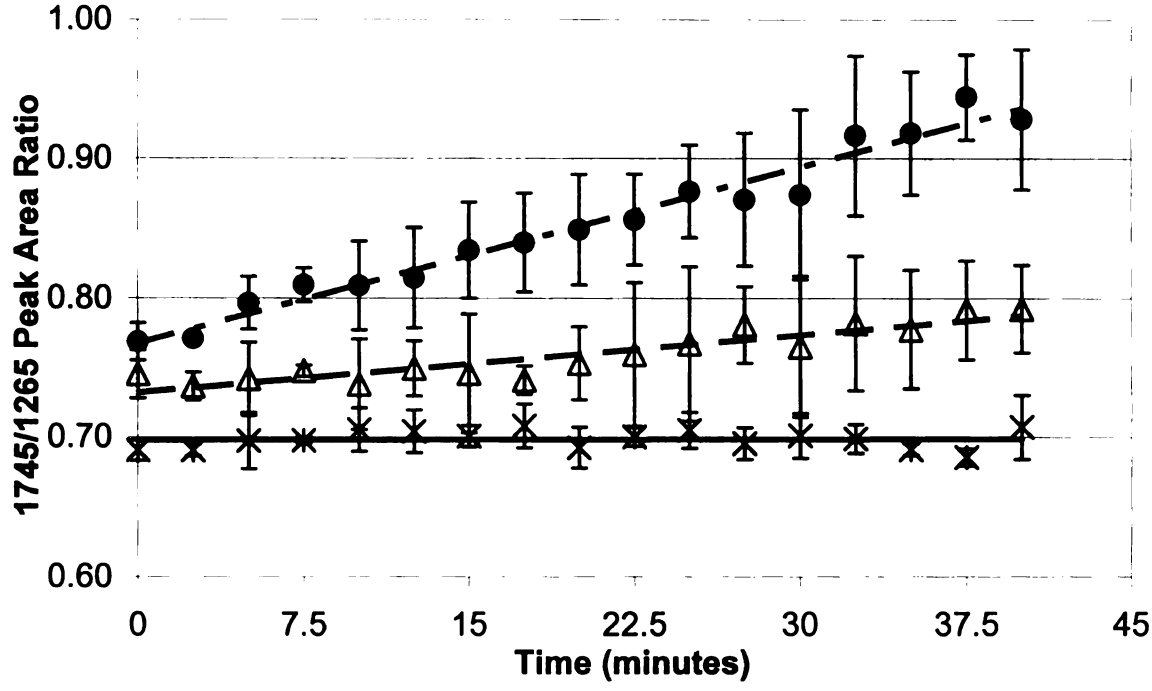

Figure 4.7. Peak area ratio 1745/1265 plotted against time for the three test temperatures. (×) 200 °C, (Δ)250 °C, (●) 300 °C.

increased in the concentration of *trans* isomers. The results displayed in Figure 4.7 also agree well with previous work[15] which demonstrated that the thermally induced *cis* to *trans* isomerization of linoleic acid was strongly dependent on temperature.

It would now seem possible that the linear correlation obtained from Figure 4.6 could be used to roughly quantify the data from Figure 4.7 by converting the 1745/1265 peak area ratio to *trans* isomer concentration. This quantification would result in *trans* isomer concentrations much higher than the actual values. The error can be (apart from the fact that the calibration curve being used would be comprised of only four points) explained by the dependence of the ratio of anti-Stokes to Stokes Raman scattering on Boltzmann's distribution. At lower temperatures (up to approximately 225 °C) the anti-Stokes to Stokes peak area intensity for the 1265 cm^{-1} peak is smaller than the same ratio for the 1745 cm^{-1} peak. While at higher temperature (approximately 250 °C and above) the opposite is true. This inversion in peak intensities means that the 1745/1265 peak area ratio will not be constant when compared between different temperatures. Because of the dependence of the peak areas on temperature, it would be necessary to create a calibration curve for every temperature tested.

In addition to monitoring *cis* to *trans* isomerization, it should also be possible to monitor degradation of fatty acids and the resulting degradation products. Initially, the monitoring of fatty acid degradation appears to be a straightforward task, analyze the *in situ* monitoring spectral data for the appearance of new peaks and the decrease in area of existing peaks. However, as alluded to earlier in this section, the heating of oils at high temperatures (whether food is present in the oil or not) produces a multitude of degradation products[13]. Some of the degradation products that have been detected are:

monoglycerols, oxidized triacylglycerols, tryacylglycerol polymers (also dimers and trimers), cyclic fatty acids, free fatty acids, ketones, aldehydes, alcohols and esters. With the appearance of such a large number of degradation products it would be difficult to single out the effect of one particular molecule to the changes observable in the Raman spectral data. Another difficulty with the monitoring of degradation products will be the concentrations levels at which they are formed. Depending on the experimental conditions many of the degradation products may be formed at concentrations below those which Raman spectroscopy can detect. For these reasons great care should be taken with the interpretation of Raman spectral data obtained from the in situ monitoring of high temperature heating of edible oils.

4-5 Conclusions

The results of this study demonstrate the possibility and advantages of using dispersive Raman spectroscopy with an NIR excitation source for analysis of edible oils on or off-line. It can no longer be argued that FT-Raman spectroscopy is superior to dispersive Raman spectroscopy for the analysis of edible oils. Using GC concentration measurements in combination with Raman spectroscopy measurements it was possible to create correlations between changes in the Raman spectra of oils and *cis* and *trans* isomer concentrations. The methodology developed in this work for *in situ* monitoring of *cis* to *trans* isomerization of edible oils has a number of immediate potential applications for the oil production industry. It also provides significant advantages with regard to sample handling/storage, sample analysis time and process monitoring/process control capabilities over conventional techniques (GC, off-line FT-Raman, off-line FT-IR) for the analysis of natural oils hydrogenation process. Other clear applications would be for

monitoring the deodorization of natural oils and also for on-line quality analysis of oils during cooking. These advantages should translate to improvements in the process productivity, production efficiency and superior quality control capabilities.

4-6 Acknowledgments

Dr. Dale LeCaptain of Central Michigan University provided one of the Raman spectrometers. Kaiser Optical Systems, Inc. provided a second Raman spectrometers and HoloReact software. Their contributions are appreciated. Partial support of J. A. F. was received from GAANN and Alfred P. Sloan Foundation fellowships.

4-7 References

1. FDA/DHHS, 68 Federal Register, 41,434 (July 11, 2003). *Food Labeling: Trans Fatty Acids in Nutrition Labeling, Nutrient Content Claims, and Health Claims* (Final Ruling). (Internet address: http:// www.cfsan.fda.gov/~lrd/fr03711a.html)

2. Bailey, G.F; Horvat, R.J. *J. Am. Oil Chem. Soc.* **1972**, 49 (8), 494-498.

3. Sadeghi-Jorabchi, H.; Hendra, P.J.; Wilson, R.H.; Belton, P.S. *J. Am. Oil Chem. Soc.* **1990**, 67 (8), 483-486.

4. Sadeghi-Jorabchi, H.; Wilson, R.H.; Belton, P.S.; Edwards-Webb, J.D.; Coxon, D.T. *Spectrochimica Acta.* **1991**, 47A (9/10), 1449-1458.

5. Baeten, V.; Hourant, P.; Morales, M.T.; Aparacio, R. *J. Agric. Food Chem.* **1998**, 46, 2638-2646.

6. Johnson, G.L.; Machado, R.M.; Freidl, K.G.; Achenbach, M.L.; Clark, P.J.; Reidy, S.K. *Organic Process Research & Development.* **2002**, 6 (5), 637-644.

7. Weng, Y.M.; Weng, R.H.; Tzeng, C.Y.; Chen, W. *Applied Spectroscopy.* **2003**, 57 (4), 413-418.

8. *Official Methods and Recommended Practices of the AOCS,* 5th ed.; Firestone, D., Ed.; American Oil Chemist's Society: Champaign, Illinois, 1998.

9. Battey, D.E.; Slater, J.B.; Wludyka, R.S.; Owen, H.; Pallister, D.M.; Morris, M.D. *Applied Spectroscopy.* **1993**, 47, 1913.

10. Owen, H.; Battey, D.E.; Pelletier, M.J.; Slater, J.B. *Proc. SPIE.* **1995**, 24 (6), 260.

11. Romero, A.; Sanchez-Muniz, F.J.; Cuesta, C. *J. Sci. Food Agric.* **2000**, 80, 2135-2141.

12. Jorge, N.; Guaraldo Goncalves, L.Ap.; Dobarganes, M.C. *Grasas y Aceites.* **1997**, 48 (1), 17-24.

13. *Food Lipids, Chemistry, Nutrition, and Biotechnology*, Akoh, C.C., Min, D.B., Ed.; Marcel Dekker: New York, NY, 1997.

14. Moya Moreno, M.C.M.; Mendoza Olivares, D.; Amezquita Lopez, F.J.; Peris Martinez, V.; Bosch Reig, F. *Journal of Molecular Structure.* **1999**, 482-483, 557-561.

15. Leon-Camacho, M.; Ruiz-Mendez, M.V.; Graciani-Constante, M.; Graciani-Constante, E. *Eur. J. Lipid Sci. Technol.* **2001**, 103, 85-92.

Chapter 5

CONTINUING INVESTIGATION: *IN SITU* MONITORING OF OIL OXIDATION DEGRADATION PRODUCTS USING A DISPERSIVE RAMAN SPECTROMETER

5-1 Introduction

The oxidation of edible oils containing a large amount of polyunsaturated fatty acids (PUFAs) is a major concern for the food industry because it is directly related to economic, flavor, and storage problems. Although relatively well understood in general terms, lipid oxidation is a quite complex and variable process which depends on oil type and conditions of oxidation[1,2]. A wide range of end products are associated with the oxidative deterioration of oils at ambient and elevated temperatures[1,3], the most important being hydroperoxides, alcohols and aldehydes. Hydrocarbons, free fatty acids (FFAs), esters, ketones, lactones, furans, triacylglycerol polymers and other minor products may also be produced. In addition, there is significant *cis* to *trans* isomerization and conjugation of double bonds in the hydroperoxides formed as an oil oxidizes. The rate of oxidation and the distribution of accumulated products depend strongly on the oil source, fatty acid composition, degree of unsaturation, presence of metal ions and antioxidants, time and thermal stress. This wide array of variables affecting the oxidation process makes it essential to have a reliable means of assessing the oxidative status and oxidative stability of edible oils.

Standard methods for determining oxidation degradation product content of fats and oils include titrations (which are largely empirical in nature), capillary GC-MS and size exclusion HPLC of samples captured off-line[1,4]. Within the last 5 to 10 years there has been an increased interest in utilizing Fourier Transform infrared spectroscopy (FT-IR) to

analyze oxidation degradation products[5,6,7,8]. Surprisingly there has been little or no work done on investigating the possibility of using Raman spectroscopy. There are two likely explanations for the lack of interest in Raman spectroscopy. First, up until our recent study[9] the analysis of fats and oils with Raman spectroscopy was confined to the use of FT-Raman spectroscopy[10,11,12,13]. The current FT-Raman technology does not provide *in situ* analysis capabilities, which makes the technique inadequate for monitoring such a dynamic process as oil oxidation. Second, is the fact that Raman spectroscopy is known to be relatively insensitive (when compared to FT-IR) to functional groups often correlated with oxidation products such as carbonyls, aldehydes and alcohols. Therefore, it is likely that past researchers have assumed that Raman spectroscopy would be unable to detect changes in the oil due to oxidation degradation. We propose that even though Raman spectroscopy may be insensitive to the specific functional groups related to oxidation degradation, the degradation products will have other functional groups which Raman spectroscopy is particularly sensitive to such as peroxides and conjugated double bonds[14].

The present work attempts to take advantage of the flexibility and the *in situ* analysis capability offered by dispersive Raman spectrometers in order to demonstrate the feasibility of using Raman spectroscopy to qualitatively monitor changes (*in situ*) in the composition of sunflower oil during oxidative degradation.

5-1.1 Lipid Oxidation

Long chain fatty acids are abundant in nature, most commonly in combination with glycerol as either as tryacylglycerides or as the amphiphilic membrane phospholipids. From most sources, tryacylglycerides will be found to comprise a mixture of compounds

with differing proportions of saturated, mono-unsaturated, and poly-unsaturated fatty acid residues. Particularly common are fatty acid residues with eighteen carbon atoms, consequently we will focus our attention on derivatives of linoleic and linolenic acids (structures shown on Figure 5.1). In the context of lipid oxidation and free radical formation it is important to mention that both linoleic and linolenic acid incorporate "skipped" diene units in their molecular structure. It is known that allylic C-H bonds are relatively weak[2], more specifically the C-H bonds of the central methylene group in skipped dienes (like linoleic and linolenic acdis) are "doubly" allylic and are especially weak (ca. 75 kcal / mol). These hydrogen atoms are therefore unusually susceptible to radical attack leading to the formation of resonance stabilized dienyl radicals (see Figure 5.2 A).

Lipid oxidation is believed to be due to a combination of triplet and singlet oxygen reactions with fatty acids. Triplet oxygen lipid oxidation has been extensively studied to improve the oxidative stability of foods[1]. Triplet oxygen, a di-radical compound, does not react with the singlet state linoleic acid instead linoleic acid must be in a free radical form to react as shown in Figure 5.2A. This reaction is known to produce only conjugated *cis* and *trans* hydroperoxides. Although triplet oxygen oxidation has been widely studied it does not fully explain the initiation step of lipid oxidation. For this reason researchers[1] have suggested that singlet oxygen is involved in the initiation of lipid oxidation. Singlet oxygen is an electrophilic, non-radical compound which reacts with electron-rich, non-radical compounds (like linoleic acid) as shown on Figure 5.2B. Figure 5.2B demonstrates that the reaction between singlet oxygen and linoleic acid leads to the formation of conjugated and non-conjugated *cis* and *trans* hydroperoxides.

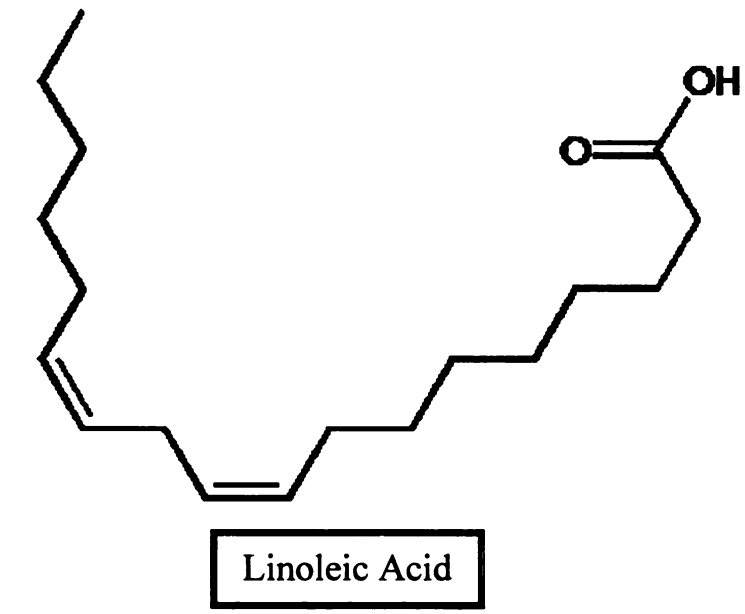

Linoleic Acid

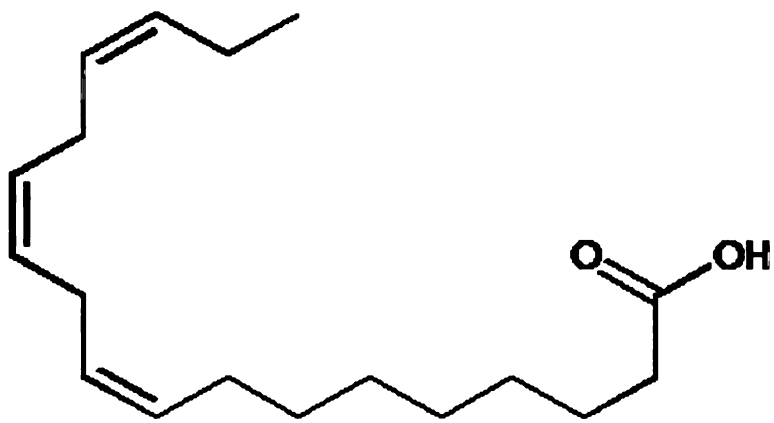

Linolenic Acid

Figure 5.1. Molecular structure of linoleic and linolenic acids.

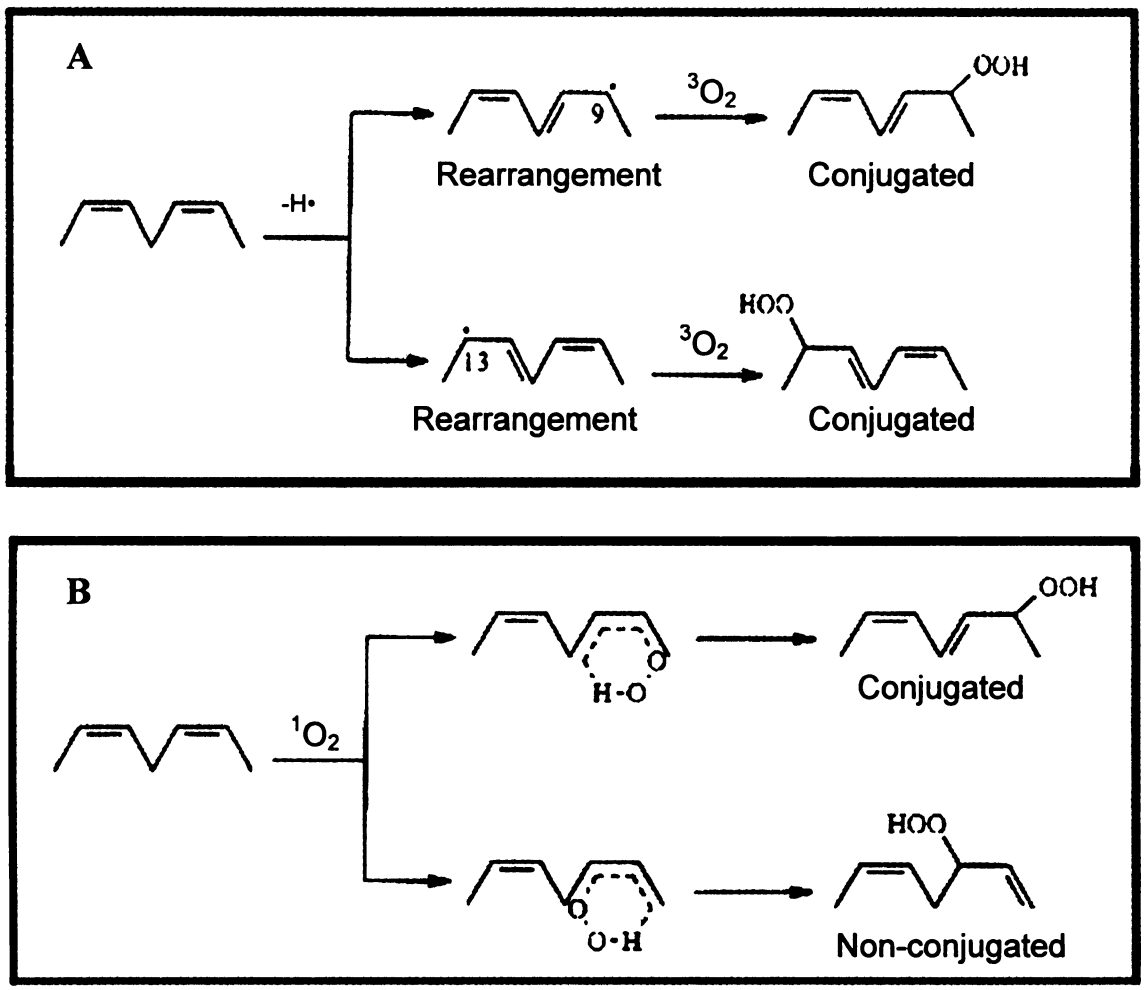

Figure 5.2. A) Reaction mechanism of triplet oxygen with linolenic acid. B) reaction mechanism of singlet oxygen with linoleic acid[1].

Because singlet oxygen can react with the non-radical compounds, its reaction rate with linoleic acid is known to be at least 1000 times higher than that of triplet oxygen[1]. Despite the large difference in reaction rates, free radical triplet oxygen oxidation is considered the primary mechanism for the formation of volatile flavor components in edible oils. This is due to triplet oxygen being more abundant than singlet oxygen and also to the relative ease with which free radicals are formed in linoleic and linolenic acid (due to the doubly allylic central group mentioned above) which allow the triplet oxygen oxidation reaction to occur.

5-1.2 Hydroperoxide Decomposition

A general decomposition pathway of hydroperoxide to produce volatile compounds is shown in Figure 5.3. The most likely first step in the decomposition pathway is the cleavage between the oxygen and oxygen of the R-O-O-H, that is, R-O-O-H → RO* + *O-H. The unsaturated alkoxy radical can be cleaved by β-scission in two mechanisms of cleavage (A and B of Figure 5.3). It is clear that the decomposition pathway will lead to a large number of degradation products. An in-depth discussion of all possible degradation products is beyond the scope of this work. For a more comprehensive analysis readers are directed towards the extensive body of literature available on the subject[1,3].

5-2 Experimental Section

Two 32 Fl oz. 100% Sunflower oil bottles (Meijer, Grand Rapids, MI) were purchased from a local retail supplier. "Fresh" 150 mL batches of oil were heated to

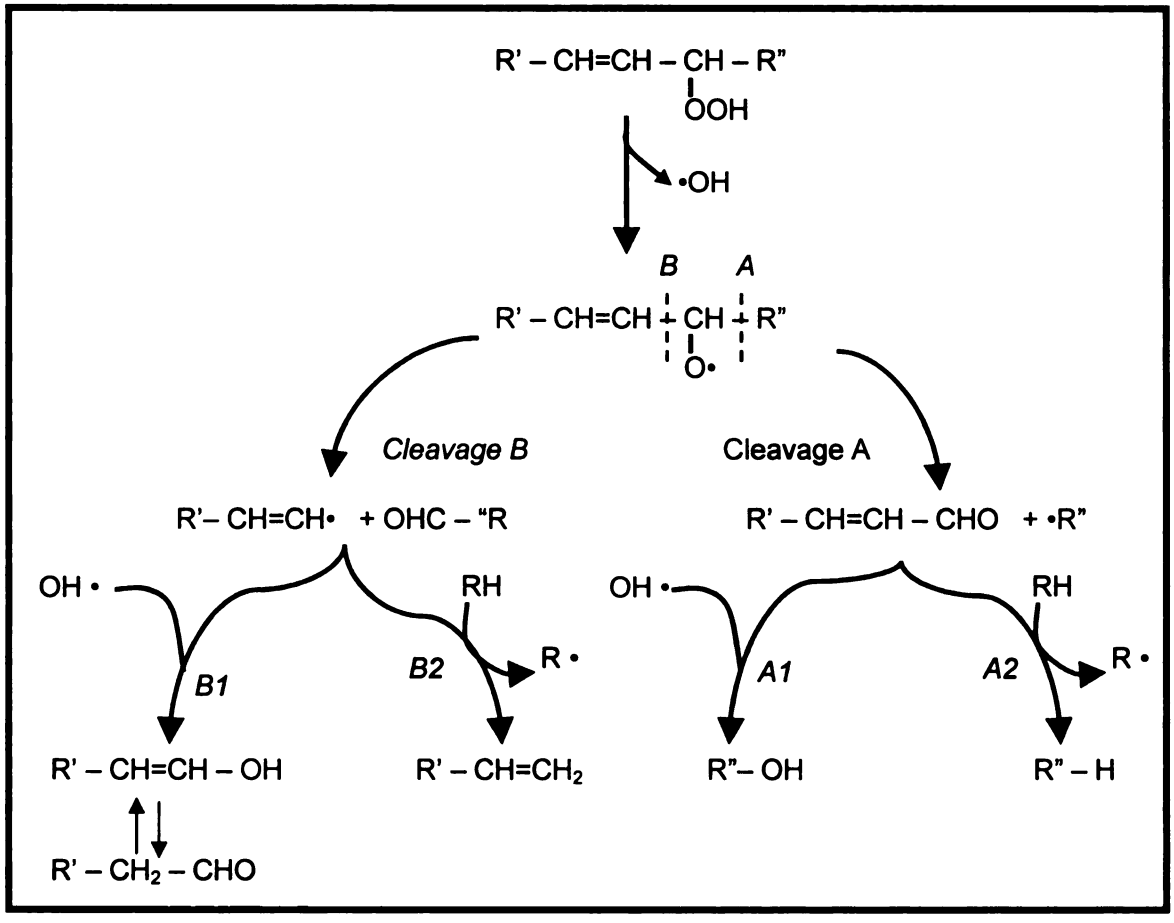

Figure 5.3. General decomposition pathway of hydroperoxide to produce volatile compounds[1].

either 130 or 200 °C and held at that particular temperature for 180 minutes. Each experiment was performed twice at each temperature. For the first experiment 0.5 g of tert-Butylhydroquinone (TBHQ) was added to the oil once the desired temperature had been reached. The second experiment was performed with neat oil. All experiments were performed using fresh oil at the start. Oil was heated in a 1.19 L stainless steel beaker (Polar Ware, Sheboygan, WI) using a stirrer/hotplate model PC-420 (Corning Incorporated Life Sciences, Acton, MA). Hotplate temperature was maintained within 3 °C of the desired temperature using a CN7600 temperature controller (Omega Engineering, Inc., Stamford, CT). The oil was continuously stirred during heating using a stainless steel four-blade propeller attached to a StedFast model SL 1200 mechanical stirrer (Fisher Scientific International, Inc., Hampton, NH). In order to facilitate oxidation dry air (AGA Specialty Gas, Cleveland, OH) was bubbled continuously through the oil at approximately 15 mL/min. The oil was heated at approximately 10 °C/minute until reaching the desired temperature. A schematic diagram of the experimental setup is shown on Figure 5.4. Once the 180 minute heating time period ended, the oil was immediately placed into a water-ice bath. This ensured that the oil was maintained at a constant temperature for exactly180 minutes.

5-2.1 Analytical Methods

Raman spectra were collected using a HoloLab Series 5000 instrument (Kaiser Optical Systems, Inc., Ann Arbor, MI). Once the desired temperature was reached, Raman spectra were acquired using five minute intervals. All spectra were obtained using two acquisitions with two second exposure leading to a four second total acquisition time per

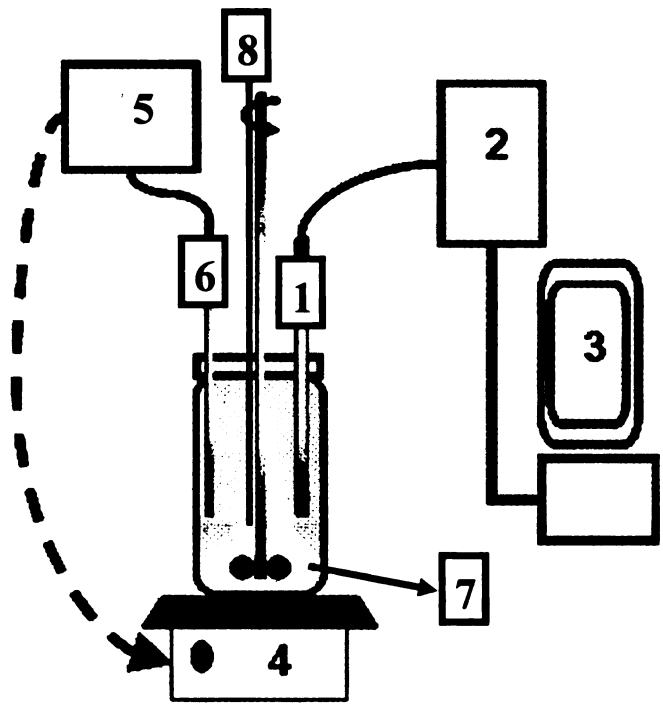

Figure 5.4. Schematic of the experimental setup. (1) Raman probe, (2) HoloLab 5000, (3) PC, (4) hot-plate, (5) temperature controller, (6) thermocouple, (7) stainless steel propeller stirrer, (8) dry air input.

spectrum. Details of the HoloLab 5000 have been described previously[15,16]. Briefly, a 100 mW external cavity stabilized diode laser at 785 nm is used for sample illumination. A CCD camera, a spectrograph, and a fiber optic probe complete the HoloLab 5000 system. Remote sampling was accomplished by employing a fiber optic probe attached to an immersion optic to focus the incident beam into the solutions. The positioning of the immersion optic was maintained constant through out all the experiments. This ensured that any effects the immersion optic may have had on the experiments remained constant throughout.

5-3 Results and Discussion

As described in the experimental section two different experiments were used to investigate the possibility of using Raman spectroscopy to monitor the oxidation of edible oils. The first experiment involved heating the oil to a specified temperature, then adding the commercial (Food & Drug Administration [FDA] approved) antioxidant tert-butylhydroquinone (TBHQ) and finally holding the oil at the specified temperature for 180 minutes. The second experiment is identical to the first, except that no TBHQ is added. It should be mentioned that for this work TBHQ was added at a higher weight percent (based on the "fat" weight of the product) than is allowed by the FDA (current work used 0.4 wt%, FDA allows a maximum of 0.02 wt%)[17].

With this simple experimental design it was possible to analyze the Raman spectra collected for the two experiments and determine if Raman spectroscopy was capable of detecting any changes in the oil due to oxidation. Spectral subtraction was used in order to elucidate any changes to the spectrum of sunflower oil that occurred during the experiments. Unless otherwise specified the spectral subtraction involved subtracting the

first spectrum acquired once the oil had reached the desired temperature (spectrum at time = 0) from the spectrum of interest. Figure 5.5 shows the results of spectral subtraction for the experiment conducted at 130 °C with TBHQ added. In Figure 5.5, A is the spectrum obtained after 5 minutes and B is the spectrum obtained after 180 minutes of holding at 130 °C (spectra have been offset for clarity). Except for the change in baseline linearity, spectra A and B do not display any significant differences. The change in baseline linearity will be discussed below.

Figure 5.6 shows the results of spectral subtraction for the experiment conducted at 130 °C without TBHQ. Spectrum A was obtained after 5 minutes and spectrum B was obtained after 180 minutes of holding at 130 °C (spectra have been offset for clarity). In this case it is clear that there are substantial differences between the two spectra. One of the major differences between the spectra shown in Figure 5.6 is the change in baseline linearity between spectra A and B. A similar effect is seen in the spectra shown on Figure 5.5. The difference in baseline is due to the degradation of naturally present antioxidants in the oil. Work performed in our lab[9] has demonstrated that these naturally present antioxidants fluoresce weakly when exposed to 785 nm light. As the oil is maintained at 130 °C the antioxidant concentration will decrease as they react with free radicals formed in the oil. The first spectrum obtained in a particular data set will have a relatively high fluorescence signal incorporated into its baseline, while spectra obtained later in the experiment will have a lower concentration of antioxidants and thus lower fluorescence. The difference in the fluorescence intensity due to the

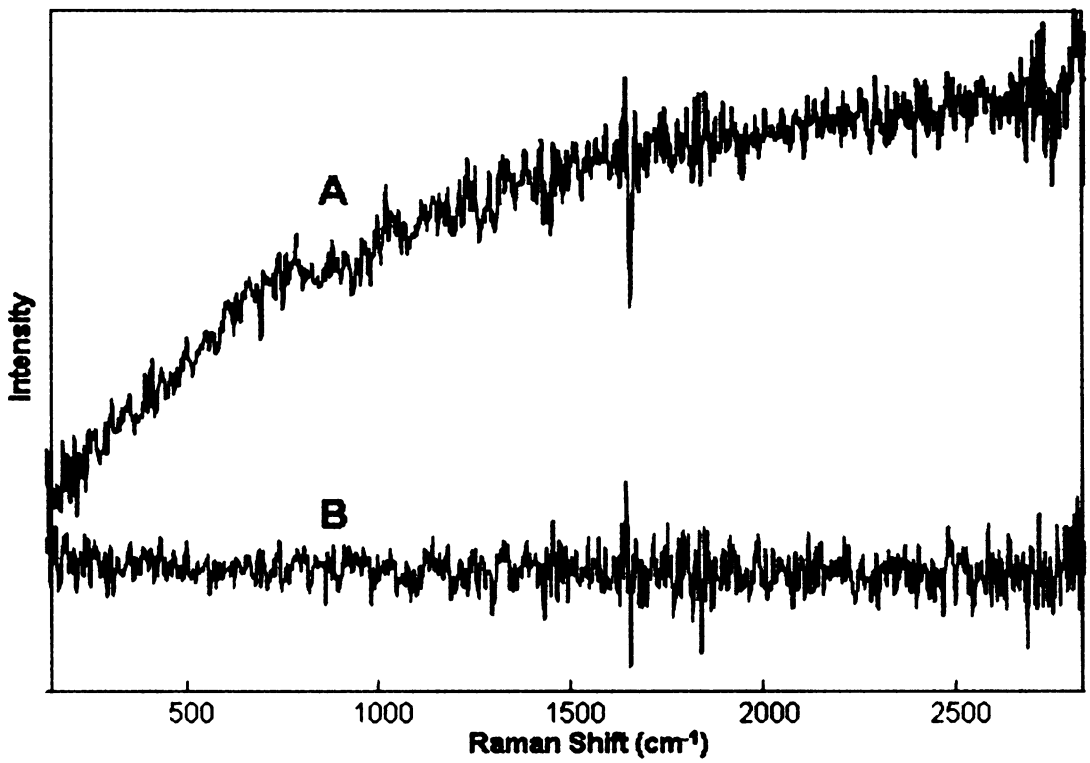

Figure 5.5. Difference Raman spectra obtained for the experiment conducted at 130 °C with 0.5 g of TBHQ added to the oil. Difference spectra calculated by subtracting the first spectrum acquired once the oil reached 130 °C from A) the spectrum acquired after 180 minutes at 130 °C B) the spectrum acquired after 5 minutes at 130 °C.

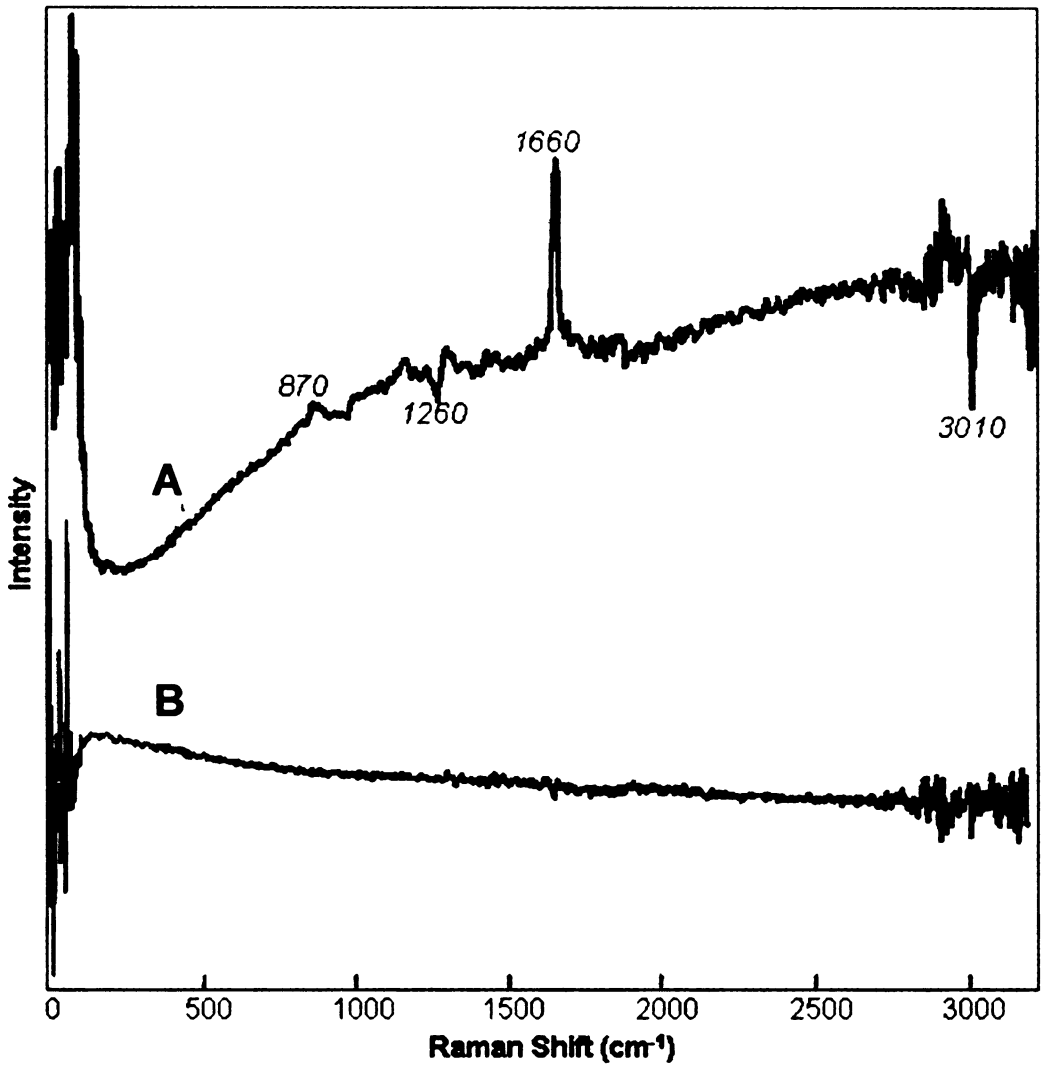

Figure 5.6. Difference Raman spectra obtained for the experiment conducted at 130 °C with no TBHQ added to the oil. Difference spectra calculated by subtracting the first spectrum acquired once the oil reached 130 °C from A) the spectrum acquired after 180 minutes at 130 °C B) the spectrum acquired after 5 minutes at 130 °C.

decrease in antioxidant concentration leads to the changes in baseline observed in Figures 5.5 and 5.6. This theory is further supported by the fact that spectra A in Figure 5.5 displays a smaller change in baseline (when compared to its corresponding spectra B) than spectra A in Figure 5.6. Since spectra A in Figure 5.5 contained a large amount of synthetic antioxidants, it is expected that only a small fraction of its naturally present antioxidant would have reacted with the free radicals formed in the oil. This would lead to a sample with a stronger fluorescence signal at the end of the experiment and therefore a smaller difference in baseline between itself and the first spectrum acquired.

Figure 5.6 A also displays significant features or peaks which are not seen in Figure 5.6 B or in Figure 5.5. It is therefore possible to conclude that the peaks seen in Figure 5.6 A are due to the formation oxidation products during the experiment. The obvious next step is the identification of the compound(s) responsible for the appearance of the peaks. The first visible peak is located at 870 cm^{-1}, it is possible to assign this peak to the O-O stretching vibration of organic peroxides. Organic peroxides are known to strongly Raman scatter in the 870 cm^{-1} region[14]. In addition, we have observed that an addition of 5 wt% of tert-Butylhydroperoxide to sunflower oil produces a peak in the Raman spectrum at approximately 875 cm^{-1}. The 875 cm^{-1} peak area is positive since the concentration of peroxide compounds is higher at the end of the experiment. The next visible peak at 1260 cm^{-1} can be assigned to the in-plane =C-H deformation in an unconjugated *cis* double bond[10], in fact previous work in our lab has correlated changes in the area of this peak to the concentration of *cis* double bonds[9]. As expected the 1260 cm^{-1} peak area is negative, at the temperature examined this is most likely due to the *cis* to *trans* isomerization occurring during oxidation. The third and most pronounced peak

in Figure 5.6 A is located at 1660 cm^{-1}. Closer examination of the spectrum reveals that the 1660 cm^{-1} peak has a small shoulder near 1640 cm^{-1}. In order to better resolve the two peaks, the first derivative of Figure 5.6 A was calculated (shown on Figure 5.7). Figure 5.7 clearly demonstrates that the 1660 cm^{-1} peak in Figure 5.6 A is two overlapped peaks at 1640 and 1660 cm^{-1}. The 1660 cm^{-1} peak has been previously assigned to *trans* C=C bonds[11,18], while the 1640 cm^{-1} peak has been assigned to conjugated C=C bonds[14,19]. The appearance of both of these peaks during our experiments can be linked to the oxidation of fatty acids (see Figure 5.2) since both of the functional groups responsible for the peaks are known to form as oxidation products.

The final peak seen in Figure 5.6 A is located in the 2990-3020 cm^{-1} region. This peak has been assigned to olefinic C-H stretching[19], more specifically, Sadeghi-Jorabchi et al.[11] have demonstrated that the exact position of this peak can be correlated with to the composition of C=C *cis* and *trans* isomers. In our particular case the peak appears at 3010 cm^{-1}, the previous work assigned that peak position to *cis,cis* dienes. Figure 5.6 A indicates that the concentration of *cis,cis* dienes decreases during our experiments. This result is in accord with the fatty acid oxidation theory described previously which predicts the transformation of *cis* C=C bonds to conjugated and unconjugated *trans* C=C bonds.

Figure 5.8 shows the results of spectral subtraction for the experiment conducted at 200 °C without TBHQ. Spectrum A was obtained after 5 minutes and spectrum B was obtained after 180 minutes of holding at 200 °C (spectra have been offset for clarity). The data for the experiment conducted at 200 °C with TBHQ added will not be presented

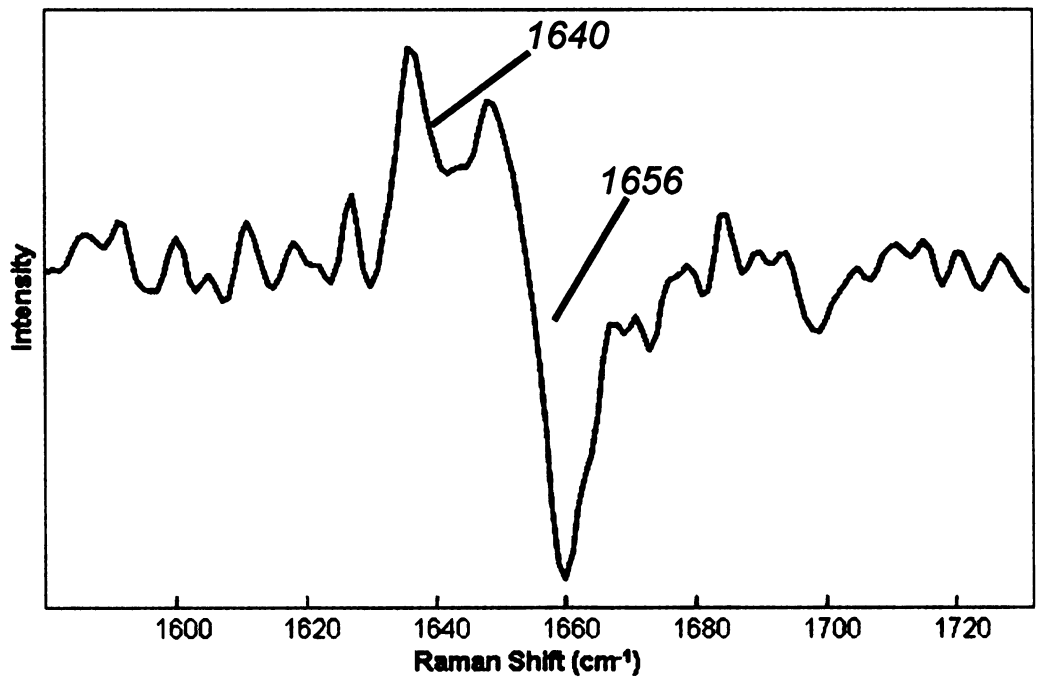

Figure 5.7. First derivative spectrum calculated for difference spectrum A shown in Figure 5.6. First derivative reveals a "hidden" peak at 1640 cm^{-1} which is not visible in the raw spectral data due to overlap with a peak at 1656 cm^{-1}.

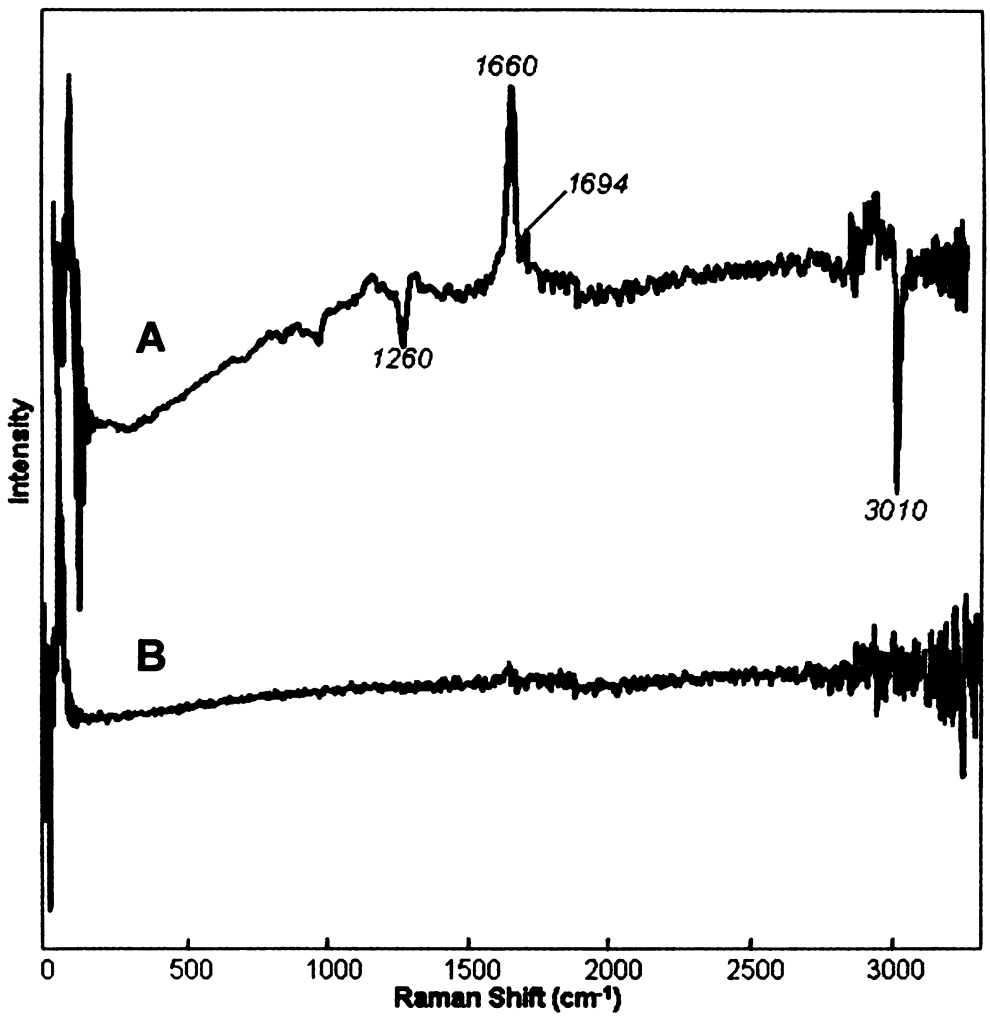

Figure 5.8. Difference Raman spectra obtained for the experiment conducted at 200 °C with no TBHQ added to the oil. Difference spectra calculated by subtracting the first spectrum acquired once the oil reached 200 °C from A) the spectrum acquired after 180 minutes at 200 °C B) the spectrum acquired after 5 minutes at 200 °C.

because it did not show significant differences when compared to the data displayed on Figure 5.8. Essentially, the addition of TBHQ did not affect the oxidation reactions for the experiment conducted at 200 °C. Since the melting range of TBHQ is 126-128 °C it is likely that upon its addition to the 200 °C oil, TBHQ immediately evaporated or thermally decomposed and thus was incapable of performing its role as an antioxidant.

Most of the peaks visible in Figure 5.8 were also visible in Figure 5.6, their assignments remain the same. However, there are some significant differences between the two Figures that are worth discussing. One of the biggest differences between Figures 5.6 and 5.8 is the intensity of the change in baseline linearity. Figure 5.6 A demonstrates a much larger change than Figure 5.8 A. The explanation for this difference is that by the time the oil had reached 200 °C most of the antioxidants had already decomposed or degraded. This would mean that the change in concentration of antioxidants between the first spectrum obtained at 200 °C versus the last spectrum obtained after 180 minutes at 200 °C would be low when compared to the same change for the experiment performed at 130 °C. Another difference between Figures 5.6 A and 5.8 A is that Figure 5.8 A does not show a peak in the 870 cm^{-1} region. There are two likely explanations for this; the first is that the melting range of many organic hydroperoxides is known to be in the 140-160 °C range. It could then be expected that at 200 °C the hydroperoxides that were formed would evaporate almost immediately. The second likely explanation would be an increased in the reaction rate of the hydroperoxides at the higher temperatures. Both of these explanations rely on the fact that the concentration of hydroperoxides in the oil would be kept at very low levels by being heated to 200 °C, making their detection with Raman spectroscopy difficult.

The last major difference between Figures 5.6 A and 5.8 A is the appearance of a peak in Figure 5.8 A in the 1690 cm^{-1} region which is not visible in Figure 5.6 A. Previous work[5,6] using ATR-FTIR observed the appearance of a band in the 1690-1715 cm^{-1} region under very similar experimental conditions. The authors assigned this band to the keto functional group present in free fatty acids and also to the appearance of conjugated keto groups, both of which are formed as products of oil oxidation.

5-4 Conclusions

It is obvious that, as the title of this chapter states, this is a continuing investigation. Much work remains to be done before any definitive conclusions can be made about the data presented here. As a starting point, it would be beneficial to perform the experiments described above at least in triplicate in order to gain a better understanding of the reproducibility (or lack there of) of the oxidation process. In addition, different oxidation conditions (temperature, air-flow rate, humidity) should be examined along with a variety of synthetic and natural antioxidants with the aim of defining the concentration range for which Raman spectroscopy can be used to detect the various oxidation products. Finally, the theories developed using Raman spectroscopy alone must be investigated further by analyzing the oil with chemical methods (e.g. peroxide value (PV), anisidine value (AV), etc.) and other analytical techniques such as GC, FT-IR and perhaps HPLC. Despite the above mentioned shortcomings, the overall objective of the present work, which was to lay the foundation for the development of Raman methods for assessing oil quality in relation to lipid oxidation and thermal stress, was accomplished successfully. We are aware that because of the large number of

compounds created during oil oxidation (many with very similar molecular structures) it is unlikely that Raman spectroscopy (and for that matter vibrational spectroscpies altogether) will ever be able to fully characterize and identify every individual oxidation product. However, if we can continue to monitor spectral changes that occur as oxidation proceeds and assign wavelengths to the more common molecular species produced, it may be possible to create a generalized, rapid approach to monitoring and quantifying key products associated with oxidation. This may in turn lead to the development of a dependable, quantitative, *in situ*, general-purpose Raman spectroscopy based quality control method for the food industry. The results of this study demonstrate the promising future of using dispersive Raman spectroscopy with an NIR excitation source for the analysis of edible oil oxidation on or off-line.

5-5 Acknowledgments

Dr. Dale LeCaptain of Central Michigan University provided the Raman spectrometer. His contribution is appreciated. Partial support of J. A. F. was received from GAANN and Alfred P. Sloan Foundation fellowships.

5-6 References

1. *Food Lipids, Chemistry, Nutrition, and Biotechnology*, Akoh, C.C.; Min, D.B., Eds.; Marcel Dekker: New York, NY, 1997.

2. Perkins, M. J.; *Radical Chemisty,* Ellis Horwood: London, England, 1994.

3. O'Brien, R. D.; *Fats and Oils, Formulating and Processing for Applications,* TECHNOMIC publications: Lancaster, PA, 1998.

4. *Official Methods and Recommended Practices of the AOCS,* 5th ed.; Firestone, D., Ed.; American Oil Chemist's Society: Champaign, Illinois, 1998.

5. Hamilton, R. J.; Cast, J., Eds.; *Spectral Properties of Lipids,* Sheffield Academic Press: Sheffield, England, 1999.

6. van de Voort, F.R.; Ismail, A.A.; Sedman, J.; Emo, G. *J. Am. Oil Chem. Soc.* **1994**, 71 (3), 243-253.

7. Moya Moreno, M.C.M.; Mendoza Olivares, D.; Amezquita Lopez, F.J.; Peris Martinez, V.; Bosch Reig, F. *Journal of Molecular Structure.* **1999**, 482-483, 557-561.

8. Guillen, M.D.; Cabo, N. *Journal of the Science of Food and Agriculture.* **2000**, 80, 2028-2036.

9. Falcon, J.A.; Berglund, K.A. Submitted for publication: *Organic Process Research & Development,* April 2004.

10. Sadeghi-Jorabchi, H.; Hendra, P.J.; Wilson, R.H.; Belton, P.S. *J. Am. Oil Chem. Soc.* **1990**, 67 (8), 483-486.

11. Sadeghi-Jorabchi, H.; Wilson, R.H.; Belton, P.S.; Edwards-Webb, J.D.; Coxon, D.T. *Spectrochimica Acta.* **1991**, 47A (9/10), 1449-1458.

12. Johnson, G.L.; Machado, R.M.; Freidl, K.G.; Achenbach, M.L.; Clark, P.J.; Reidy, S.K. *Organic Process Research & Development.* **2002**, 6 (5), 637-644.

13. Weng, Y.M.; Weng, R.H.; Tzeng, C.Y.; Chen, W. *Applied Spectroscopy.* **2003**, 57 (4), 413-418.

14. F.R.; Fateley, W.G.; Bentley, F.F.; *Characteristic Raman Frequencies of Organic Compounds,* John Wiley & Sons, Inc.: New York, NY, 1974.

15. Battey, D.E.; Slater, J.B.; Wludyka, R.S.; Owen, H.; Pallister, D.M.; Morris, M.D. *Applied Spectroscopy.* **1993**, 47, 1913.

16. Owen, H.; Battey, D.E.; Pelletier, M.J.; Slater, J.B. *Proc. SPIE.* **1995**, 24 (6), 260.

17. Food and Drug Administration, 21CFR172.185

18. Bailey, G.F; Horvat, R.J. *J. Am. Oil Chem. Soc.* **1972**, 49 (8), 494-498.

19. Baeten, V.; Hourant, P.; Morales, M.T.; Aparacio, R. *J. Agric. Food Chem.* **1998**, 46, 2638-2646.

Chapter 6

CONCLUSIONS & NEXT STEPS

This work consists of two major sections in which novel methods and applications of Raman spectroscopy are described for the *in situ* monitoring of two widely used industrial processes. The first section focused on the *in situ* monitoring of anti-solvent addition crystallizations of active pharmaceutical ingredients (APIs) using Raman spectroscopy and principal components analysis (PCA) in order to gain a better understanding of the crystallization process. The second section aimed at using Raman spectroscopy to monitor *in situ* the *cis-trans* isomerization of fatty acids in edible oils during high temperature processing and to lay the foundation for the development of Raman methods for assessing oil quality in relation to lipid oxidation and thermal stress.

In Chapter 2 Raman spectroscopy was used for *in situ* monitoring of antisolvent addition crystallization of cortisone acetate. Raman spectral features of the solvent, the antisolvent, and the solute were monitored to measure the relative concentration of the components. It was found that Raman spectroscopy also provides useful information about the on-set of crystallization. Furthermore, Raman spectroscopy is probably the only analytical technique available that allows for the *in situ* monitoring of the solid-state form that crystallizes. Therefore, the present work provides a method for the *in situ* monitoring of the entire crystallization process, from solution to possible polymorph transformation after crystallization. This study demonstrated the advantages of using Raman spectroscopy is able to provide accurate information regarding not only the crystallization process such as ATR-FTIR and other methods, but it is also capable of providing information on the solid-state form during crystallization and subsequent unit

operations such as drying. Finally, Raman spectroscopy in tandem with differential scanning calorimetry (DSC) was used to monitor the dehydration of crystals during an extended storage time including the effect of an impurity on the transformation rate. These results provide further evidence that Raman spectroscopy can be very useful in rapid screening of different solid-state forms during processing or storage.

The work presented in Chapter 2 demonstrates the usefulness (and advantages compared with other analytical techniques such as DSC or X-ray powder diffraction) of using Raman spectroscopy to monitor solid-state forms after crystallization in a general sense. More in-depth understanding of the specific changes observed for cortisone acetate during storage will require supplementation of the results presented with additional experimental data. A logical first experiment would be the use of thermogravimetric analysis (TGA) or Karl-Fischer titrations in order to accurately determine the amount of water present in the crystal lattice beginning at day zero through the end of the storage period. These experiments would provide valuable information regarding the evaporation rate of water from the crystals which should aid in the development of a conclusive dehydration mechanism. Replacing water with deuterated water as the antisolvent should provide a more solid foundation for peak assignment of the peaks observed to appear during the storage time period (see Figure 2.9).

Further investigations into the project presented in Chapter 2 should also include monitoring the crystallization of compounds other than cortisone acetate. These studies would prove that the *in situ* monitoring technique introduced does not depend on a particular chemical species. Regardless of the solvent, antisolvent and solute used, Raman spectroscopy will be able to provide qualitative and quantitative information

about the components in solution (assuming there is no significant overlap of peaks from the three components) before crystallization occurs and will also provide qualitative information about the crystals once they have formed. Another benefit of investigating different crystallizing species would be the opportunity to study compounds with vastly different metastable regions. In particular it would be interesting to monitor the crystallization of compounds which can sustain very high supersaturation and thus should reach the nucleation stage at a much slower pace than cortisone acetate. High supersaturation conditions have been proven to be conducive to the formation of pre-crystallization solution structures[1]. *In situ* monitoring of these pre-crystallization solution structures could provide some insight into the crystal structure that ultimately forms. It should be noted that the relationship between solution structures formed under high supersaturation conditions and the final crystal structures formed has been investigated in the past[1] and these studies did not find a strong correlation between the structures. However, those studies only focused only on dihydrogen orthophosphate compounds, and it can be argued that different classes of compounds should behave quite differently. Being able to correlate any pre-crystallization solution structure with the final crystal structure would be an important breakthrough particularly for compounds that crystallize in various polymorphic forms.

Another interesting avenue to follow would be the modification of the current approach in order to monitor *in situ* other often used crystallization methods. Temperature change crystallization would be an obvious candidate due to its wide application in the pharmaceutical industry. Assuming the use of a cooling profile to bring about crystallization, the overall Raman scattering intensity would increase as the temperature

is decreased (see Eq. (1-5) in Chapter 1). Obviously this would cause a different peak area profile than those displayed in Figures 2.4-2.6. Despite the differences, the large drop in Raman scattering signal that comes about due to the formation of crystals should still be evident. Furthermore, a cooling crystallization would not require the addition of a third component (assuming the simplest case where there is only one solvent and one solute) which should simplify the analysis of the spectral data.

Using the method developed in Chapter 2 for *in situ* monitoring of anti-solvent crystallization of cortisone acetate, the Raman spectral features of the solute and the anti-solvent were subjected to principal components analysis (PCA) in Chapter 3. The purpose of this analysis was to obtain information from the PCA model which was not readily apparent from the raw spectral data. For the system utilized, PCA was able to distinguish spectral features from the solute in solution, the solute crystals and the anti-solvent. Furthermore, PCA was capable of detecting subtle changes in the spectral data (as the addition of anti-solvent progressed) that could be used as a warning for the onset of crystallization. To our knowledge this is the first reported study that combines PCA with Raman spectroscopy for monitoring crystallizations *in situ*.

In Chapter 3, PCA was used solely as a qualitative tool; only the pattern of the scores was used to monitor the progress and onset of crystallization. With the method used, the model was recalculated with the incorporation of every new spectrum acquired. Because the model was constantly recalculated the scores and loadings were also continually changing. The constant change is important because the interpretation of the principal components changes with time as the data set changes (see Figure 3.11). The first principal component always represents the largest variation in the data set; however this

variation will change over time. For example, at the beginning of the experiment (before crystallization) the larges variation in the data set is due to the dilution of the solution by the addition of water, therefore PC1 will likely be due to those changes. Following crystallization the largest variation will be due to the drastic drop in signal intensity, and PC1 will then reflect that variation. Under these circumstances, PCA is not being used to create a model. Instead, it is essentially another way to deconvolute spectra.

A solution to this problem would be to use a training set to create a PCA model which could then be used to "predict" real time scores as the newly acquired spectra were introduced into the model. With this approach, the "predicted" scores values could be used quantitatively to monitor the crystallization process by creating a feedback control loop. The control loop would use the scores values as indicators to vary the water addition rate. As with most models that are created the benefits that may be gained by the construction of the predictive model might be undone by the inflexible nature of the model. Unexpected changes such as an increase or decrease in water addition rate or a variation in the temperature would likely cause the model to fail.

Chapters 4 and 5 concentrate on *in situ* monitoring of edible oil degradation and oxidation under simulated processing conditions. In Chapter 4, a novel dispersive Raman spectroscopic procedure for the *in situ* monitoring of fatty acid *cis* to *trans* isomerization in edible oils is described. Raman spectral changes observed during the high temperature heating of oil were correlated with *cis* and *trans* isomer concentration determined by gas chromatography (GC). The short acquisition times, low laser power and ease of application of dispersive Raman spectroscopy using an NIR excitation source combined with the correlation derived from the GC data provided the capability of monitoring the

isomerization *in situ*. The method developed has potential applications for increased process control of edible oil hydrogenation, deodorization and quality control among other widely used processing steps.

Chapter 5 describes preliminary studies which aim at utilizing Raman spectroscopy to *in situ* monitor the oxidation of thermally stressed edible oil. Spectral subtraction was used to enhance spectral changes observed under the accelerated oxidation conditions. The difference spectra displayed peaks which could be assigned to various functional groups, such as hydroperoxides, conjugated C=C, *trans* C=C and ketones, which are known to form as products of oil oxidation. It was also possible to qualitatively monitor the disappearance or degradation of natural antioxidants during oxidation. Although further work must be done in order to complete this study, the results obtained thus far indicate that it will be possible to develop a dependable, quantitative, *in situ*, general-purpose Raman spectroscopy based method to monitor and quantify key products associated with oil oxidation.

The degradation of edible oils subjected to high temperature in open air conditions is known to be a complicated process[2,3] dominated by the oxidation of fatty acids. The formation of many of the decomposition products is largely dependent on the exact stress conditions applied to the oil[2]. For these reasons, future work on the projects presented in Chapters 4 and 5 must include high performance liquid chromatography (HPLC) analysis. Because the decomposition of the oils is so complex and involves the production of such a wide variety of compounds[2,4] (from polymers to volatile compounds) it should be expected that Raman spectroscopy alone will not be able to differentiate many of the compounds created. HPLC analysis would provide more

definitive information regarding the degradation products formed. In addition, it may then be possible to correlate the HPLC and Raman spectral data. This correlation could lead to the ability of using Raman spectroscopy to quickly analyze stressed oils for particular decomposition products.

Once an HPLC method was in place, it would be possible to monitor oil oxidation *in situ* under "normal" cooking conditions. Researchers[5,6] have defined cooking conditions of interest in order to analyze the used oil for chemical composition changes. To our knowledge there are no reports of monitoring cooking oil *in situ*. One obvious obstacle to this experiment will be the added chemical compounds that food can introduce to the oil during the cooking process. It would be expected that fresh food, for example fresh potatoes, would introduce a large amount of water into the oil. The water will quickly turn to steam in the hot oil, and it is reasonable to argue that the steam generated would increase the rate of oxidation of the oil. Raman spectroscopy would be well suited to monitoring *in situ* the rapidly changing chemical environment during frying.

6-1 References

1. Cerreta, M.K.; Ph.D. Dissertation, Michigan State University, East Lansing, Michigan, 1988.

2. *Food Lipids, Chemistry, Nutrition, and Biotechnology*, Akoh, C.C., Min, D.B., Ed.; Marcel Dekker: New York, NY, 1997.

3. O'Brien, R. D.; *Fats and Oils, Formulating and Processing for Applications,* TECHNOMIC publications: Lancaster, PA, 1998.

4. Hamilton, R. J.; Cast, J., Eds.; *Spectral Properties of Lipids,* Sheffield Academic Press: Sheffield, England, 1999.

5. Houhoula, D.P.; Oreopoulou, V.; Tzia, C. *J. Am. Oil Chem. Soc.* **2002**, 79 (2), 49133-137.

6. Sebedio, J-L.; Bonpunt, A.; Grandgirard, A.; Prevost, J. *J. Agric. Food Chem.* **1990**, 38, 1862-1867.

APPENDIX

Table A1. Data for Figure 2.3

Water Weight %	Acetone Weight %	Cortisone Acetate Weight %	Standard Deviation
60.08	39.74	0.18	0.04
51.11	48.40	0.49	0.05
42.22	56.93	0.85	0.03
29.72	68.31	1.97	0.07
16.43	80.53	3.04	0.06
8.04	88.49	3.47	0.10

Table A2. Data for Figure 2.4 (water addition rate: 0.25 mL/min).

Time (min.)	Peak Area 750-850 cm^{-1}
0.0	1.67E+07
1.0	1.65E+07
1.9	1.62E+07
3.0	1.58E+07
3.9	1.55E+07
5.0	1.51E+07
5.9	1.48E+07
6.9	1.45E+07
8.0	1.43E+07
9.0	1.40E+07
9.9	1.38E+07
10.9	1.35E+07
12.0	1.32E+07
12.9	1.30E+07
14.0	1.28E+07
15.0	1.25E+07
15.9	1.23E+07
17.0	1.22E+07
18.0	1.20E+07
18.9	1.18E+07
20.0	1.16E+07
21.0	1.14E+07
21.9	1.12E+07
23.0	1.10E+07
24.0	1.08E+07
25.0	1.07E+07
26.0	1.05E+07
27.0	1.04E+07
28.0	1.02E+07
29.0	1.01E+07
30.0	9.95E+06
30.9	9.81E+06
32.0	9.69E+06
33.0	9.56E+06
33.9	9.43E+06
35.0	9.32E+06
36.0	9.20E+06
36.9	9.10E+06
38.0	9.02E+06
39.0	8.92E+06
39.9	8.81E+06
41.0	8.71E+06
42.0	8.59E+06
42.9	8.50E+06
44.0	8.40E+06
45.0	8.33E+06
45.9	8.24E+06
47.0	8.15E+06
48.0	8.06E+06
48.9	7.77E+06
50.0	6.92E+06
51.0	5.89E+06
51.9	5.24E+06
53.0	5.19E+06
54.0	4.96E+06
54.9	4.80E+06
56.0	4.55E+06
57.0	4.43E+06
57.9	4.39E+06
59.0	4.34E+06
60.0	4.29E+06
60.9	4.11E+06
62.0	4.03E+06
63.0	4.02E+06
63.9	4.05E+06
65.0	4.13E+06
66.0	4.05E+06
66.9	4.00E+06
68.0	3.95E+06
69.0	3.83E+06
69.9	3.78E+06
71.0	3.76E+06
72.0	3.78E+06
72.9	3.75E+06
74.0	3.69E+06
75.0	3.70E+06
75.9	3.62E+06
77.0	3.59E+06
78.0	3.61E+06
78.9	3.61E+06
80.0	3.58E+06
81.0	3.54E+06
81.9	3.47E+06
83.0	3.48E+06
84.0	3.44E+06
84.9	3.40E+06
86.0	3.43E+06
87.0	3.39E+06
87.9	3.39E+06
89.0	3.34E+06
90.0	3.30E+06
90.9	3.28E+06
92.0	3.31E+06
93.0	3.31E+06
93.9	3.21E+06
95.0	3.12E+06
96.0	3.12E+06
96.9	3.11E+06
98.0	3.02E+06
99.0	3.06E+06

Table A3. Data for Figure 2.4 (water addition rate: 0.50 mL/min).

Time (min.)	Peak Area 750-850 cm^{-1}
1.0	1.07E+07
2.0	1.01E+07
3.0	9.90E+06
4.0	9.76E+06
5.0	9.67E+06
6.0	9.31E+06
7.0	9.01E+06
8.0	8.74E+06
9.0	8.44E+06
10.0	8.24E+06
11.0	7.98E+06
12.0	7.71E+06
13.0	7.46E+06
14.0	7.28E+06
15.0	7.12E+06
16.0	6.94E+06
17.0	6.79E+06
18.0	6.65E+06
19.0	6.50E+06
20.0	6.37E+06
21.0	6.32E+06
22.0	6.15E+06
23.0	6.04E+06
24.0	5.93E+06
25.0	5.81E+06

Time (cont.)	Peak Area
26.0	5.69E+06
27.0	5.58E+06
28.0	4.48E+06
29.0	3.25E+06
30.0	2.99E+06
31.0	2.93E+06
32.0	2.87E+06
33.0	2.79E+06
34.0	2.75E+06
35.0	2.74E+06
36.0	2.72E+06
37.0	2.70E+06
38.0	2.69E+06
39.0	2.68E+06
40.0	2.64E+06
41.0	2.67E+06
42.0	2.63E+06
43.0	2.63E+06
44.0	2.60E+06
45.0	2.62E+06
46.0	2.61E+06
47.0	2.59E+06
48.0	2.58E+06
49.0	2.59E+06
50.0	2.56E+06
51.0	2.54E+06

Table A4. Data for Figure 2.4 (water addition rate: 1.00 mL/min).

Time (min.)	Peak Area 750-850 cm^{-1}
0.0	1.18E+07
1.0	1.06E+07
2.0	9.22E+06
3.0	8.95E+06
4.0	8.64E+06
5.0	8.39E+06
6.0	7.97E+06
7.0	7.57E+06
8.0	7.24E+06
9.0	6.92E+06
10.0	6.60E+06
11.0	6.50E+06
12.0	6.23E+06
13.0	6.01E+06
14.0	5.16E+06
15.0	3.45E+06
16.0	2.98E+06
17.0	2.83E+06
18.0	2.78E+06
19.0	2.71E+06
20.0	2.68E+06
21.0	2.72E+06
22.0	2.73E+06
23.0	2.69E+06
24.0	2.71E+06
25.0	2.67E+06
26.0	2.66E+06

Table A5. Data for Figure 2.5 (water addition rate: 0.25 mL/min).

Time (min.)	Peak Area 750-850 cm^{-1}
0.0	1.70E+07
1.0	1.69E+07
2.0	1.66E+07
3.0	1.61E+07
4.0	1.58E+07
5.0	1.57E+07
6.0	1.53E+07
7.0	1.50E+07
8.0	1.46E+07
9.0	1.44E+07
10.0	1.42E+07
11.0	1.41E+07
12.0	1.39E+07
13.0	1.34E+07
14.0	1.30E+07
15.0	1.29E+07
16.0	1.27E+07
17.0	1.24E+07
18.0	8.09E+06

Time (cont.)	Peak Area
19.0	4.49E+06
20.0	3.98E+06
21.0	3.77E+06
22.0	3.72E+06
23.0	3.59E+06
24.0	3.51E+06
25.0	3.37E+06
26.0	3.33E+06
27.0	3.24E+06
28.0	3.13E+06
29.0	3.12E+06
30.0	3.05E+06
31.0	3.01E+06
32.0	2.95E+06
33.0	2.90E+06
34.0	2.88E+06
35.0	2.87E+06
36.0	2.88E+06
37.0	2.81E+06
38.0	2.79E+06
39.0	2.78E+06
40.0	2.75E+06

Time (cont.)	Peak Area
41.0	2.72E+06
42.0	2.70E+06
43.0	2.70E+06
44.0	2.69E+06
45.0	2.65E+06
46.0	2.65E+06
47.0	2.62E+06
48.0	2.65E+06
49.0	2.63E+06
50.0	2.57E+06
51.0	2.60E+06
52.0	2.55E+06
53.0	2.53E+06
54.0	2.58E+06
55.0	2.59E+06
56.0	2.56E+06
57.0	2.54E+06
58.0	2.54E+06
59.0	2.53E+06
60.0	2.53E+06
61.0	2.52E+06

Table A6. Data for Figure 2.5 (water addition rate: 0.50 mL/min).

Time (min.)	Peak Area 750-850 cm^{-1}
0.0	1.63E+07
1.1	1.63E+07
2.0	1.60E+07
3.0	1.55E+07
4.0	1.50E+07
5.0	1.45E+07
6.0	1.40E+07
7.0	1.35E+07
8.0	1.31E+07
9.0	1.27E+07
10.0	1.21E+07
11.0	7.09E+06
12.0	3.77E+06
13.0	3.17E+06
14.0	2.96E+06
15.0	2.78E+06
16.0	2.66E+06
17.0	2.54E+06
18.0	2.48E+06
19.0	2.42E+06
20.0	2.40E+06
21.0	2.35E+06
22.0	2.34E+06
23.0	2.32E+06
24.0	2.34E+06
25.0	2.29E+06
26.0	2.27E+06
27.0	2.25E+06
28.0	2.24E+06
29.0	2.24E+06
30.0	2.21E+06
31.0	2.22E+06
32.0	2.21E+06

Table A7. Data for Figure 2.5 (water addition rate: 1.00 mL/min).

Time (min.)	Peak Area 750-850 cm^{-1}
0.0	1.44E+07
1.0	1.31E+07
2.0	1.20E+07
3.0	1.16E+07
4.0	1.11E+07
5.0	1.04E+07
6.0	2.31E+06
7.0	1.71E+06
8.0	1.59E+06
9.0	1.51E+06
10.0	1.49E+06
11.0	1.49E+06
12.0	1.48E+06
13.0	1.46E+06
14.0	1.46E+06
15.0	1.47E+06
16.0	1.48E+06

Table A8. Data for Figure 2.6 (water addition rate: 0.25 mL/min).

Time (min.)	Peak Area 750-850 cm^{-1}
1.0	1.02E+05
2.0	9.68E+04
3.0	9.65E+04
4.0	9.10E+04
5.0	9.11E+04
6.0	8.86E+04
7.0	8.21E+04
8.0	8.41E+04
9.0	8.11E+04
10.0	7.91E+04
11.0	7.70E+04
12.0	7.32E+04
13.0	7.21E+04
14.0	7.01E+04
15.0	6.86E+04
16.0	6.94E+04
17.0	6.58E+04
18.0	4.33E+04
19.0	2.59E+04
20.0	2.45E+04
21.0	2.38E+04
22.0	2.38E+04
23.0	2.31E+04
24.0	2.17E+04
25.0	2.58E+04
26.0	2.37E+04
27.0	2.10E+04
28.0	2.14E+04
29.0	2.21E+04

Time (cont.)	Peak Area
30.0	2.24E+04
31.0	2.01E+04
32.0	2.27E+04
33.0	1.98E+04
34.0	2.33E+04
35.0	2.21E+04
36.0	2.25E+04
37.0	2.24E+04
38.0	1.97E+04
39.0	2.22E+04
40.0	2.29E+04
41.0	2.12E+04
42.0	2.05E+04
43.0	2.26E+04
44.0	2.31E+04
45.0	2.14E+04
46.0	2.11E+04
47.0	2.11E+04
48.0	2.05E+04
49.0	2.24E+04
50.0	1.97E+04
51.0	2.54E+04
52.0	2.10E+04
53.0	2.31E+04
54.0	2.19E+04
55.0	2.11E+04
56.0	2.14E+04
57.0	2.00E+04
58.0	1.95E+04
59.0	2.18E+04
60.0	2.33E+04
61.0	2.25E+04

Table A9. Data for Figure 2.6 (water addition rate: 0.50 mL/min).

Time (min.)	Peak Area 750-850 cm^{-1}
1.1	8.95E+04
2.0	8.41E+04
3.0	7.84E+04
4.0	7.19E+04
5.0	6.87E+04
6.0	6.76E+04
7.0	6.10E+04
8.0	6.01E+04
9.0	3.72E+04
10.0	1.96E+04
11.0	1.91E+04
12.0	1.54E+04
13.0	1.43E+04
14.0	1.69E+04
15.0	1.87E+04
16.0	1.32E+04
17.0	1.58E+04
18.0	1.45E+04
19.0	1.60E+04
20.0	1.56E+04
21.0	1.68E+04
22.0	1.74E+04
23.0	1.82E+04
24.0	1.80E+04
25.0	1.78E+04
26.0	1.66E+04
27.0	1.74E+04
28.0	2.04E+04
29.0	1.95E+04
30.0	1.76E+04

Table A10. Data for Figure 2.6 (water addition rate:1.00 mL/min).

Time (min.)	Peak Area 750-850 cm^{-1}
1.0	7.24E+04
2.0	6.69E+04
3.0	5.87E+04
4.0	5.98E+04
5.0	5.03E+04
6.0	1.28E+04
7.0	1.01E+04
8.0	9.26E+03
9.0	1.11E+04
10.0	1.06E+04
11.0	1.25E+04
12.0	1.32E+04
13.0	1.33E+04
14.0	1.36E+04
15.0	1.37E+04
16.0	1.11E+04

Table A11. Data for Figure 2.12

Days After Crystallization	(A) Peak Width 1585-1635 cm^{-1}	(B) Peak Width 1585-1635 cm^{-1}	(C) Peak Width 1585-1635 cm^{-1}
0	8.67	8.88	8.67
1	8.87	8.88	8.72
2	8.88	8.88	8.73
3	11.00	11.00	15.03
4	14.00	15.75	16.91
5	---	17.06	16.86
6	16.49	---	16.86
7	17.15	16.85	16.86
8	---	17.03	16.86
9	17.09	16.89	16.86
10	16.89	17.18	---
11	17.04	16.91	---
12	17.06	16.98	---
13	---	17.03	---
14	16.92	16.88	---
15	16.98	---	---
16	16.83	---	---

Table A12. Data for Figure 2.13

Days After Crystallization	Peak Width 1585-1635 cm^{-1} (0.04 wt% Bisnoraldehyde)	Peak Width 1585-1635 cm^{-1} (0.15 wt% Bisnoraldehyde)	Peak Width 1585-1635 cm^{-1} (0.22 wt% Bisnoraldehyde)
0	8.61	8.72	9.05
1	8.64	8.75	8.87
2	8.66	8.75	8.97
3	8.70	8.85	9.15
4	8.78	8.76	9.17
5	9.44	8.85	9.14
6	13.49	8.93	9.27
7	16.44	10.35	9.00
8	16.95	15.09	9.06
9	17.07	16.92	9.10
10	17.03	16.86	9.30
11	---	16.86	10.40
12	---	16.86	---
13	---	16.86	---
14	---	16.86	---

Table A13. Data for Figure 3.3

Water Weight %	Acetone Weight %	Cortisone Acetate Weight %	Standard Deviation
49.72	49.40	0.88	0.03
40.16	57.13	2.71	0.09
24.65	68.26	7.09	0.17
16.20	72.90	10.9	0.04
8.43	76.47	15.1	0.14

Table A14. Data for Figure 3.9

Volume of Water Added (mL)	PC1 Scores
0.00	-2.33E+04
0.32	-2.28E+04
0.60	-2.10E+04
0.88	-1.93E+04
1.15	-1.75E+04
1.43	-1.61E+04
1.71	-1.45E+04
1.98	-1.28E+04
2.27	-1.14E+04
2.54	-9.80E+03
2.82	-8.52E+03
3.10	-6.75E+03
3.38	-5.70E+03
3.65	-4.25E+03
3.93	-3.64E+03
4.21	-2.25E+03
4.49	-1.38E+03
4.77	5.13E+02
5.05	9.89E+02
5.33	1.18E+03
5.61	1.65E+03
5.88	2.40E+03
6.17	3.06E+03
6.44	3.81E+03
6.73	4.73E+03
7.01	5.85E+03
7.28	6.02E+03
7.57	6.67E+03
7.84	7.09E+03
8.13	7.74E+03
8.40	7.86E+03
8.68	8.00E+03
8.96	8.54E+03
9.24	8.90E+03

Water Added (cont.)	PC1 Scores
9.53	9.03E+03
9.80	9.06E+03
10.08	9.30E+03
10.37	9.52E+03
10.64	9.56E+03
10.93	1.00E+04
11.21	9.84E+03
11.48	1.00E+04
11.77	9.83E+03
12.05	1.00E+04
12.33	9.88E+03
12.61	9.89E+03

Table A15. Data for Figure 4.4

Time (min.)	1745 cm^{-1} Average Peak Area	Standard Deviation
0	6.96E+04	1.32E+03
2.5	7.01E+04	8.58E+02
5	7.17E+04	1.80E+03
7.5	7.09E+04	1.19E+03
10	7.03E+04	1.94E+03
12.5	6.99E+04	1.42E+03
15	7.09E+04	1.10E+03
17.5	7.13E+04	1.21E+03
20	7.12E+04	6.62E+02
22.5	7.12E+04	6.63E+02
25	7.15E+04	1.69E+02
27.5	6.95E+04	1.09E+03
30	6.92E+04	2.88E+03
32.5	7.11E+04	1.58E+03
35	7.00E+04	9.79E+02
37.5	7.18E+04	9.53E+02
40	7.01E+04	8.54E+02

Table A16. Data for Figure 4.5 and 4.6

Heating Temperature (°C)	Cis Isomer Concentration (wt%)	1265/1745 Average Peak Area Ratio	Standard Deviation
No heating	88.59	1.71	0.06
200	88.24	1.66	0.06
250	87.67	1.59	0.09
300	80.12	1.35	0.03

Heating Temperature (°C)	Trans Isomer Concentration (wt%)	1745/1265 Average Peak Area Ratio	Standard Deviation
No heating	0.94	0.59	0.02
200	1.68	0.60	0.02
250	1.22	0.63	0.03
300	8.48	0.74	0.02

Table A17. Data for Figure 4.7

Time (min.)	1745/1265 Average Peak Area Ratio at 200 °C	Standard Deviation	1745/1265 Average Peak Area Ratio at 250 °C	Standard Deviation	1745/1265 Average Peak Area Ratio at 300 °C	Standard Deviation
0	0.69	0.01	0.75	0.02	0.77	0.01
2.5	0.69	0.00	0.74	0.01	0.77	0.00
5	0.70	0.02	0.74	0.03	0.80	0.02
7.5	0.70	0.00	0.75	0.00	0.81	0.01
10	0.71	0.02	0.74	0.03	0.81	0.03
12.5	0.70	0.02	0.75	0.02	0.82	0.04
15	0.70	0.01	0.75	0.04	0.83	0.03
17.5	0.71	0.02	0.74	0.01	0.84	0.04
20	0.69	0.01	0.75	0.03	0.85	0.04
22.5	0.70	0.01	0.76	0.05	0.86	0.03
25	0.70	0.01	0.77	0.06	0.88	0.03
27.5	0.70	0.01	0.78	0.03	0.87	0.05
30	0.70	0.02	0.77	0.05	0.87	0.06
32.5	0.70	0.01	0.78	0.05	0.92	0.06
35	0.69	0.00	0.78	0.04	0.92	0.04
37.5	0.69	0.01	0.79	0.04	0.94	0.03
40	0.71	0.02	0.79	0.03	0.93	0.05